



Universiteit
Leiden
The Netherlands

The relation between dynamics and activity of phospholipase A/acyltransferase homologs

Chatterjee, S.D.

Citation


Chatterjee, S. D. (2022, March 2). *The relation between dynamics and activity of phospholipase A/acyltransferase homologs*. Retrieved from <https://hdl.handle.net/1887/3277998>

Version: Publisher's Version

License: [Licence agreement concerning inclusion of doctoral thesis in the Institutional Repository of the University of Leiden](#)

Downloaded from: <https://hdl.handle.net/1887/3277998>

Note: To cite this publication please use the final published version (if applicable).



The relation between dynamics and activity of
phospholipase A/acyltransferase homologs

Soumya Deep Chatterjee

The relation between dynamics and activity of phospholipase A/acyltransferase homologs

Soumya Deep Chatterjee

The relation between dynamics and activity of phospholipase A/acyltransferase homologs.

Proefschrift

ter verkrijging van
de graad van doctor aan de Universiteit Leiden,
op gezag van rector magnificus prof.dr.ir. H. Bijl,
volgens het besluit van het college voor promoties
te verdedigen op 2 maart 2022
klokke 13:45 uur

door

Soumya Deep Chatterjee
Geboren te Siliguri, India

in 1990

Promotores:

Prof. dr. Marcellus Ubbink

Prof. dr. Mario van der Stelt

Promotiecommissie:

Prof. dr. H.S. Overkleeft

Prof. dr. A. Kros

Prof. dr. J.M.F.G. Aerts

Dr. J. Vreede (University of Amsterdam)

Dr. M. Tessari (Radboud University Nijmegen)

Table of Contents

Chapter 1 Introduction	6-27
Chapter 2 Sub-second ^{15}N backbone dynamics reveal differences between PLAAT3 and PLAAT4	29-64
Chapter 3 Molecular dynamics simulations reveal loop rearrangements in PLAAT4	66-83
Chapter 4 Introduction of the PLAAT4 L2(B6) in PLAAT3 disrupts salt bridges and increases activity	85-102
Chapter 5 Removal of slow-pulsing artifacts in in-phase ^{15}N relaxation dispersion experiments using broadband ^1H decoupling	104-124
Chapter 6 General Discussion	126-131
Summary	132-137
Curriculum Vitae	138
List of Publications	138

Abbreviations

CPD	Composite pulse decomposition
CPMG	Carr-Purcell-Meiboom-Gill
CW	Continuous wave
LRAT	Lecithin: retinol acyltransferases
MD	Molecular dynamics
NAE	<i>N</i> -acylethanolamine
NAPE	<i>N</i> -acyl phosphatidyl ethanolamine
NMR	Nuclear magnetic resonance
PC	Phosphatidylcholine
PE	Phosphatidylethanolamine
PLAAT	Phospholipase A/acyltransferase
ppm	Parts per million
RMSD	Root mean square deviation
ST	Single train
TROSY	Transverse relaxation optimized spectroscopy

1

Chapter

Introduction

The PLAAT family

Phospholipase A/acyltransferases (PLAATs) are a five-membered family of enzymes. They were first identified as H-Ras-like class II tumor suppressors (HRASLS).¹ Numerous research studies in different scientific domains led to them being named in a variety of ways. These names are summarized in Table 1.1. The five members are a part of a larger, diverse superfamily NlpC/P60 thiol proteases or papain-like proteases because of their sequence similarities with lecithin: retinol acyltransferases (LRAT), a member of the NlpC/P60 family.² PLAATs share a highly conserved sequence NCEHFV, which contains cysteine that acts as the nucleophile and is part of the catalytic triad.²⁻⁵ This triad consists next to the cysteine of two histidines, one acting as the base that deprotonates the sulfhydryl group of the nucleophile and the other stabilizes the imidazole ring of the basic histidine in PLAAT2-5. In PLAAT1, the latter histidine is replaced by asparagine. This cysteine-histidine-histidine catalytic triad is a hallmark signature of NlpC/P60 superfamily of proteins.⁶ Four of the PLAAT enzymes are membrane anchored proteins having a C-terminal trans-membrane domain, while PLAAT5, the largest of all PLAATs, lacks this anchor.⁷

Table 1.1. Alternative names for PLAAT proteins found in literature

PLAAT1	PLAAT2	PLAAT3	PLAAT4	PLAAT5
A-C1	PLA/AT-2	HREV107	TIG3	HRASLS-5
HRASLS-1	PLA _{1/2} -2	HREV107-1	RIG1	RLP-1
PLA/AT-1	HRASLS-2	H-REV107	PLA/AT-4	HRSL5
HRSL1		PLA/AT-3	HRASLS-4	HRLP5
		PLA2G16	RARRES3	iNAT
		MCG118754	PLA _{1/2} -3	PLA/AT-5
		RLP-3		
		adPLA		
		HRASLS-3		

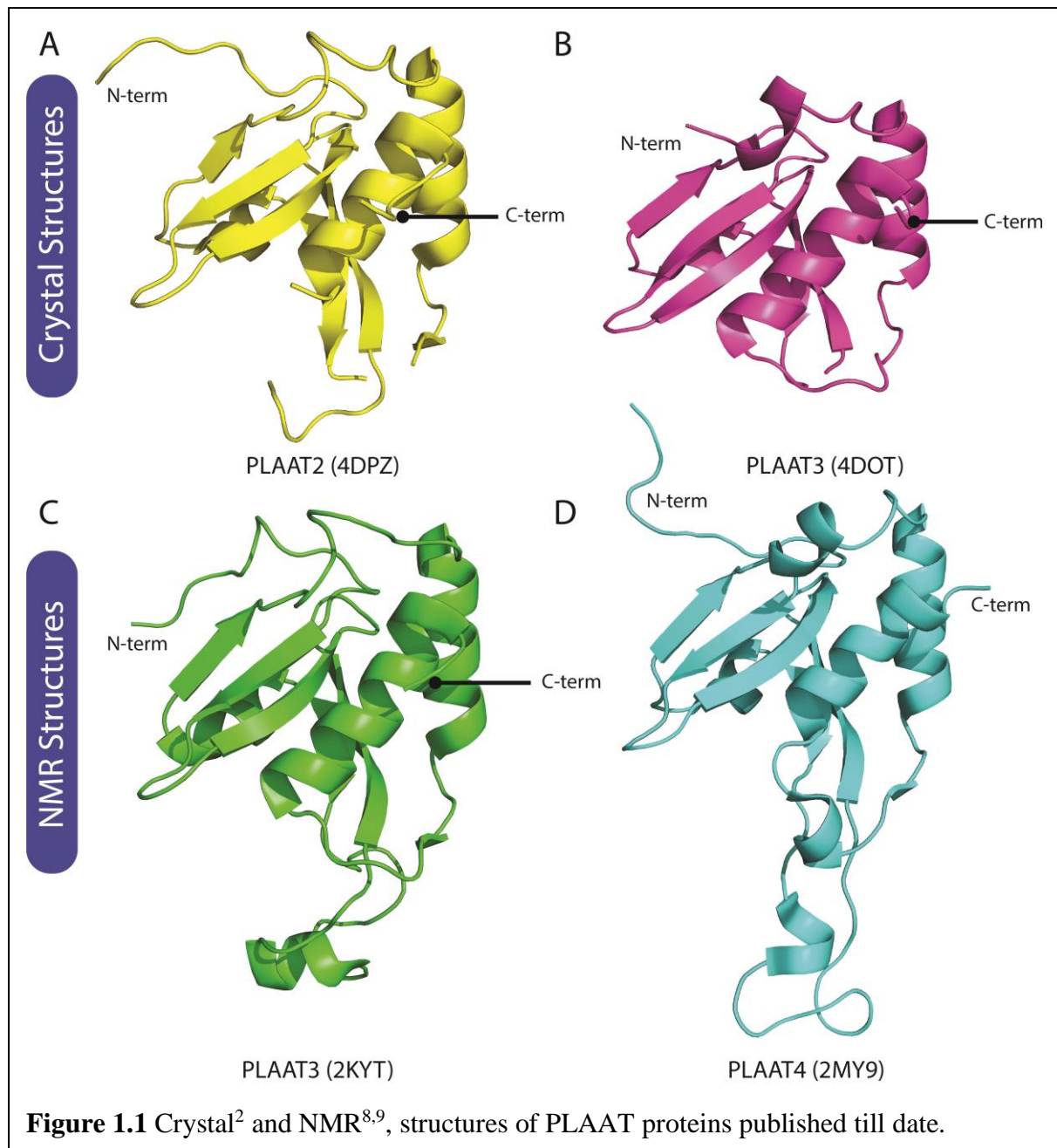
Only the three-dimensional structures of three PLAATs (PLAAT2, PLAAT3 and PLAAT4) are known. The PLAATs share similar secondary structure motifs and have an active site similar to those found in NlpC/P60 superfamily.^{2,8,9} The crystal structures of PLAAT2 (PDB

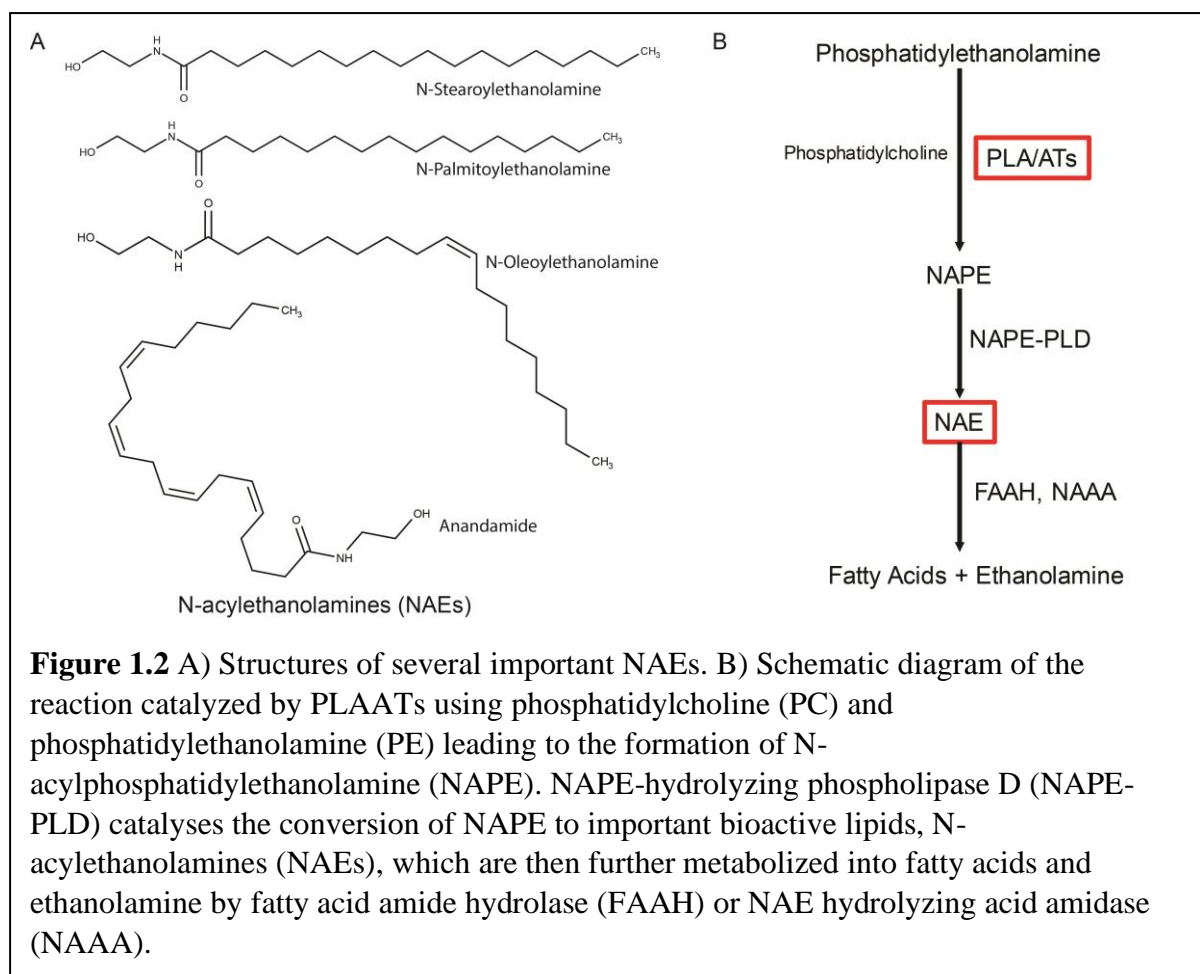
entry 4DPZ) and PLAAT3 (4DOT) were first determined by Golczak *et al.*² and the NMR structures of PLAAT3 (2KYT) and PLAAT4 (2MY9) were later solved by Xia *et al.* (Figure 1.1).^{8,9} The secondary structure comprises three α -helices (crystal structures and NMR structure of PLAAT3) or four α -helices (NMR structure of PLAAT4) and antiparallel β -sheet containing four strands (crystal structures) or six strands (NMR structures), similar to classic segregated α + β -folds of papain-like proteases.^{2,6}

Functions of PLAATs

The PLAATs catalyze the first step of reactions leading to the formation of N-acylphosphatidylethanolamines (NAPE), which undergoes further steps to form N-acylethanolamines (NAEs), an important class of bioactive lipids that play roles in a variety of processes, such as anti-inflammation (N-palmitoylethanolamine),¹⁰⁻¹² catabolism of fat (N-oleoylethanolamine),¹³ anti-apoptotic activity (N-stearoylethanolamine),¹³ and ligands for endocannabinoid receptors (anandamide), see Figure 1.2.¹⁴⁻¹⁶

PLAATs, as the name suggests, demonstrate phospholipase A_{1/2} (PLA_{1/2}) activities, in which both phosphatidylcholine (PC) and phosphatidylethanolamine (PE) act as substrates.^{3,7,17-20} All PLAATs except PLAAT3 show specificity for the PLA₁ position, whereas for PLAAT3 contradicting evidence from various studies suggest that the protein may prefer either the A1 or the A2 position, depending on the type of substrate and assay conditions.²¹⁻²³ The second part of the name comes from their ability to transfer the acyl-chain of a phosphoglyceride (for example PC) to the amino group of a phosphatidylethanolamine (PE), leading to the formation of NAPEs, as mentioned above. Furthermore, apart from being an N-acyltransferase, PLAATs can also act as O-acyltransferases, transferring an acyl-chain to the sn-1 or sn-2 position of a lysophospholipid, for example lysophosphatidylcholine.^{2,3,17,19,24} See Figure 1.3 for all the reactions catalyzed by PLAATs.





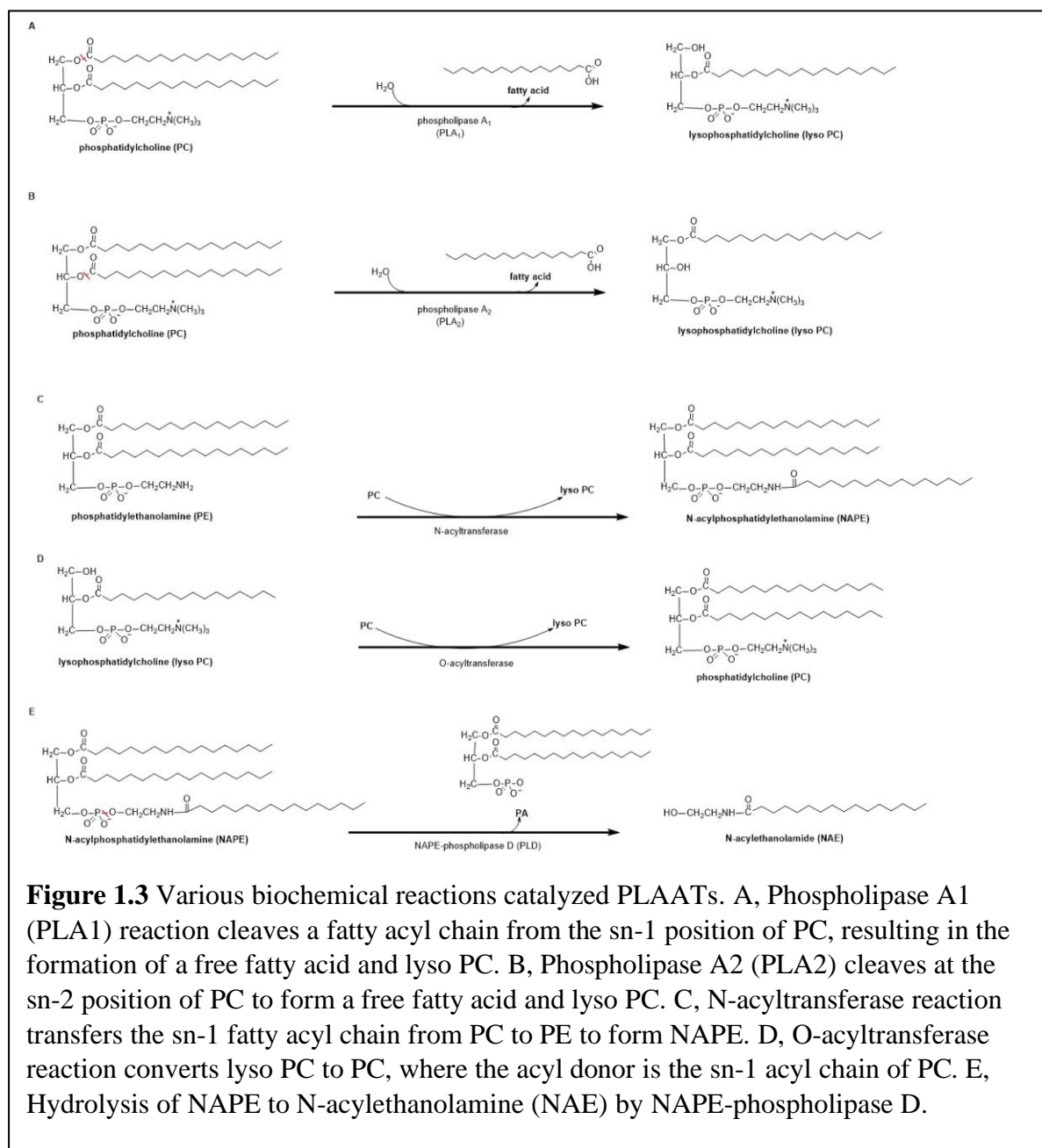
In human beings, mice and rats, the gene for PLAAT1 is expressed mostly in skeletal muscle, heart and testes, where its physiological role has not been investigated so far.¹⁷ PLAAT1 shows an N-acyltransferase activity that is higher than the PLA_{1/2} activity.^{3,17,24,25} PLAAT2 is only found in human beings and especially in the trachea, stomach, colon and kidneys.⁷ It has been known to suppress tumors (class II) in breast cells and cervical cancer cells.⁷ This protein also exhibits strong N-acyltransferase activity and less PLA_{1/2} activity and, interestingly, prefers the sn-1 position of PC for the former activity.^{19,24} PLAAT3 was also discovered as a tumor suppressor^{20,26–32}, however contradicting reports showed that PLAAT3 rather increases tumor progression.^{29,33} In contrast to PLAAT1 and PLAAT2, PLAAT3 shows a preference for PLA activity over N-acyltransferase activity.^{17,24} However, PLAAT1 and PLAAT3 both share common function in organelle degradation in lens.³⁴ PLAAT3 also plays an important role in viral entry pathways by acting as host factor for enterovirus^{35–37}. PLAAT3 is found mostly in white adipose tissue and less in brown adipose tissue^{21,38}. In white adipose tissue, it modulates lipolysis and therefore is a critical factor in obesity, as was elegantly demonstrated in mice models by Jaworski *et al.*³⁸ PLAAT3 inhibitors^{39,40}, therefore would be potential therapeutic

anti-obesity and anti-viral targets. Like PLAAT3, PLAAT4 was also discovered and shown to work as tumor suppressor.⁴¹⁻⁴⁶ PLAAT4, like PLAAT2 is a human-specific ortholog. It is found in skin cells, where it interacts with and activates transglutaminase I (TG1), which in turn produces cornified envelope, necessary for keratinocyte proliferation and survival, and skin to function as a physical and water barrier.⁴⁷⁻⁵⁰ As PLAAT4 is a class II tumor suppressor, it was shown to be down-regulated in psoriasis and skin cancer in a study by Duvic *et al.*⁵¹

PLAAT4 is a homolog of PLAAT3^{41,42} and it also shows more PLA_{1/2} activity than N-acyltransferase activity.^{17,19,24} However, the two enzymes exhibit a contrasting characteristic regarding the PLA_{1/2} activity. The transmembrane C-terminal domain is crucial for PLAAT3 membrane-attachment as well as PLA_{1/2} activity and truncation of this domain has been shown by Uyama *et al.* to result in loss of phospholipase activity.⁵² In contrast, Golczak *et al.*² demonstrated with truncated N-terminal domains of PLAATs that, unlike truncated PLAAT3, truncated PLAAT4 is capable of phospholipase activity, suggesting that the transmembrane C-terminal domain is not critical for PLAAT4 PLA_{1/2} activity. Furthermore, these authors demonstrated by studying the rate of breakdown of short-chain phospholipids and studying the protein-acyl intermediates that the truncated PLAAT4 is more active as phospholipase than PLAAT3. Although PLAAT3 and PLAAT4 are homologs, they clearly differ in activity and specificity toward substrates. Physiologically, the phospholipase activity of PLAAT3 plays an important role in adipose tissue as it regulates triglyceride metabolism.²¹ Phospholipase activity of PLAAT4, on the other hand, plays a crucial role in tumor suppression, particularly in metastasis and invasion.⁴⁶ Moreover Wei *et al.* demonstrated that the NTD of PLAAT4 was found to be enhancing the cell death effect of the CTD, whereas the NTD of PLAAT3 was found to be inhibitory.⁸ Therefore, the differences in activity between the two enzymes can be studied by studying the roles played by the N-terminal and C-terminal domains on a molecular level. The findings could hold the key to the understanding of the molecular mechanisms and physiological significance of these enzymes that are yet to be studied in detail. Studying the roles of N-terminal and C-terminal domains of the two enzymes at a molecular level can help to obtain an understanding of the molecular mechanisms and physiological significance of these enzymes which may advance the design and discovery of selective PLAAT inhibitors.

The aim of the research presented in this thesis, therefore, was to elucidate the reason for the difference in activities (especially phospholipase activity) between PLAAT3 and PLAAT4, present despite their similar sequences and structures. It was hypothesized that differences in the dynamic properties could be the cause of the differences in activity, so NMR spectroscopy

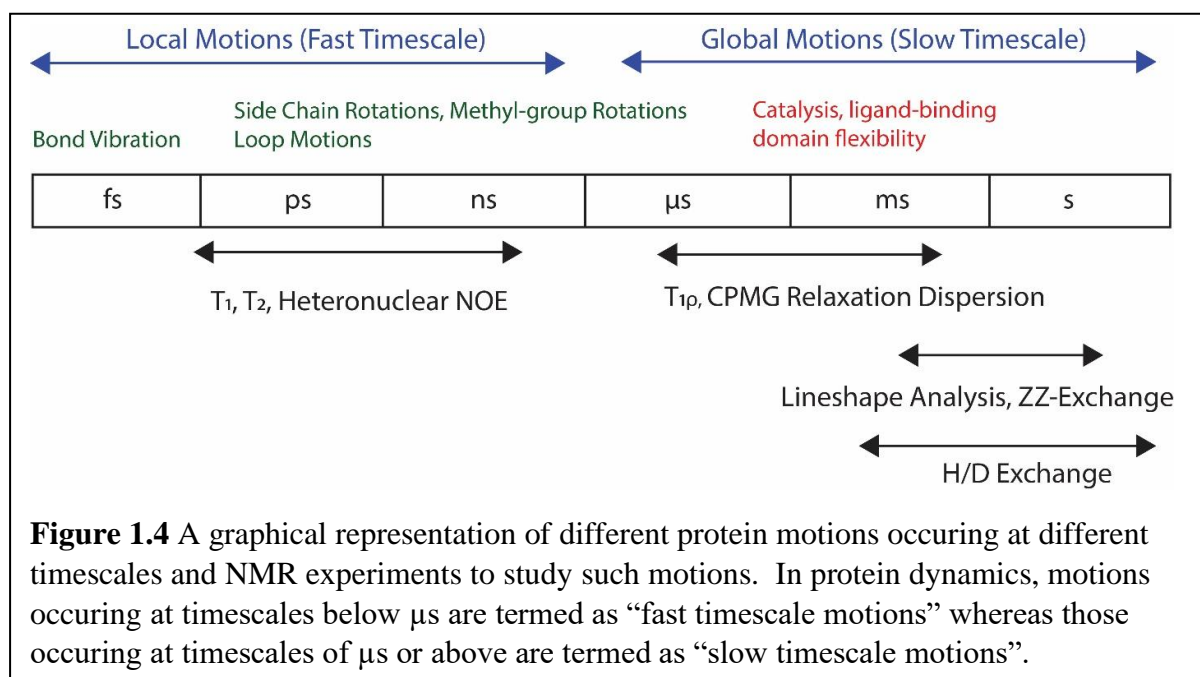
and MD simulations were used to characterize the enzymes. Both methods are briefly introduced below.



NMR Spectroscopy

Studying protein dynamics with NMR spectroscopy has created a new perspective on what proteins are and how they function. This applies to enzymes in particular. Proteins are no longer seen as static entities but as dynamic ensembles occupying various positions in a free energy landscape.^{53–55} Protein dynamics occur at many timescales and different sets of NMR

experiments allow us to probe biologically relevant phenomena occurring at those timescales (Figure 1.4).⁵⁶ Protein motions occurring at ps-ns timescale can be studied using longitudinal relaxation (R_1), transverse relaxation (R_2) and heteronuclear nuclear Overhauser effect/enhancement (NOE).⁵⁷⁻⁶¹ Several dynamics parameter, such as the order parameter (S^2), global rotational correlation time (τ_c), effective rotational correlation time (τ_e) and the exchange rate (R_{ex}) can be quantified using the model free analysis developed by Lipari and Szabo.^{62,63} The order parameter ranges from 0 (highly dynamic) to 1 (rigid), τ_c is an indicator of molecular tumbling time and is highly dependent on the size of the protein. τ_e is in the range of ps-ns ($\tau_e < \tau_c$) and is a measure of local motions, such as loop flexibility. R_{ex} indicates exchange contribution to the linewidth (apparent transverse relaxation rate), due either to motions in the μ s-ms timescale that cause chemical shift changes or to chemical exchange phenomena. Generally, data are acquired at two magnetic fields to improve the statistical fitting of the data to one of five “model-free” models, because relaxation rates are field dependent. These five models fit the measured relaxation rates with an increasing number of parameters to obtain S^2 , τ_e and R_{ex} for individual nuclei in the protein, usually of backbone ^{15}N atoms. The term model-free refers to the fact that these parameters are defined without a predefined notion of the type of motion in mind, such as rotation in a cone.^{64,65} The ps-ns motions are often associated with flexibility of loops and termini, and in many cases such motions may not be related to biological function but rather are a property of protein matter. However, a growing number of studies have shown that protein dynamics at this timescale can also affect function.⁶⁶⁻⁷⁴



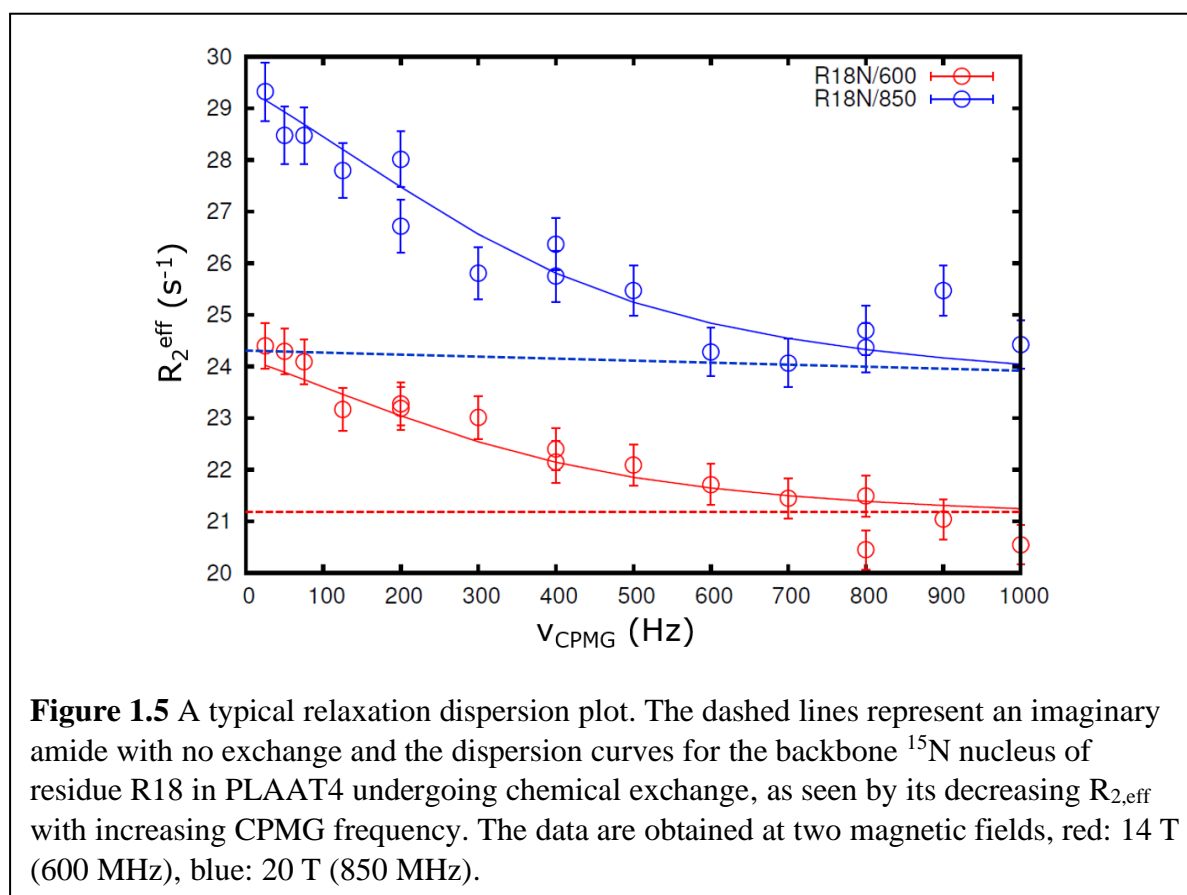
Biologically relevant and important phenomena occur at μs - ms timescale such as catalysis,^{75–78} protein folding,^{79–83} protein-protein or protein-ligand interactions.^{84–89} NMR experiments such as $R_{1\rho}$ and CPMG relaxation dispersion (RD) and chemical exchange saturation transfer (CEST) are crucial in providing information about dynamics occurring at this timescale.^{90–95} The general principle of all these experiments is that different states have different NMR properties (chemical shifts, dipolar couplings or relaxation rates) and that the exchange between states affects the NMR signals, by causing changes in peak intensity or linewidth. Thus, these experiment can extract information about the population, exchange rates and structures of minor conformers that are in exchange with the major ground state conformation.^{96–102} Since the minor conformation is sparsely populated, the already low intensity peaks are usually further broadened out due to exchange, which makes them ‘invisible’. Therefore, information about the minor conformers is obtained from the effects of exchange on the NMR resonance of the major conformer, or on the signal average in case of fast exchange between the two states. In the CPMG-RD experiment, the chemical exchange is quantified by obtaining the exchange contribution to the apparent transverse relaxation rate (R_2) of the nucleus in the major conformer. This is achieved by using a train of 180° pulses at a frequency of $\nu_c = 1/4\tau_{cp}$ (where ν_c is the CPMG frequency and $2\tau_{cp}$ is time between the 180° pulses in the train) during a period T to reduce the exchange contribution to the linewidth. By performing a series of experiments with varying ν_c , the effective apparent line width ($R_{2,eff}$) can be determined from the peak intensities in each of these experiment (I_{CPMG}) relative to a reference spectrum for which T is set to zero (I_0), equation 1.1.

$$R_{2,eff} = \frac{1}{T} \ln \left(\frac{I_{CPMG}}{I_0} \right) \quad (\text{Equation 1.1})$$

Nuclei that do not undergo chemical exchange, do not have the exchange contribution and hence, the $R_{2,eff}$ is same at all CPMG frequencies and equals the intrinsic R_2 . A plot of $R_{2,eff}$ vs. CPMG frequency shows a dispersion profile (Figure 1.5). A nucleus undergoing exchange will have a profile showing a decreasing $R_{2,eff}$ with increasing CPMG frequency until it reaches a plateau, being the intrinsic R_2 . The parameters describing the exchange process, such as the rate of exchange (k_{ex}), population of the minor conformer (p_B) and the absolute chemical shift difference between the major and the minor conformer ($|\Delta\omega|$) can be obtained from the dispersion curves by minimizing the following equation:

$$X^2(\zeta) = (R'_{2,eff}(\varphi) - R_{2,eff}) / \Delta R_{2,eff} \quad (\text{Equation 1.2})$$

Where $R'_{2,\text{eff}}$ is the calculated rate of relaxation obtained by solving the Bloch-McConnell equations,^{103,104} $R_{2,\text{eff}}$ is the effective transverse relaxation rate, φ is a function of dynamics parameters such as k_{ex} , p_{B} and $\Delta\omega$. The detailed analysis of the CPMG RD experiments to deduce the structure of the minor conformer as well as the experiments required for calculating the sign of the $\Delta\omega$ are outside the scope of this thesis and can be found in many excellent review papers, such as.^{105–110}



NMR spectroscopy, though a powerful tool to study protein dynamics, is not bereft of limitations.

It is inherently insensitive due to the small energy gaps involved in magnetic resonance transitions, so concentrated samples are required. Furthermore, depending on the rate of the chemical process, NMR will often yield an average observable, making it difficult to determine the properties of the individual components that cause the averaged observable.¹¹¹ Exchange dynamics is rich in information but can also hinder observation of nuclei considerably, for example if the resonances broaden beyond detection or due to exchange with solvent hydrogens of which the signals are necessarily suppressed in protein NMR experiments. All these factors can make it impossible to interpret dynamic properties in terms of structural changes.

Molecular Dynamics Simulation

Molecular dynamics (MD) simulation is another powerful tool for studying protein dynamics and can serve to complement the information obtained from NMR spectroscopy. MD simulations allow us to quantify and visualize atomic motions occurring in a protein at fast timescale as well as, due to the growth in modern computational capabilities, slower timescale. An introduction to MD simulations is presented in Chapter 3. For the possibilities of combining NMR spectroscopy on proteins and MD simulations, the reader is referred to two excellent reviews, by Case¹¹² and Fiset *et al.*¹¹³

Thesis Outline

At the start of the research in October 2014, NMR assignments of PLAAT3¹¹⁴ and PLAAT4,¹¹⁵ the crystal structures of PLAAT2 and PLAAT3² and the NMR structure of PLAAT3⁹ were available. The structure of PLAAT4 was reported in January 2015.⁸ Here, the first protein dynamics data of ¹⁵N-labelled PLAAT3 and PLAAT4 obtained with NMR spectroscopy are presented in Chapter 2. To complement our understanding of the dynamics of the two proteins and to get more information on the residues that could not be studied with NMR spectroscopy due to solvent exchange and slow-timescale-exchange-related line broadening, MD simulations were performed on the two proteins, described in chapter 3. The combination of NMR data and MD results enabled us to formulate a hypothesis to explain the differences in phospholipase activity of two proteins. The hypothesis was then tested by performing mutations both *in silico* and *in vitro*. MD simulations as well as activity assays on the variants were performed, leading to the remarkable conclusion that loop exchange from PLAAT4 to PLAAT3 can introduce enzymatic activity in the latter protein, a gain-of-function mutation. These results are described in Chapter 4. In Chapter 5, a study on CPMG RD NMR experiments is described, in which an artifact observed during the slow pulsing regimes is analyzed and the efficacy of different decoupling sequences in its removal was tested. Chapter 6 contains a general discussion on PLAAT3 and PLAAT4 dynamics and activity and the scope for future research on the phospholipase A/acyltransferase family.

References

- (1) Ito, H., Akiyama, H., Shigeno, C., and Nakamura, T. (2001) Isolation, characterization, and chromosome mapping of a human A-C1 Ha-Ras suppressor gene (HRASLS). *Cytogenet. Genome Res.* 93, 36–39.
- (2) Golczak, M., Kiser, P. D., Sears, A. E., Lodowski, D. T., Blaner, W. S., and Palczewski, K. (2012) Structural basis for the acyltransferase activity of lecithin:retinol acyltransferase-like proteins. *J. Biol. Chem.* 287, 23790–23807.
- (3) Jin, X.-H., Uyama, T., Wang, J., Okamoto, Y., Tonai, T., and Ueda, N. (2009) cDNA cloning and characterization of human and mouse Ca²⁺-independent phosphatidylethanolamine N-acyltransferases. *Biochim. Biophys. Acta - Mol. Cell Biol. Lipids* 1791, 32–38.
- (4) Ruiz, A., Winston, A., Lim, Y.-H., Gilbert, B. A., Rando, R. R., and Bok, D. (1999) Molecular and biochemical characterization of lecithin retinol acyltransferase. *J. Biol. Chem.* 274, 3834–3841.
- (5) Kiser, P. D., Golczak, M., Maeda, A., and Palczewski, K. (2012) Key enzymes of the retinoid (visual) cycle in vertebrate retina. *Biochim. Biophys. Acta* 1821, 137–151.
- (6) Anantharaman, V., and Aravind, L. (2003) Evolutionary history, structural features and biochemical diversity of the NlpC/P60 superfamily of enzymes. *Genome Biol.* 4, R11–R11.
- (7) Shyu, R.-Y., Hsieh, Y.-C., Tsai, F.-M., Wu, C.-C., and Jiang, S.-Y. (2008) Cloning and functional characterization of the HRASLS2 gene. *Amino Acids* 35, 129–137.
- (8) Wei, H., Wang, L., Ren, X., Yu, W., Lin, J., Jin, C., and Xia, B. (2015) Structural and functional characterization of tumor suppressors TIG3 and H-REV107. *FEBS Lett.* 589, 1179–1186.
- (9) Ren, X., Lin, J., Jin, C., and Xia, B. (2010) Solution structure of the N-terminal catalytic domain of human H-REV107--a novel circularly permuted NlpC/P60 domain. *FEBS Lett.* 584, 4222–4226.

- (10) Calignano, A., Rana, G. La, Giuffrida, A., and Piomelli, D. (1998) Control of pain initiation by endogenous cannabinoids. *Nature* 394, 277–281.
- (11) Lambert, D. M., Vandevoorde, S., and Fowler, K.-O. J. and C. J. (2002) The palmitoylethanolamide family: a new class of anti-inflammatory agents? *Curr. Med. Chem.* 9, 663–674.
- (12) Ara, I., Rahman, S., Tsuboi, K., Uyama, T., and Ueda, N. (2014) New players in the fatty acyl ethanolamide metabolism OH OH OH. *Pharmacol. Res.* 86, 1–10.
- (13) Rodríguez de Fonseca, F., Navarro, M., Gómez, R., Escuredo, L., Nava, F., Fu, J., Murillo-Rodríguez, E., Giuffrida, A., LoVerme, J., Gaetani, S., Kathuria, S., Gall, C., and Piomelli, D. (2001) An anorexic lipid mediator regulated by feeding. *Nature* 414, 209–212.
- (14) Devane, W. A., Hanus, L., Breuer, A., Pertwee, R. G., Stevenson, L. A., Griffin, G., Gibson, D., Mandelbaum, A., Etinger, A., and Mechoulam, R. (1992) Isolation and structure of a brain constituent that binds to the cannabinoid receptor. *Science* (80-.). 258, 1946 LP – 1949.
- (15) Di Marzo, V. (1998) ‘Endocannabinoids’ and other fatty acid derivatives with cannabimimetic properties: biochemistry and possible physiopathological relevance. *Biochim. Biophys. Acta - Lipids Lipid Metab.* 1392, 153–175.
- (16) Di Marzo, V., De Petrocellis, L., Fezza, F., Ligresti, A., and Bisogno, T. (2002) Anandamide receptors. *Prostaglandins, Leukot. Essent. Fat. Acids* 66, 377–391.
- (17) Shinohara, N., Uyama, T., Jin, X., Tsuboi, K., Tonai, T., Houchi, H., and Ueda, N. (2011) Enzymological analysis of the tumor suppressor A-C1 reveals a novel group of phospholipid-metabolizing enzymes. *J. Lipid Res.* 52, 1927–1935.
- (18) Jin, X.-H., Okamoto, Y., Morishita, J., Tsuboi, K., Tonai, T., and Ueda, N. (2007) Discovery and characterization of a Ca²⁺-independent phosphatidylethanolamine N-acyltransferase generating the anandamide precursor and its congeners. *J. Biol. Chem.* 282, 3614–3623.
- (19) Uyama, T., Jin, X.-H., Tsuboi, K., Tonai, T., and Ueda, N. (2009) Characterization of the human tumor suppressors TIG3 and HRASLS2 as phospholipid-metabolizing enzymes. *Biochim. Biophys. Acta - Mol. Cell Biol. Lipids* 1791, 1114–1124.
- (20) Hajnal, A., Klemenz, R., and Schäfer, R. (1994) Subtraction cloning of H-rev107, a gene

specifically expressed in H-ras resistant fibroblasts. *Oncogene* 9, 479–490.

(21) Duncan, R. E., Sarkadi-nagy, E., Jaworski, K., Ahmadian, M., and Sul, H. S. (2008) Identification and functional characterization of adipose-specific phospholipase A2 (AdPLA). *J. Biol. Chem.* 283, 25428–25436.

(22) Uyama, T., Morishita, J., Jin, X.-H., Okamoto, Y., Tsuboi, K., and Ueda, N. (2009) The tumor suppressor gene H-Rev107 functions as a novel Ca²⁺-independent cytosolic phospholipase A1/2 of the thiol hydrolase type. *J. Lipid Res.* 50, 685–693.

(23) Pang, X.-Y., Cao, J., Addington, L., Lovell, S., Battaile, K. P., Zhang, N., Rao, J. L. U. M., Dennis, E. A., and Moise, A. R. (2012) Structure/function relationships of adipose phospholipase A2 containing a Cys-His-His catalytic triad. *J. Biol. Chem.* 287, 35260–35274.

(24) Uyama, T., Ikematsu, N., Shinohara, N., Jin, X., Tsuboi, K., and Tonai, T. (2012) Generation of N -acylphosphatidylethanolamine by members of the phospholipase A / acyltransferase (PLA / AT) family. *J. Biol. Chem.* 287, 31905–31919.

(25) Uyama, T., Inoue, M., Okamoto, Y., Shinohara, N., Tai, T., Tsuboi, K., Inoue, T., Tokumura, A., and Ueda, N. (2013) Involvement of phospholipase A / acyltransferase-1 in N -acylphosphatidylethanolamine generation. *BBA - Mol. Cell Biol. Lipids* 1831, 1690–1701.

(26) Sers, C., Emmenegger, U., Husmann, K., Bucher, K., Andres, A. C., and Schäfer, R. (1997) Growth-inhibitory activity and downregulation of the class II tumor-suppressor gene H-rev107 in tumor cell lines and experimental tumors. *J. Cell Biol.* 136, 935–944.

(27) Roder, K., Latasa, M.-J., and Sul, H. S. (2002) Silencing of the mouse H-rev107 gene encoding a class II tumor suppressor by CpG methylation. *J. Biol. Chem.* 277, 30543–30550.

(28) Yanatatsaneejit, P., Chalermchai, T., Kerekhanjanarong, V., Shotelersuk, K., Supiyaphun, P., Mutirangura, A., and Sriuranpong, V. (2008) Promoter hypermethylation of CCNA1, RARRES1, and HRASLS3 in nasopharyngeal carcinoma. *Oral Oncol.* 44, 400–406.

(29) Nazarenko, I., Kristiansen, G., Fonfara, S., Guenther, R., Gieseler, C., Kemmner, W., Schafer, R., Petersen, I., and Sers, C. (2006) H-REV107-1 stimulates growth in non-small cell lung carcinomas via the activation of mitogenic signaling. *Am. J. Pathol.* 169, 1427–1439.

(30) Nazarenko, I., Schäfer, R., and Sers, C. (2007) Mechanisms of the HRSL3 tumor suppressor function in ovarian carcinoma cells. *J. Cell Sci.* 120, 1393 LP – 1404.

- (31) Shyu, R.-Y., Wu, C.-C., Wang, C.-H., Tsai, T.-C., Wang, L.-K., Chen, M.-L., Jiang, S.-Y., and Tsai, F.-M. (2013) H-rev107 regulates prostaglandin D2 synthase-mediated suppression of cellular invasion in testicular cancer cells. *J. Biomed. Sci.* 20, 30.
- (32) Wang, C.-H., Shyu, R.-Y., Wu, C.-C., Tsai, T.-C., Wang, L.-K., Chen, M.-L., Jiang, S.-Y., and Tsai, F.-M. (2014) Phospholipase A/Acyltransferase enzyme activity of H-rev107 inhibits the H-RAS signaling pathway. *J. Biomed. Sci.* 21, 36.
- (33) Xiong, S., Tu, H., Kollareddy, M., Pant, V., Li, Q., Zhang, Y., Jackson, J. G., Suh, Y.-A., Elizondo-Fraire, A. C., Yang, P., Chau, G., Tashakori, M., Wasylshen, A. R., Ju, Z., Solomon, H., Rotter, V., Liu, B., El-Naggar, A. K., Donehower, L. A., Martinez, L. A., and Lozano, G. (2014) Pla2g16 phospholipase mediates gain-of-function activities of mutant p53. *Proc. Natl. Acad. Sci. U. S. A.* 111, 11145–11150.
- (34) Morishita, H., Eguchi, T., Tsukamoto, S., Sakamaki, Y., Takahashi, S., Saito, C., Koyama-Honda, I., and Mizushima, N. (2021) Organelle degradation in the lens by PLAAT phospholipases. *Nature* 592, 634–638.
- (35) Baggen, J., Liu, Y., Lyoo, H., van Vliet, A. L. W., Wahedi, M., de Bruin, J. W., Roberts, R. W., Overduin, P., Meijer, A., Rossmann, M. G., Thibaut, H. J., and van Kuppeveld, F. J. M. (2019) Bypassing pan-enterovirus host factor PLA2G16. *Nat. Commun.* 10, 3171.
- (36) Elling, U., Wimmer, R. A., Leibbrandt, A., Burkard, T., Michlits, G., Leopoldi, A., Micheler, T., Abdeen, D., Zhuk, S., Aspalter, I. M., Handl, C., Liebergesell, J., Hubmann, M., Husa, A.-M., Kinzer, M., Schuller, N., Wetzl, E., van de Loo, N., Martinez, J. A. Z., Estoppey, D., Riedl, R., Yang, F., Fu, B., Dechat, T., Ivics, Z., Agu, C. A., Bell, O., Blaas, D., Gerhardt, H., Hoepfner, D., Stark, A., and Penninger, J. M. (2017) A reversible haploid mouse embryonic stem cell biobank resource for functional genomics. *Nature* 550, 114–118.
- (37) Staring, J., von Castelmur, E., Blomen, V. A., van den Hengel, L. G., Brockmann, M., Baggen, J., Thibaut, H. J., Nieuwenhuis, J., Janssen, H., van Kuppeveld, F. J. M., Perrakis, A., Carette, J. E., and Brummelkamp, T. R. (2017) PLA2G16 represents a switch between entry and clearance of Picornaviridae. *Nature* 541, 412–416.
- (38) Jaworski, K., Ahmadian, M., Duncan, R. E., Sarkadi-nagy, E., Varady, K. A., Hellerstein, M. K., Lee, H.-Y., Samuel, V. T., Shulman, G. I., Kim, K., de Val, S., Kang, C., Sul, H. S., Val, S. De, Kang, C., and Sul, H. S. (2009) AdPLA ablation increases lipolysis and prevents obesity induced by high-fat feeding or leptin deficiency. *Nat. Med.* 15, 159–168.

- (39) Zhou, J., Mock, E. D., Al Ayed, K., Di, X., Kantae, V., Burggraaff, L., Stevens, A. F., Martella, A., Mohr, F., Jiang, M., van der Wel, T., Wendel, T. J., Ofman, T. P., Tran, Y., de Koster, N., van Westen, G. J. P., Hankemeier, T., and van der Stelt, M. (2020) Structure–activity relationship studies of α -ketoamides as inhibitors of the phospholipase A and acyltransferase enzyme family. *J. Med. Chem.* 63, 9340–9359.
- (40) Jiang, B., Yu, B., Zhang, X., Liu, M., and Yang, D. (2015) A 15N CPMG relaxation dispersion experiment more resistant to resonance offset and pulse imperfection. *J. Magn. Reson.* 257, 1–7.
- (41) DiSepio, D., Ghosn, C., Eckert, R. L., Deucher, A., Robinson, N., Duvic, M., Chandraratna, R. A., and Nagpal, S. (1998) Identification and characterization of a retinoid-induced class II tumor suppressor/growth regulatory gene. *Proc. Natl. Acad. Sci. U. S. A.* 95, 14811–14815.
- (42) Huang, S.-L., Shyu, R.-Y., Yeh, M.-Y., and Jiang, S.-Y. (2000) Cloning and characterization of a novel retinoid-inducible gene 1(RIG1) deriving from human gastric cancer cells. *Mol. Cell. Endocrinol.* 159, 15–24.
- (43) Casanova, B., de la Fuente, M. T., Garcia-Gila, M., Sanz, L., Silva, A., Garcia-Marco, J. A., and Garcia-Pardo, A. (2001) The class II tumor-suppressor gene RARRES3 is expressed in B cell lymphocytic leukemias and down-regulated with disease progression. *Leukemia* 15, 1521–1526.
- (44) Tsai, F.-M., Shyu, R.-Y., and Jiang, S.-Y. (2007) RIG1 suppresses Ras activation and induces cellular apoptosis at the Golgi apparatus. *Cell. Signal.* 19, 989–999.
- (45) Huang, S.-L., Shyu, R.-Y., Yeh, M.-Y., and Jiang, S.-Y. (2002) The retinoid-inducible gene I: effect on apoptosis and mitogen-activated kinase signal pathways. *Anticancer Res.* 22, 799–804.
- (46) Morales, M., Arenas, E. J., Urosevic, J., Guiu, M., Fernández, E., Planet, E., Fenwick, R. B., Fernández-Ruiz, S., Salvatella, X., Reverter, D., Carracedo, A., Massagué, J., and Gomis, R. R. (2014) RARRES3 suppresses breast cancer lung metastasis by regulating adhesion and differentiation. *EMBO Mol. Med.* 6, 865–881.
- (47) Scharadin, T. M., and Eckert, R. L. (2014) TIG3: an important regulator of keratinocyte proliferation and survival. *J. Invest. Dermatol.* 134, 1811–1816.

- (48) Jans, R., Sturniolo, M. T., and Eckert, R. L. (2008) Localization of the TIG3 transglutaminase interaction domain and demonstration that the amino-terminal region is required for TIG3 function as a keratinocyte differentiation regulator. *J. Invest. Dermatol.* 128, 517–529.
- (49) Sturniolo, M. T., Dashti, S. R., Deucher, A., Rorke, E. A., Broome, A.-M., Chandraratna, R. A. S., Keepers, T., and Eckert, R. L. (2003) A novel tumor suppressor protein promotes keratinocyte terminal differentiation via activation of type I transglutaminase. *J. Biol. Chem.* 278, 48066–48073.
- (50) Sturniolo, M. T., Chandraratna, R. A. S., and Eckert, R. L. (2005) A novel transglutaminase activator forms a complex with type I transglutaminase. *Oncogene* 24, 2963–2972.
- (51) Duvic, M., Helekar, B., Schulz, C., Cho, M., DiSepio, D., Hager, C., DiMao, D., Hazarika, P., Jackson, B., Breuer-McHam, J., Young, J., Clayman, G., Lippman, S. M., Chandraratna, R. A. S., Robinson, N. A., Deucher, A., Eckert, R. L., and Nagpal, S. (2000) Expression of a retinoid-inducible tumor suppressor, tazarotene-inducible gene-3, is decreased in psoriasis and skin cancer. *Clin. Cancer Res.* 6, 3249 LP – 3259.
- (52) Uyama, T., Kawai, K., Kono, N., Watanabe, M., Tsuboi, K., Inoue, T., Araki, N., Arai, H., and Ueda, N. (2015) Interaction of phospholipase A/acyltransferase-3 with Pex19p: a possible involvement in the down-regulation of peroxisomes. *J. Biol. Chem.* 290, 17520–17534.
- (53) Frauenfelder, H., Sligar, S. G., and Wolynes, P. G. (1991) The energy landscapes and motions of proteins. *Science* (80-.). 254, 1598 LP – 1603.
- (54) Ferreiro, D. U., Hegler, J. A., Komives, E. A., and Wolynes, P. G. (2007) Localizing frustration in native proteins and protein assemblies. *Proc. Natl. Acad. Sci. U. S. A.* 104, 19819–19824.
- (55) Jensen, M. R., Ruigrok, R. W. H., and Blackledge, M. (2013) Describing intrinsically disordered proteins at atomic resolution by NMR. *Curr. Opin. Struct. Biol.* 23, 426–435.
- (56) Kempf, J. G., and Loria, J. P. (2002) Protein dynamics from solution NMR. *Cell Biochem. Biophys.* 37, 187–211.
- (57) Kay, L. E. (1998) Protein dynamics from NMR. *Nat. Struct. Biol.* 5 Suppl, 513–517.

(58) Nirmala, N. R., and Wagner, G. (1988) Measurement of ^{13}C relaxation times in proteins by two-dimensional heteronuclear ^1H - ^{13}C correlation spectroscopy. *J. Am. Chem. Soc.* *110*, 7557–7558.

(59) Nirmala, N. R., and Wagner, G. (1989) Measurement of ^{13}C spin-spin relaxation times by two-dimensional heteronuclear ^1H - ^{13}C correlation spectroscopy. *J. Magn. Reson.* *82*, 659–661.

(60) Palmer, A. G., Rance, M., and Wright, P. E. (1991) Intramolecular motions of a zinc finger DNA-binding domain from Xfin characterized by proton-detected natural abundance carbon-13 heteronuclear NMR spectroscopy. *J. Am. Chem. Soc.* *113*, 4371–4380.

(61) Farrow, N. A., Muhandiram, R., Singer, A. U., Pascal, S. M., Kay, C. M., Gish, G., Shoelson, S. E., Pawson, T., Forman-Kay, J. D., and Kay, L. E. (1994) Backbone dynamics of a free and a phosphopeptide-complexed Src homology 2 domain studied by ^{15}N NMR relaxation. *Biochemistry* *33*, 5984–6003.

(62) Lipari, G., and Szabo, A. (1982) Model-free approach to the interpretation of nuclear magnetic resonance relaxation in macromolecules. 1. Theory and range of validity. *J. Am. Chem. Soc.* *104*, 4546–4559.

(63) Lipari, G., and Szabo, A. (1982) Model-free approach to the interpretation of nuclear magnetic resonance relaxation in macromolecules. 2. Analysis of experimental results. *J. Am. Chem. Soc.* *104*, 4559–4570.

(64) d’Auvergne, E. J., and Gooley, P. R. (2003) The use of model selection in the model-free analysis of protein dynamics. *J. Biomol. NMR* *25*, 25–39.

(65) Mandel, A. M., Akke, M., and Palmer Arthur G., I. I. I. (1995) Backbone dynamics of Escherichia coli ribonuclease HI: correlations with structure and function in an active enzyme. *J. Mol. Biol.* *246*, 144–163.

(66) Barbato, G., Ikura, M., Kay, L. E., Pastor, R. W., and Bax, A. (1992) Backbone dynamics of calmodulin studied by nitrogen-15 relaxation using inverse detected two-dimensional NMR spectroscopy: the central helix is flexible. *Biochemistry* *31*, 5269–5278.

(67) Freedberg, D. I., Ishima, R., Jacob, J., Wang, Y.-X., Kustanovich, I., Louis, J. M., and Torchia, D. A. (2002) Rapid structural fluctuations of the free HIV protease flaps in solution: relationship to crystal structures and comparison with predictions of dynamics calculations.

Protein Sci. 11, 221–232.

(68) Kalodimos, C. G., Biris, N., Bonvin, A. M. J. J., Levandoski, M. M., Guennuegues, M., Boelens, R., and Kaptein, R. (2004) Structure and flexibility adaptation in nonspecific and specific protein-DNA complexes. *Science* (80-.). 305, 386 LP – 389.

(69) Thorpe, I. F., and Brooks 3rd, C. L. (2007) Molecular evolution of affinity and flexibility in the immune system. *Proc. Natl. Acad. Sci. U. S. A.* 104, 8821–8826.

(70) Zimmermann, J., Oakman, E. L., Thorpe, I. F., Shi, X., Abbyad, P., Brooks 3rd, C. L., Boxer, S. G., and Romesberg, F. E. (2006) Antibody evolution constrains conformational heterogeneity by tailoring protein dynamics. *Proc. Natl. Acad. Sci. U. S. A.* 103, 13722–13727.

(71) Das, R., Chowdhury, S., Mazhab-Jafari, M. T., Sildas, S., Selvaratnam, R., and Melacini, G. (2009) Dynamically driven ligand selectivity in cyclic nucleotide binding domains. *J. Biol. Chem.* 284, 23682–23696.

(72) Peng, T., Zintsmaster, J. S., Namanja, A. T., and Peng, J. W. (2007) Sequence-specific dynamics modulate recognition specificity in WW domains. *Nat. Struct. & Mol. Biol.* 14, 325.

(73) Akke, M., Brueschweiler, R., and Palmer, A. G. (1993) NMR order parameters and free energy: an analytical approach and its application to cooperative calcium(2+) binding by calbindin D9k. *J. Am. Chem. Soc.* 115, 9832–9833.

(74) Yang, D., and Kay, L. E. (1996) Contributions to conformational entropy arising from bond vector fluctuations measured from NMR-derived order parameters: application to protein folding. *J. Mol. Biol.* 263, 369–382.

(75) HAMMES, G. G. (1964) Mechanism of enzyme catalysis. *Nature* 204, 342–343.

(76) Eisenmesser, E. Z., Millet, O., Labeikovsky, W., Korzhnev, D. M., Wolf-Watz, M., Bosco, D. A., Skalicky, J. J., Kay, L. E., and Kern, D. (2005) Intrinsic dynamics of an enzyme underlies catalysis. *Nature* 438, 117–121.

(77) Henzler-Wildman, K. A., Thai, V., Lei, M., Ott, M., Wolf-Watz, M., Fenn, T., Pozharski, E., Wilson, M. A., Petsko, G. A., Karplus, M., Hübner, C. G., and Kern, D. (2007) Intrinsic motions along an enzymatic reaction trajectory. *Nature* 450, 838.

- (78) Palmer, A. G. (2015) Enzyme dynamics from NMR spectroscopy. *Acc. Chem. Res.* 48, 457–465.
- (79) Korzhnev, D. M., Religa, T. L., Banachewicz, W., Fersht, A. R., and Kay, L. E. (2010) A transient and low-populated protein-folding intermediate at atomic resolution. *Science* (80-). 329, 1312 LP – 1316.
- (80) Neudecker, P., Robustelli, P., Cavalli, A., Walsh, P., Lundström, P., Zarrine-Afsar, A., Sharpe, S., Vendruscolo, M., and Kay, L. E. (2012) Structure of an intermediate state in protein folding and aggregation. *Science* (80-). 336, 362 LP – 366.
- (81) Kimsey, I. J., Petzold, K., Sathyamoorthy, B., Stein, Z. W., and Al-Hashimi, H. M. (2015) Visualizing transient Watson-Crick-like mispairs in DNA and RNA duplexes. *Nature* 519, 315–320.
- (82) Libich, D. S., Tugarinov, V., and Clore, G. M. (2015) Intrinsic unfoldase/foldase activity of the chaperonin GroEL directly demonstrated using multinuclear relaxation-based NMR. *Proc. Natl. Acad. Sci. U. S. A.* 112, 8817–8823.
- (83) Franco, R., Gil-Caballero, S., Ayala, I., Favier, A., and Brutscher, B. (2017) Probing conformational exchange dynamics in a short-lived protein folding intermediate by real-time relaxation–dispersion NMR. *J. Am. Chem. Soc.* 139, 1065–1068.
- (84) Sugase, K., Dyson, H. J., and Wright, P. E. (2007) Mechanism of coupled folding and binding of an intrinsically disordered protein. *Nature* 447, 1021.
- (85) Schneider, R., Maurin, D., Communie, G., Kragelj, J., Hansen, D. F., Ruigrok, R. W. H., Jensen, M. R., and Blackledge, M. (2015) Visualizing the molecular recognition trajectory of an intrinsically disordered protein using multinuclear relaxation dispersion NMR. *J. Am. Chem. Soc.* 137, 1220–1229.
- (86) Pratihar, S., Sabo, T. M., Ban, D., Fenwick, R. B., Becker, S., Salvatella, X., Griesinger, C., and Lee, D. (2016) Kinetics of the antibody recognition site in the third IgG-binding domain of protein G. *Angew. Chemie Int. Ed.* 55, 9567–9570.
- (87) Xiao, T., Fan, J., Zhou, H., Lin, Q., and Yang, D. (2016) Local unfolding of fatty acid binding protein to allow ligand entry for binding. *Angew. Chemie Int. Ed.* 55, 6869–6872.
- (88) Zhao, B., Guffy, S. L., Williams, B., and Zhang, Q. (2017) An excited state underlies gene regulation of a transcriptional riboswitch. *Nat. Chem. Biol.* 13, 968–974.

- (89) Delaforge, E., Kragelj, J., Tengo, L., Palencia, A., Milles, S., Bouvignies, G., Salvi, N., Blackledge, M., and Jensen, M. R. (2018) Deciphering the dynamic interaction profile of an intrinsically disordered protein by NMR exchange spectroscopy. *J. Am. Chem. Soc.* *140*, 1148–1158.
- (90) Akke, M., and Palmer, A. G. (1996) Monitoring macromolecular motions on microsecond to millisecond time scales by $R1\rho$ - $R1$ constant relaxation time NMR spectroscopy. *J. Am. Chem. Soc.* *118*, 911–912.
- (91) Massi, F., and Peng, J. W. (2018) Characterizing protein dynamics with NMR $R1\rho$ relaxation experiments, in *Methods in Molecular Biology*, pp 205–221. Humana Press Inc.
- (92) Fawzi, N. L., Ying, J., Torchia, D. A., and Clore, G. M. (2010) Kinetics of amyloid beta monomer-to-oligomer exchange by NMR relaxation. *J. Am. Chem. Soc.* *132*, 9948–9951.
- (93) Kovermann, M., Rogne, P., and Wolf-Watz, M. (2016) Protein dynamics and function from solution state NMR spectroscopy. *Q. Rev. Biophys.* *49*, e6.
- (94) Carr, H. Y., and Purcell, E. M. (1954) Effects of diffusion on free precession in nuclear magnetic resonance experiments. *Phys. Rev.* *94*, 630–638.
- (95) Meiboom, S., and Gill, D. (1958) Modified spin-echo method for measuring nuclear relaxation times. *Rev. Sci. Instrum.* *29*, 688–691.
- (96) Palmer, A. G., Kroenke, C. D., and Patrick Loria, J. (2001) Nuclear magnetic resonance methods for quantifying microsecond-to-millisecond motions in biological macromolecules, in *Nuclear Magnetic Resonance of Biological Macromolecules - Part B* (James, T. L., Dötsch, V., and Schmitz, U. B. T.-M. in E., Eds.), pp 204–238. Academic Press.
- (97) Vallurupalli, P., Bouvignies, G., and Kay, L. E. (2012) Studying “invisible” excited protein states in slow exchange with a major state conformation. *J. Am. Chem. Soc.* *134*, 8148–8161.
- (98) Vallurupalli, P., Sekhar, A., Yuwen, T., and Kay, L. E. (2017) Probing conformational dynamics in biomolecules via chemical exchange saturation transfer: a primer. *J. Biomol. NMR* *67*, 243–271.
- (99) Gopalan, A. B., Hansen, D. F., and Vallurupalli, P. (2018) CPMG experiments for protein minor conformer structure determination BT - protein NMR: methods and protocols (Ghose, R., Ed.), pp 223–242. Springer New York, New York, NY.

- (100) Sauerwein, A. C., and Hansen, D. F. (2015) Relaxation dispersion NMR spectroscopy BT - protein NMR: modern techniques and biomedical applications (Berliner, L., Ed.), pp 75–132. Springer US, Boston, MA.
- (101) van Zijl, P. C. M., and Yadav, N. N. (2011) Chemical exchange saturation transfer (CEST): what is in a name and what isn't? *Magn. Reson. Med.* *65*, 927–948.
- (102) Lokesh, N., Seegerer, A., Hioe, J., and Gschwind, R. M. (2018) Chemical exchange saturation transfer in chemical reactions: a mechanistic tool for NMR detection and characterization of transient intermediates. *J. Am. Chem. Soc.* *140*, 1855–1862.
- (103) Korzhnev, D. M., Salvatella, X., Vendruscolo, M., Di Nardo, A. A., Davidson, A. R., Dobson, C. M., and Kay, L. E. (2004) Low-populated folding intermediates of Fyn SH3 characterized by relaxation dispersion NMR. *Nature* *430*, 586–590.
- (104) Vallurupalli, P., Hansen, D. F., Stollar, E., Meirovitch, E., and Kay, L. E. (2007) Measurement of bond vector orientations in invisible excited states of proteins. *Proc. Natl. Acad. Sci.* *104*, 18473 LP – 18477.
- (105) Neudecker, P., Lundström, P., and Kay, L. E. (2009) Relaxation dispersion NMR spectroscopy as a tool for detailed studies of protein folding. *Biophys. J.* *96*, 2045–2054.
- (106) Ishima, R. (2014) CPMG relaxation dispersion BT - protein dynamics: methods and protocols (Livesay, D. R., Ed.), pp 29–49. Humana Press, Totowa, NJ.
- (107) Hansen, A. L., Lundström, P., Velyvis, A., and Kay, L. E. (2012) Quantifying millisecond exchange dynamics in proteins by CPMG relaxation dispersion NMR using side-chain ¹H probes. *J. Am. Chem. Soc.* *134*, 3178–3189.
- (108) Vallurupalli, P. (2010) Structure and dynamics of protein excited states with millisecond lifetimes. *J. Indian Inst. Sci.*
- (109) Hansen, D. F., Vallurupalli, P., Lundström, P., Neudecker, P., and Kay, L. E. (2008) Probing chemical shifts of invisible states of proteins with relaxation dispersion NMR spectroscopy: how well can we do? *J. Am. Chem. Soc.* *130*, 2667–2675.
- (110) Bouvignies, G., Korzhnev, D. M., Neudecker, P., Hansen, D. F., Cordes, M. H. J., and Kay, L. E. (2010) A simple method for measuring signs of (¹H (N) chemical shift differences between ground and excited protein states. *J. Biomol. NMR* *47*, 135–141.

(111) Kruschel, D., and Zagrovic, B. (2009) Conformational averaging in structural biology: issues, challenges and computational solutions. *Mol. Biosyst.* 5, 1606–1616.

(112) Case, D. A. (2002) Molecular dynamics and NMR spin relaxation in proteins. *Acc. Chem. Res.* 35, 325–331.

(113) Fiset, O., Lagüe, P., Gagné, S., and Morin, S. (2012) Synergistic applications of MD and NMR for the study of biological systems. *J. Biomed. Biotechnol.* 2012, 254208.

(114) Ren, X., Lin, J., Jin, C., and Xia, B. (2010) ¹H, ¹³C and ¹⁵N resonance assignments of human H-REV107 N-terminal domain. *Biomol. NMR Assign.* 4, 175–178.

(115) Wang, L., Yu, W., Ren, X., Lin, J., Jin, C., and Xia, B. (2012) ¹H, ¹³C, and ¹⁵N resonance assignments of the N-terminal domain of human TIG3. *Biomol. NMR Assign.* 6, 201–203.

2

Chapter

Sub-second ¹⁵N backbone dynamics reveal differences between PLAAT3 and PLAAT4.

The work in this chapter was published as: Chatterjee, S. D., Zhou, J., Dasgupta, R., Cramer-Blok, A., Timmer, M., van der Stelt, M., and Ubbink, M. (2021) Protein Dynamics Influence the Enzymatic Activity of Phospholipase A/Acyltransferases 3 and 4. *Biochemistry* 60, 1178–1190.

Abstract

PLAAT3 and PLAAT4, despite being homologs, clearly differ in substrate specificity, activity and physiological roles. The effect of the amino acid differences on protein dynamics between the two enzymes were studied. Thermostability experiments revealed that PLAAT3 is inherently more thermostable than PLAAT4 owing to a well dispersed mesh of salt bridges. Despite having similar molecular weights, T_c was observed to be higher for PLAAT4 owing to an elongated structure. Fast timescale NMR dynamics confirmed the presence of a highly disordered loop in both enzymes while PLAAT3 was observed to be quite non-flexible otherwise. Globally, PLAAT4 was found to be more dynamic and low order parameters were observed in the active site region indicating a dynamic active site. Slow timescale dynamics also confirmed a presence of a dynamic active site in PLAAT4, absent in PLAAT3.

Introduction

Phospholipases A/acyltransferases (PLAATs) are a family of enzymes that are sequentially homologous and structurally similar to lecithin:retinol acyltransferase (LRAT).¹ Due to its resemblance to LRAT, they are also part of the bigger eukaryotic superfamily of NlpC/P60.² They were identified as enzymes due to their similarities in structure with LRAT.² In human tissues, the genes of five members of the PLAATs are expressed and the enzymes are named as PLAAT1 to PLAAT5, although many other names exist in the literature. The enzymes were originally discovered as class II tumor suppressors³⁻⁵ and were named as HRAS-like suppressor (HRASLS).^{6,7} HRASLS genes are ubiquitously expressed in most normal tissues, but downregulated in most types of tumor cells.⁸ The relationship between the tumor suppressor function and acyltransferase activity remains unclear.⁹

In the past several years, it was reported that all five members possess phospholipase A1/A2 activity (hydrolysis of the *sn-1* or *sn-2* ester bonds of PtdCho or PtdEt) and N-acyl phosphatidylethanolamines (NAPE)-forming N-acyltransferase activity, which releases an acyl group from the *sn-1* or *sn-2* position of phosphatidylcholine (PtdCho) and/or transfers it to phosphatidylethanolamine (PtdEt) in

a Ca^{2+} -independent manner, see Figure 2.1C.¹⁰ These enzymes also have O-acyltransferase (AT) activity (transfer of an acyl group from PtdCho to the hydroxyl group of lyso PtdCho.^{1,6,7} PLAAT3 and PLAAT4 both contain the N-terminal NlpC/P60 domain and have conserved sequences, showing 58% identity and 72% similarity (Figure 2.1A). They have the characteristic NCEHFV motif of PLAATs, in which C represents C113, the nucleophile that forms a catalytic triad with two histidine residues. H23 acts as a base and H35 as the stabilizer (Figure 2.1D).^{1,2,7} Xiaobai *et al.* have previously determined the solution structure (PDB: 2KYT) of the N-terminal domain (NTD) of PLAAT3 (PLAAT3N, residues 1–125),¹¹ revealing that PLAAT3N adopts a fold highly similar to those of the NlpC/P60 peptidase domains (Figure 2.1B). The same group also reported the solution structure of the NTD of PLAAT4 (PLAAT4N, residues 1–125, PDB ID: 2MY9).¹² The crystal structure of the NTD of PLAAT3 has been reported by Golczack *et al.* (PDB ID: 4DPZ) with a similar fold to that of the NMR structure (RMSD 0.74 for the $\text{C}\alpha$ atoms of the non-flexible residues). The flexible loop and a few other residues could not be observed due to disorder.¹

The two proteins comprise of six β strands and three (PLAAT3) or four (PLAAT4) α helices and one large loop (residues 38-57) that connects two β strands. We introduce minor modifications to the naming conventions of the secondary structural elements published in^{11,12}, see Table 2.1, Figure 2.2). We have included the nomenclature for two main loops L1 (residues 38-57) and L2 (residue 100-109/110) and the β strand B6 (residues 103-104) as a part of the loop L2 and thus renamed as L2(B6).

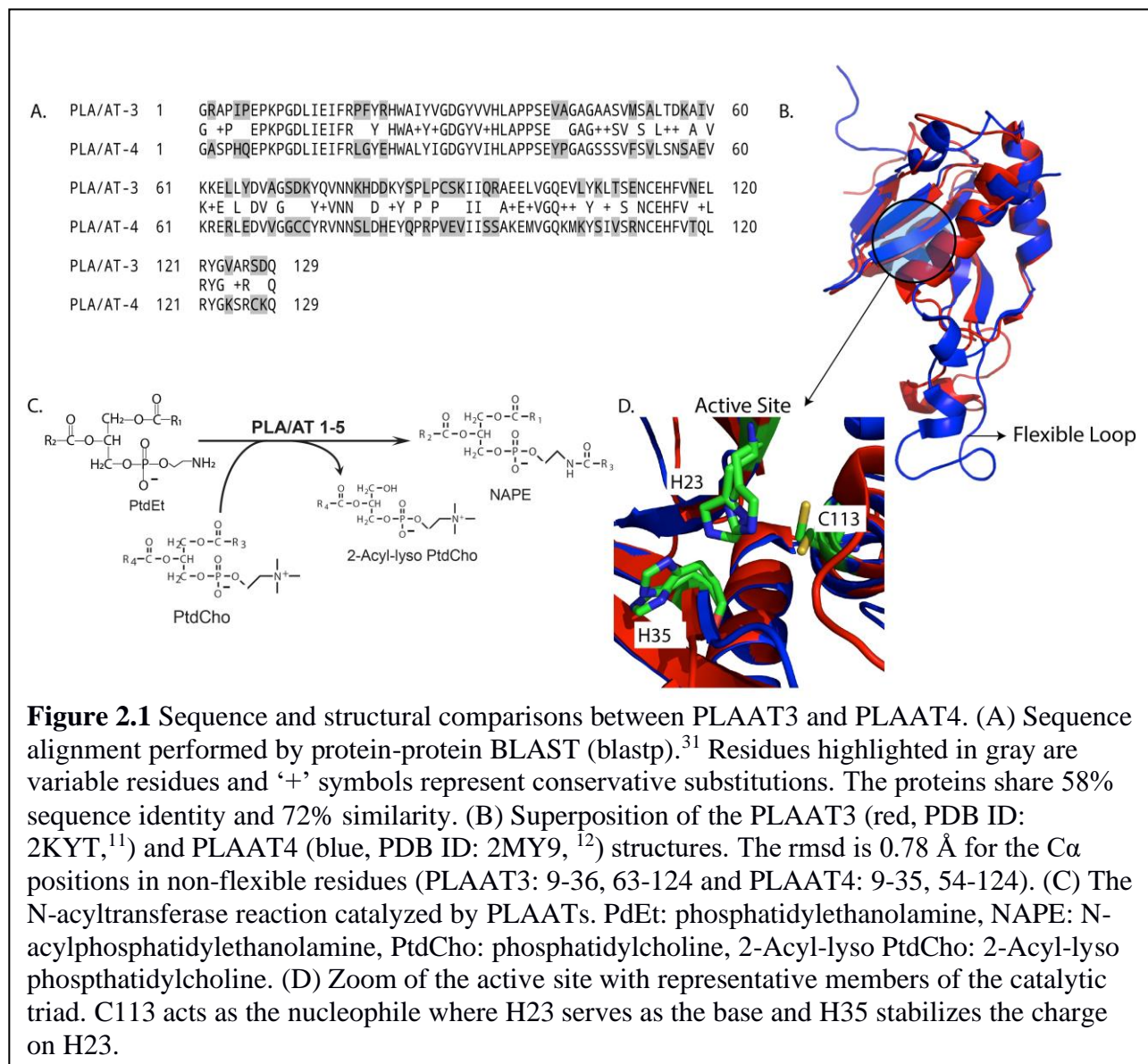


Table 2.1. Modified nomenclature of the secondary structural elements of PLAAT3 and PLAAT4. N: N-terminal residues, B: β -strand, L: loop, A: α -helix, C: C-terminal residues.

PLAAT3		PLAAT4	
Name	Residues	Residues	Name
N	1-12	N	1-10
B1	13-18	B1	13-17
B2	21-29	B2	23-29
B3	32-37	B3	32-37
L1	38-57	L1	38-57

B4	58-64	B4	58-64
A1	65-68	A1	65-69
B5	73-76	B5	73-76
A2	89-99	A2'	79-82
L2(B6)	100-109	A2	89-99
A3	110-122	L2(B6)	100-110
C	123-125	A3	112-122
		C	123-125

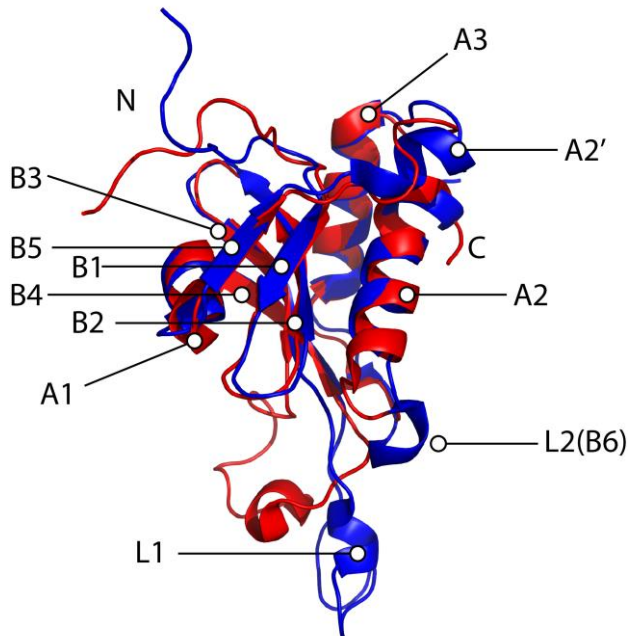


Figure 2.2 Modified nomenclature of PLAAT3 (red, PDB ID: 2KYT) and PLAAT4 (blue, PDB ID: 2MY9) according to Table 2.1.

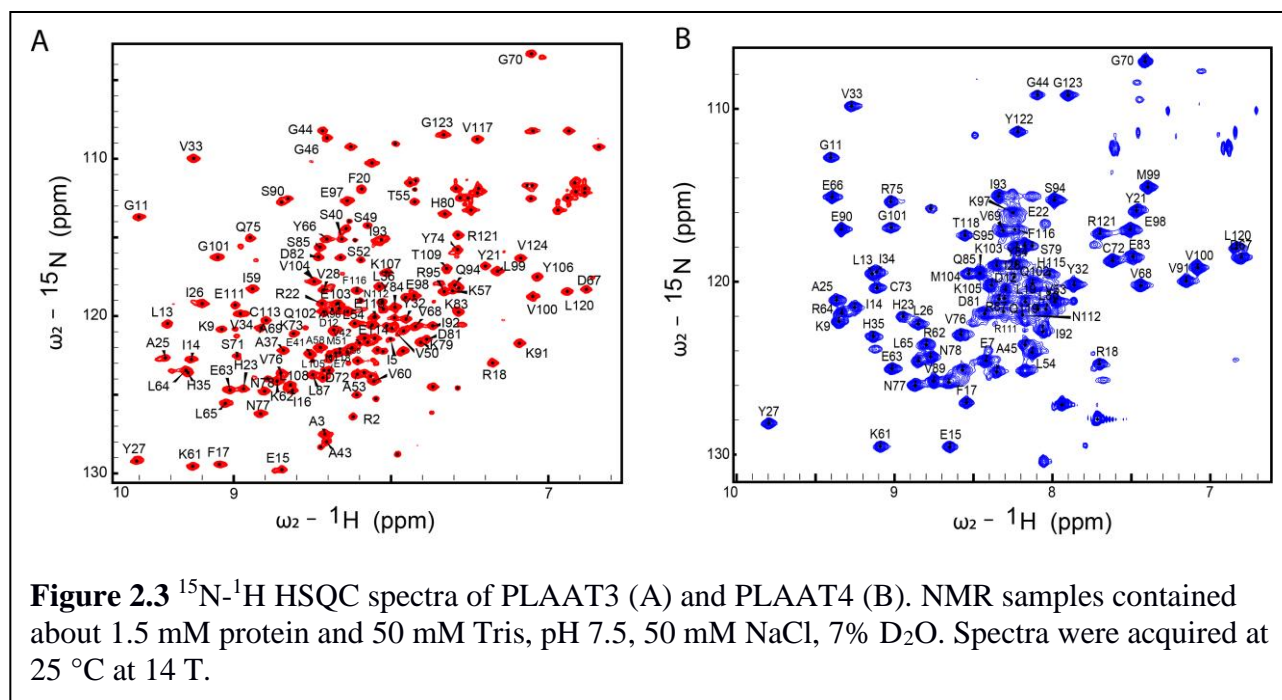
Despite having similar amino acid sequences and structural homology, PLAAT3 and PLAAT4 differ greatly in activity. Uyama *et al.* reported a difference in phospholipase activity between full length PLAAT3 and PLAAT4 and stated that PLAAT3 has a maximal activity that is 4.8-fold larger than that of PLAAT4 in the mammalian cell homogenates.¹³ This was confirmed by Pang *et al.* using full length MBP-PLAAT3 fusion proteins to assay the phospholipase activity with fluorescent BODIPY-labelled substrates dissolved in liposomes.¹⁴ Interestingly, Golczak *et al.* showed the opposite in case of the soluble NTDs of these PLAATs, using short chain phosphatidylcholines as substrates and tracking the intermediates using mass spectrometry.¹ Clearly, despite the structural similarities, the activity depends both on the exact sequence (PLAAT3 or -4) and the state (truncated – full length). Given the structural similarity between PLAAT3 and -4, we wondered whether differences in protein dynamics could explain the differences in activity. The dynamics of the soluble NTDs of PLAAT3 and PLAAT4 were studied using NMR spectroscopy on the fast, nanosecond, and slower, millisecond timescales. Such experiments are very demanding in terms of sample quality, size and stability, so we decided to work, at least initially, on the truncated N-terminal soluble part of the protein. From now onwards, any reference to PLAAT3 or PLAAT4 will therefore refer to the truncated versions of the proteins. The results show significant differences in dynamics in these two proteins, especially around the active site in PLAAT4.

Results

To characterize the differences in dynamics between PLAAT3 and PLAAT4, the melting temperature and the mobility of various timescales was determined. The N-terminal domains of PLAATs were expressed and purified by procedure mentioned in Materials and Methods.

Thermostability. A thermofluor-based assay was carried out to determine the melting temperatures (T_m) of PLAAT3 and PLAAT4 using the hydrophobic fluorescent probe SYPRO ORANGE. The T_m values were found to be $78.0 (\pm 0.5)^\circ\text{C}$ for PLAAT3 and $62.5 (\pm 0.5)^\circ\text{C}$ for PLAAT4. The large difference of 15°C suggests that PLAAT3 has a more rigid structure with strong inter-residue, noncovalent interactions.

^{15}N - ^1H HSQC spectra. NMR samples of PLAAT3 and PLAAT4 were prepared by producing ^{15}N -labelled proteins in *E. coli* BL21-DE3 pLys, with yields of around 40 mg/L. Concentrations of around 1.5 mM could be reached for NMR data acquisition. ^{15}N - ^1H HSQC spectra of PLAAT3 and PLAAT4 were assigned based on the published data,^{15,16} using the BMRB depositions (see Materials and Methods and Figure 2.3). Fewer resonances are observed in the spectrum of PLAAT4 than for that of PLAAT3, which suggests that more amides are mobile on the millisecond timescale or their protons in rapid exchange with the solvent, causing line broadening due to chemical exchange.

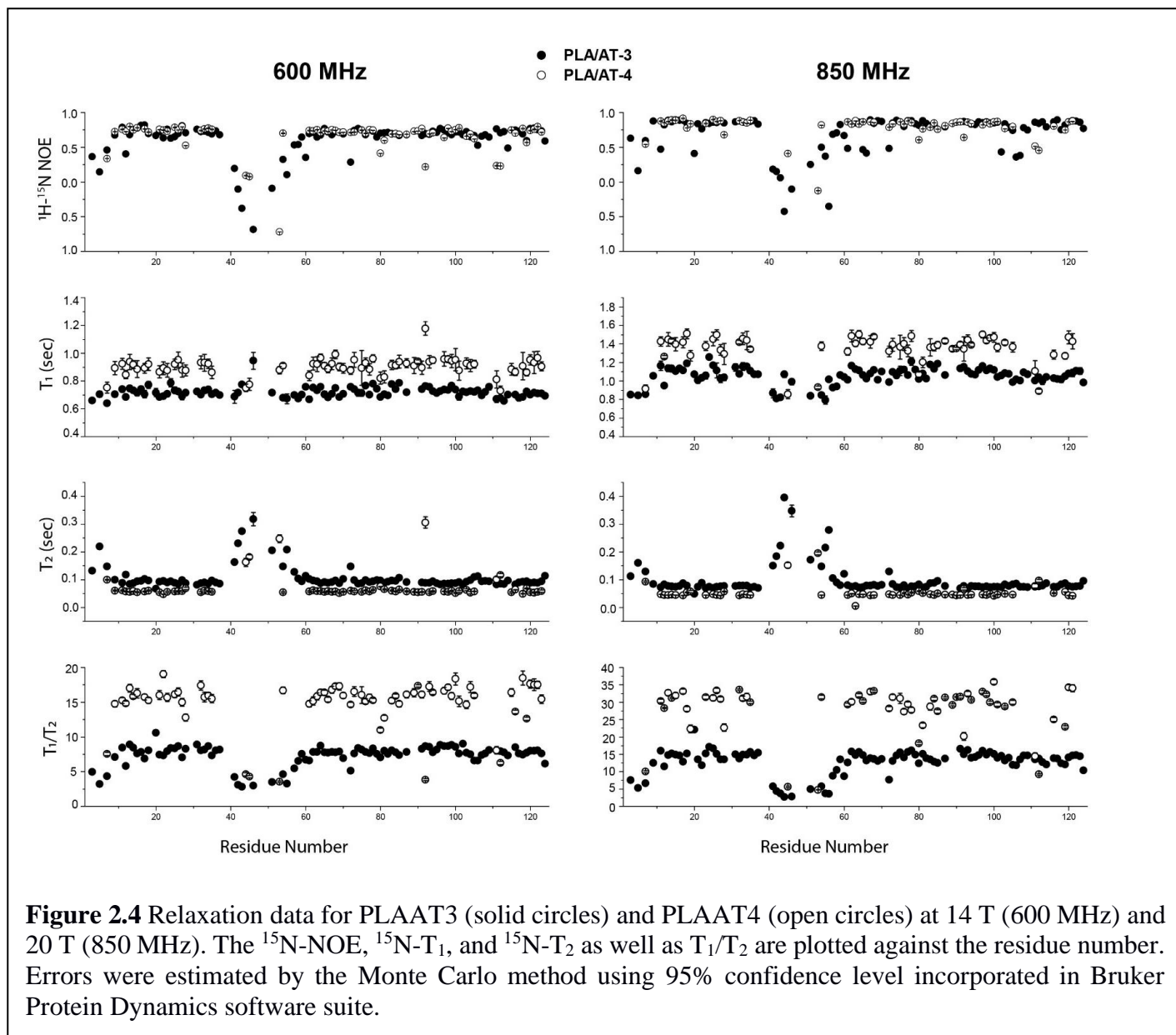


Fast motions. To determine the motions of PLAAT3 and PLAAT4 at pico-nanosecond timescale, the ^{15}N backbone amide T_1 , T_2 and heteronuclear NOE parameters were determined at 14 T (600 MHz ^1H frequency) and 20 T (850 MHz). The data are presented in Figure 2.4 and Table S2.1(a-d). Relaxation parameters could be determined for 98 residues of PLAAT3 and 71 residues of PLAAT4. It is clear that the T_1/T_2 ratio is much larger for PLAAT4 than for PLAAT3, suggesting that the rotational correlation times differ, even though the two proteins have similar molecular weights. The low NOE values of L1 in both proteins indicate that this loop is highly disordered, which is in line with previous findings.^{1,11,12} Due to the flexibility of the N-terminus and loop L1, the NOE and T_2 values of those regions differ much from the rigid parts of the proteins and should not be considered for the average T_1 , average T_2 and average NOE calculations. Therefore, we calculated the 20% trimmed average values of T_1 , T_2 and NOE, given in Table 2.2. Trimmed average NOE and T_1 values for PLAAT4 were higher than for PLAAT3 and T_2 values for PLAAT4 were lower.

To determine the rotational correlation times (τ_c) by Bruker Protein Dynamics software suite, three criteria were applied to exclude highly flexible residues. First, only residues with NOE values > 0.65 were included. Second, the T_1 value had to be within one standard deviation and, third, the T_2 is not much larger than the mean, $[(T_2 - T_{2,\text{mean}})/T_2 < 3 * (T_1 - T_{1,\text{mean}})/T_1]$. The derived rotational correlation times are 8.4 ns and 12.5 ns for PLAAT3 and -4, respectively. This is remarkable, because both proteins have similar molecular weights, of 14.4 kDa and 14.7 kDa, respectively, and the NMR solutions and temperature were same for both proteins. Theoretical estimations of average τ_c from all models in the NMR ensemble structures (2kyt.pdb¹¹ for PLAAT3 and 2my9.pdb¹² for PLAAT4) using HYDRONMR¹⁷ yield 9 ± 1 ns and 11 ± 1 ns, respectively, values close to experimentally determined ones. PLAAT3 is more globular with a compact structure, perhaps due to a distributed network of 17 salt bridges, whereas PLAAT4 is a more elongated molecule with only 10 salt bridges, concentrated in certain parts of the protein, as illustrated in Fig. 2.5. It can also not be excluded that PLAAT4 has a tendency for transient self-interactions under the high concentration (1.5 mM) used in the NMR samples, leading to a higher τ_c . Residues with NOE values below two standard deviation of the trimmed average were identified as residues showing internal motions and residues with T_1/T_2 ratios two standard deviation above or below the trimmed mean were identified as exhibiting additional motion. The residues demonstrating fast timescale dynamics are mapped on the structures of both proteins (Figure 2.6). Also, residues for which resonances are not found in the spectra are indicated, as these are likely to be involved in motions or exchange processes.

Table 2.2. 20% trimmed average and standard deviation in brackets of T_1 , T_2 and NOE values of PLAAT3 and PLAAT4 obtained at 14 T (600 MHz) and 20 T (850 MHz) experiments. The rotational correlation time τ_c for PLAAT3 was calculated using subsets of 40 (600 MHz) or 57 residues (850 MHz). For PLAAT4, τ_c subsets of 33 (600 MHz) and 37 residues (850 MHz) were used.

	600MHz			850 MHz		
	T_1 (ms)	T_2 (ms)	NOE	T_1 (ms)	T_2 (ms)	NOE
PLAAT3						
20% Trimmed Mean	720(2)	90(1)	0.66(0.01)	1060(5)	80(2)	0.78(0.02)
τ_c	8.5(0.2) ns			8.2(0.4) ns		
PLAAT4						
20% Trimmed Mean	900(4)	50(8)	0.71(0.01)	1380(10)	40(1)	0.83(0.01)
τ_c	12.6(0.3) ns			12.5(0.4) ns		



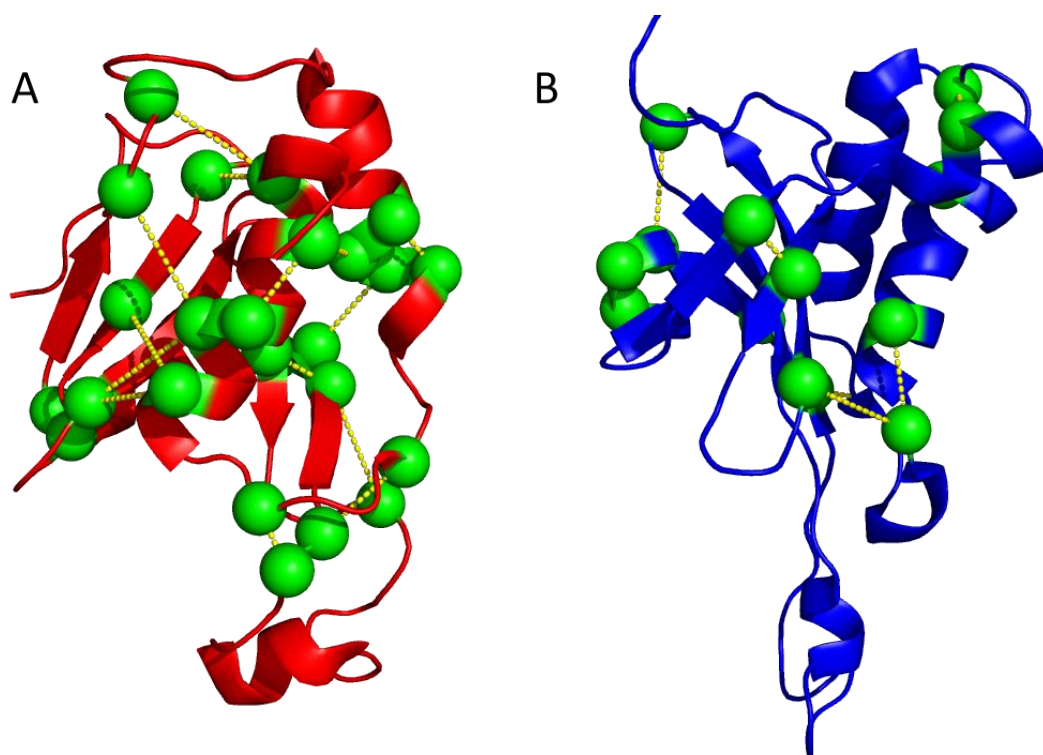
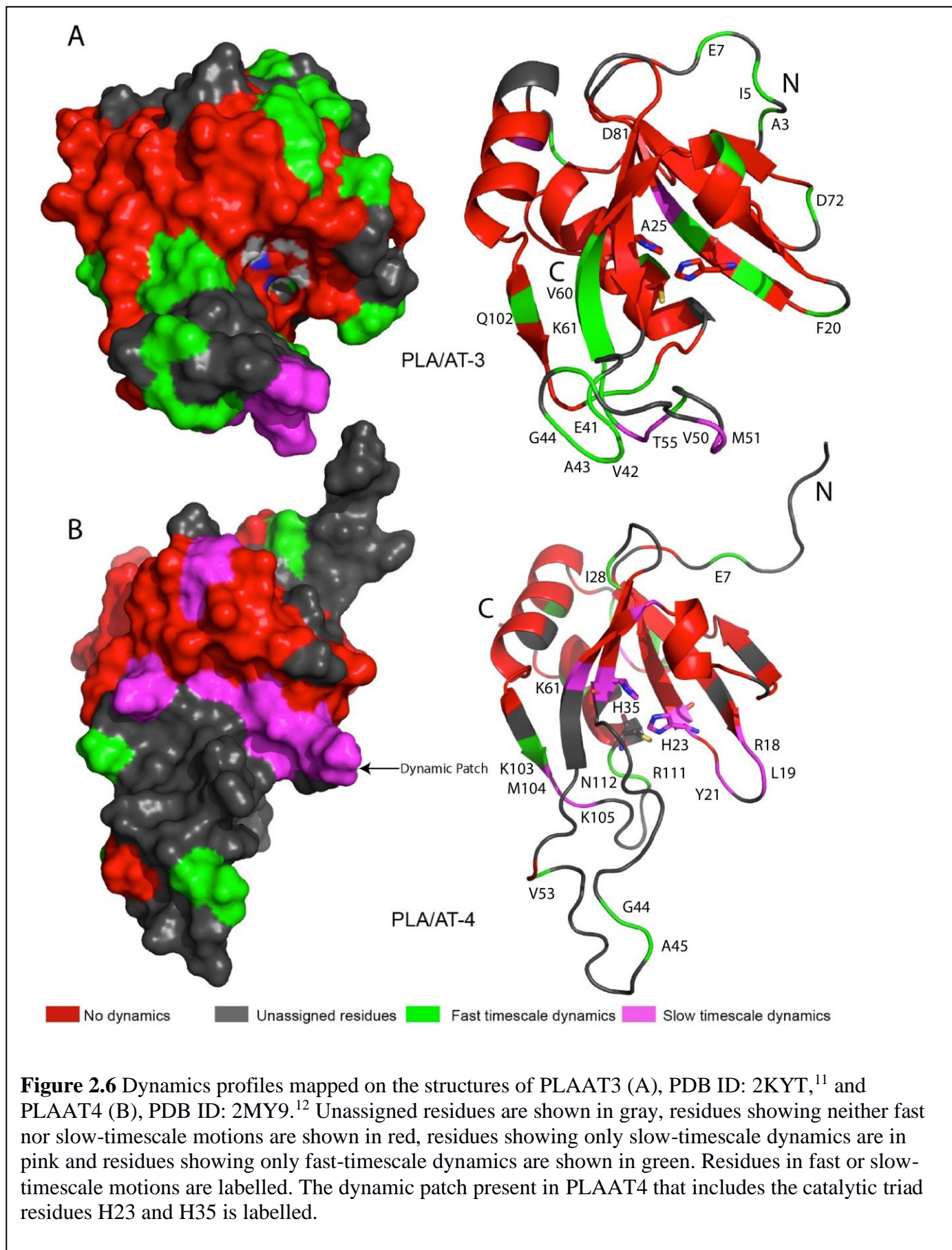
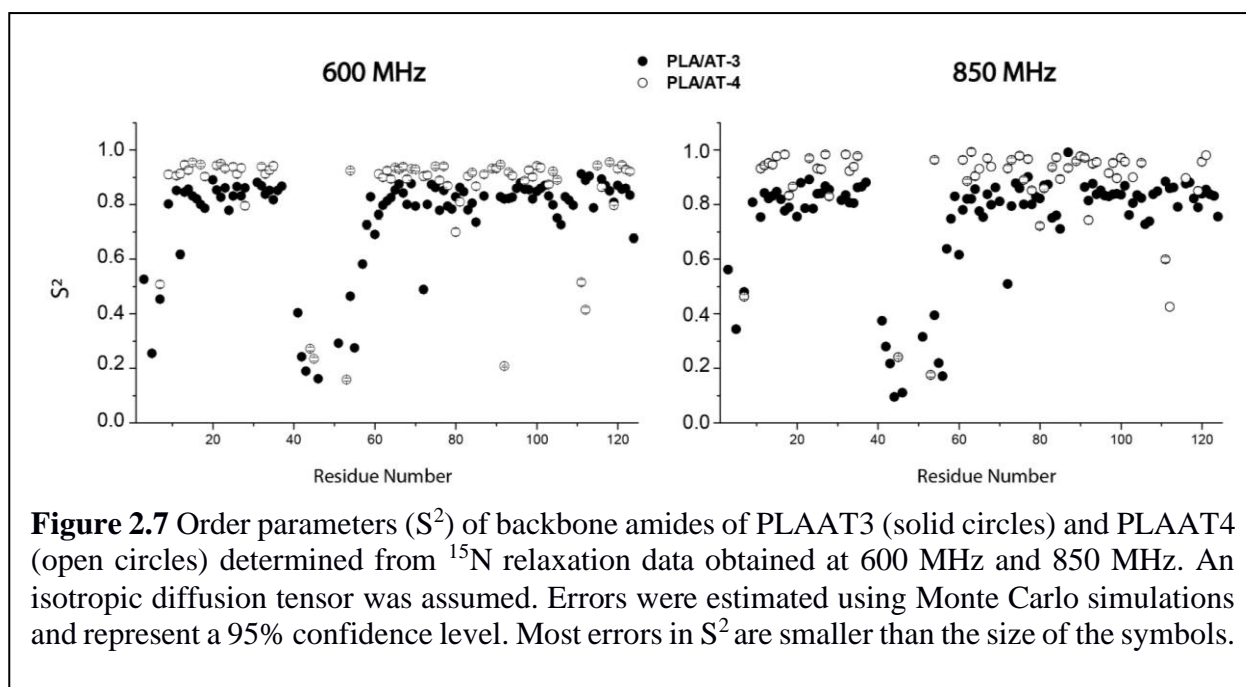


Figure 2.5 Representation of salt bridge networks (yellow dashes) in PLAAT3 (PDB ID: 2KYT) (A) and PLAAT4 (PDB ID: 2MY9) (B). Salt bridges were defined as a pair of basic and acidic residues with a nitrogen and an oxygen atom of the basic and acidic sidechains, respectively, within 3.2 Å in at least one of the 20 NMR structures. Green spheres represent the C α atoms of the bridged residues.



The Lipari-Szabo model-free method^{18,19} was used to derive the order parameters (S^2) of the backbone amides from the ^{15}N relaxation data. Only the model that allowed fitting of S^2 and the time constant of the fast dynamics (τ_e) was used, to avoid overfitting (see Materials and Methods). The order parameters are plotted in Figure 2.7 and the results are listed in Table S2.2 (a-b). Clearly, the presence of fast dynamics in the N-termini and the flexible loops is confirmed and several more isolated low S^2 values indicate local dynamics, in particular in PLAAT4 around residues I92, R111 and N112. The S^2 values for the rigid parts of PLAAT4 are quite high (on average 0.95). It is unclear what the reason is. It is observed for all rigid residues, suggesting that the underlying model of an



isolated two-spin system in an isotropically rotating protein is not fully valid in the case of PLAAT4. Inclusion of the anisotropy of rotation of the NMR solution structure did not resolve this issue. As will be discussed below, the flexible loop in PLAAT4 assumes on average a more extended conformation than in PLAAT3 and is highly dynamic, which may lead to artificially high τ_e and S^2 values.

Slow motions. To probe backbone motions in the millisecond timescale, we acquired ^{15}N -CPMG relaxation dispersion experiments for both proteins at 14 T and 20 T. Five residues of PLAAT3 showed weak relaxation dispersion (Figure S2.1). Three residues (V50, M51 and D56) are in the highly disordered loop L1, one residue (D81) in the loop joining B5 and A2 and another residue (W24) was in B2 (S3), see Figure 2.6. In contrast, twelve residues of PLAAT4 showed evidence for

millisecond dynamics (Figures 2.8 and S2.2). PLAAT4 has a well-defined dynamic region consisting of 6 residues, R18, L19, Y21, K61 and the catalytic triad members H23 and H35, see Figure 2.6. No resonance could be assigned to C113, the catalytic cysteine. The relaxation data of this region were fitted globally to a two-site exchange model, yielding a population (p_B) of 1% for the minor state and an exchange rate (k_{ex}) of $1.9 (0.2) \times 10^3 \text{ s}^{-1}$ (Figure 2.8). Dynamic parameters of residues in both PLAAT3 and PLAAT4 are listed in Table S2.3.

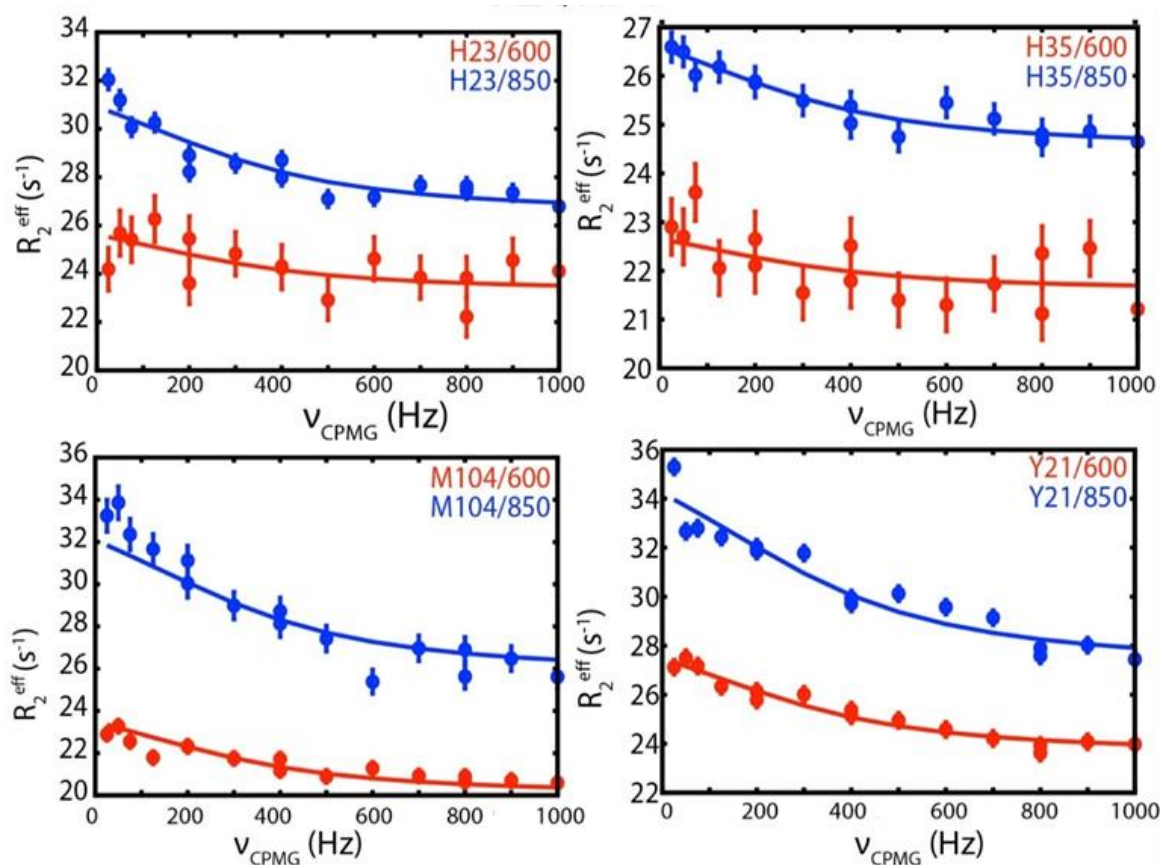


Figure 2.8 Examples of relaxation dispersion curves observed for PLAAT4. The effective transverse relaxation rates are plotted against the CPMG frequency for four residues. The red and blue curves represent data acquired at 14 T and 20 T, respectively. The experimental data are indicated by circles. The errors represent the uncertainties in estimation of effective transverse relaxation rate, based on three duplicate points. The solid lines indicate a fit to the two-state exchange model with a k_{ex} of $1.9 (0.2) \times 10^3 \text{ s}^{-1}$ and p_B of 1%. All dispersion curves for PLAAT3 and PLAAT4 are presented in Supplementary Figure S2.3

Discussion

Golczak *et al.*¹ demonstrated that the N-terminal portion of PLAAT4 catalyzes short chain phosphatidylcholines faster than N-terminal portion of PLAAT3 and that the rate of hydrolysis of acyl intermediate is much faster in PLAAT4. Xia *et al.*¹² reported that C-terminal domains (CTDs) of PLAAT4 and PLAAT3 can independently induce HeLa cell death at a comparable level, while their NTDs play opposite roles in regulating the cell death activity of CTDs, even though the structures of PLAAT4N and PLAAT3N are highly similar, with a rmsd of 0.78 Å (PDB entries 2KYT and 2MY9). They hypothesized that such functional difference is probably due to different NTD/CTD interaction patterns between PLAAT4 and PLAAT3. Since the difference should come from the 28% sequence dissimilarity, we studied differences in the dynamics of the NTDs of these proteins. The melting temperature of PLAAT3 is 15 °C higher than that of PLAAT4 and the rotational correlation time is 33% shorter. Thus, PLAAT3 is a more stable and compact protein than PLAAT4. A comparison of the structures shows that the former has a more extensive network of salt bridges dispersed throughout the structure while the latter has lesser salt bridges and that too confined to certain regions, which could explain these observations (Figure 2.5).

Both proteins feature a large loop (L1) that is known to be disordered,^{1,11,12,20} and is shown here to be mobile on the pico-nanosecond timescale. It has been proposed that L1 is a membrane anchoring loop in the full length protein.²⁰ It was shown that replacement of L1 in PLAAT3 by the equivalent loop of LRAT leads to induction of Vitamin A metabolism. This indicates that the highly disordered loop might play a role in modulating activity by interacting with the membrane.

Interesting differences are found between PLAAT3 and PLAAT4 around the active site. PLAAT4 shows low order parameters for R111 and N112, which immediately precede the catalytic nucleophile C113. Since there are no resonance assignments for residues 106-110 and 113-114, we assume that the peaks of these residues are lacking because of broadening due to motional chemical exchange. Millisecond timescale dynamics experiments identified a dynamic active site region involving residues 18, 19, 21, 23, 35 and 61. The resonance of G20 is missing, again indicative of exchange broadening. Residue E22, which forms a salt bridge with R111, shows no broadening due to chemical exchange, which could imply that it either is not dynamic or its change in chemical shift ($\Delta\omega$) happens to be small. Thus, the active site region of PLAAT4 is dynamic, involving at least residues 18-23, 35, 61 and also 113-114. Such a dynamic patch is not observed in PLAAT3. We speculate that the difference in dynamics can explain the activity differences observed PLAAT3 and PLAAT4. The

NTD of PLAAT3 may show little activity toward its substrate due to lack of active site dynamics, whereas the dynamics of PLAAT4 may enable its activity. To develop a model of what the dynamics in PLAAT4 may entail, molecular dynamics simulations can be used. Although they can only sample fast dynamics, they may still provide insight into the nature of motions. Such calculations are known to correlate with NMR relaxation studies.²¹⁻²⁴ These studies are the subject of the next chapter.

Materials and methods

Protein production. DNA sequences encoding the human N-terminal soluble form (residues 1–125) of PLAAT3 or PLAAT4 (Uniprot ID P53816 and Q9UL19, respectively) with N-terminal His₆ tag and a TEV cleavage site were ordered from GeneArt. The fragments were inserted in-frame into bacterial expression vector pET-28a using the *Nco*I and *Xho*I restriction sites. Chemically competent *Escherichia coli* BL21-DE3pLys cells were transformed with the plasmids for protein production. The bacteria were cultured overnight in 50 mL of LB medium with 50 µg/mL kanamycin at 37°C under shaking. For ¹⁵N-labeling, 5 mL of the overnight pre-culture was transferred to 500 mL minimal medium with 50 µg/mL kanamycin. When the OD₆₀₀ reached 0.6, the temperature was lowered to 22°C and gene expression was induced by addition of 0.5 mM IPTG. The culture was incubated for 5 hours before cells were harvested by centrifugation at 6000 rpm at 4°C. The pellet was resuspended in 5 mL of 50 mM Tris-HCl buffer (pH 7.5) followed by freezing at -80°C overnight. The cells were thawed the next day in presence of DNase I and lysozyme and lysed by French press. The lysate was centrifuged at 4°C at 25000g for 45 min. The supernatant of the cell lysate containing the His₆-tagged soluble protein was then loaded on a HiTrap-Nickel column, equilibrated with 50 mM Tris pH 7.5, 500 mM NaCl and 5 mM Imidazole. The protein was eluted using a linear imidazole concentration gradient from 0 to 0.5 M. The collected fractions were pooled and dialyzed overnight using a 3.5 kDa molecular weight cut-off cellulose membrane at 4°C in 50 mM Tris, pH 7.5, 500 mM NaCl, 0.5mM EDTA buffer to remove imidazole. His₆-tagged TEV protease was added for the cleavage of the His₆-tag on PLAAT during dialysis overnight. The mixture was loaded again on a His₆-Trap Nickel column to collect the N-terminal PLAAT3 and PLAAT4 domains. The buffer was changed into 50 mM Tris-HCl, 50 mM NaCl, 10 mM DTT, pH 7.5. The volume of the sample was reduced to 2.5 mL using a 5 kDa MWCO Amicon Ultracentrifugal filter (EMD Millipore) at 2200 g and 15°C. The concentrated sample was loaded on and eluted from a Superose12 gel filtration column in 30 mM sodium phosphate buffer with 30 mM NaCl and 10 mM DTT at pH 7.0. All NMR samples contained 1.5 mM uniformly ¹⁵N -labeled protein in this buffer with 7% D₂O added for lock.

Thermofluor-based melting temperature (T_m) analysis. Thermofluor analysis was performed on a CFX96 Real-Time PCR system (Bio-Rad) to determine the thermal stability of PLAAT proteins. Duplicate protein samples of 25 µL were prepared in 30 mM sodium phosphate buffer (pH 7.0), 25 mM sodium chloride and 10 mM DTT in 96-well Concord Polycarbonate PCR plates (Bio-Rad) using SYPRO Orange (Sigma-Aldrich) as a fluorescent probe. After sealing with Optical-Quality Sealing Tape (Bio-Rad), plates were vortexed and centrifuged for 30 seconds using an MPS 1000 Mini PCR

Plate Spinner (Labnet). Melting curves were obtained by detection of fluorescence using the FRET channel of the RT-PCR machine. The temperature was increased in steps of 0.5°C increments. At each point, the sample was incubated for 30 s before measuring the fluorescence. At the end the reaction was stopped by heating at 90 °C for 5 min. The results were analyzed in CFX Manager 3.1 (Bio-Rad). The temperature corresponding to the maximum of the first derivative of the melting curve was taken to be the melting temperature (T_m).

T₁, T₂, NOE measurements. NMR experiments were carried out at 25°C on 600 MHz and 850 MHz Bruker Avance III spectrometers equipped with TCI cryoprobes at 600 MHz and 850 MHz proton larmor frequency. Standard Bruker pulse sequences were used for T_1 (hsqct1etf3gpsitc3d), T_2 (hsqct2etf3gpsitc3d) and NOE (hsqcnoef3gpsi) experiments. ¹⁵N-¹H NOE spectra were acquired first acquired in an interleaved fashion and then split into two HSQCs with and without amide proton saturation each containing 2048/200 points in the ¹H/¹⁵N dimensions.

In the T_1 and T_2 experiments water saturation was avoided using low power water-flip-back pulses. The mixing times used for the determination of T_1 were 0.01s(x2), 0.16s, 0.22s, 0.35s(x2), 0.48s, 0.6s, 0.8s(x2), 1.0s, 1.2s with duplicates for error estimation. Mixing times for T_2 determination were 0s, 0.034(x2)s, 0.05s, 0.07(x2)s, 0.085s, 0.10, 0.135(x2)s, 0.17s, 0.2(x2)s and 0.24s. All spectra were processed with Bruker TOPSPIN with QSine and Gaussian window functions and linear prediction applied to the ¹⁵N dimension. NOE values were calculated as the ratio of peak intensities in the experiment with and without proton saturation. To obtain T_1 and T_2 values the experimental data points (peak heights) were fitted to a curve $I_0 \cdot \exp(-t/T_1$ or $T_2)$ where I_0 is the peak intensity of the reference spectra (0s) and fit parameter errors were estimated using Monte Carlo simulations. All NOE, T_1 and T_2 analyses were performed on Bruker Protein Dynamics software suite.

Resonance assignments. ¹H-¹⁵N HSQC spectra of PLAAT3 and PLAAT4 were assigned using BMRB entries 16883 and 18012, respectively.^{15,16}

Relaxation dispersion measurements. Constant relaxation time CPMG experiments were performed for the backbone ¹⁵N nuclei of PLAAT3 and PLAAT4 using a modified ST-CW CPMG pulse sequence. A series of two-dimensional (2D) spectra with 1024/60 complex points (¹H/¹⁵N) were recorded with a relaxation delay (T_{relax}) of 40 ms and cpmg frequencies set to 100, 200(x2), 300, 400(x2), 500, 600, 700, 800(x2), 900 and 1000 Hz, run in an interleaved fashion, followed by a reference spectrum with $T_{relax} = 0$. Duplicates (x2) were used to estimate the effective transverse

relaxation rate ($R_{2,eff}$) error. The spectra were zero-filled and Fourier transformed with linear prediction applied in the ^{15}N dimension and Gaussian weighting functions applied along the ^1H and ^{15}N dimensions, respectively. Peaks were fitted with FuDa (Hansen, <http://www.biochem.ucl.ac.uk/hansen/fuda/>) to obtain intensities, and $R_{2,eff}$ were calculated from the calculated peak intensities using the formula: $R_{2,eff}(v_{\text{CPMG}}) = -1/T_{\text{relax}} \cdot \ln(I(v_{\text{CPMG}})/I_0)$, where I_0 is the peak intensity in the reference spectrum. The $R_{2,eff}$ values were corrected for R_1 -contribution using the formula described by Jiang *et al.*²⁵ with $0.95 \text{ s}^{-1} R_1$ - and 10.5 s^{-1} as an estimate for R_2 -contribution for all residues. Finally, the resulting relaxation dispersion profiles of residues that show dispersion obtained at two fields were fitted to Carver-Richards equation and modeled to a two-state model by using CATIA (Hansen, <http://www.biochem.ucl.ac.uk/hansen/catia/>), k_{ex} and p_{B} were obtained as the global output of CATIA whereas $\Delta\omega$ were obtained for individual residues in the fit.

Model-free analysis. Automated model free analysis was performed using Bruker Protein Dynamics software suite. The NH bond length was set to 1.02 \AA and the NH chemical shift anisotropy was set to -172 ppm . To ensure good model fitting, calculated errors in T_1 , T_2 and NOE were overridden with an error of 2%, as the calculated errors were smaller due to very high signal to noise. The software performs the following actions: Using the two-field T_1 , T_2 and NOE datasets, the global correlation time (τ_c) and reduced spectral densities $j(0)$, $j(\omega_{\text{N}})$, $j(0.87\omega_{\text{H}})$ were calculated. The reduced spectral densities were then used to estimate the order parameters (S^2), the ratio D_{\parallel}/D_{\perp} of the diffusion tensor and relaxation exchange (R_{ex}) parameters for each residue. Estimation of τ_c required exclusion of dynamic residues which was done by excluding all residues with NOE values less than 0.65 residues with T_2 smaller than the difference between mean and one standard deviation and residues with large T_2 values as compared to T_1 since these residues might undergo conformational exchange. The T_1 , T_2 and NOE values of each residue were fitted to two of 4 models assuming isotropic modelling: M1(S^2) and M2(S^2 , τ_c).^{18,26-30}

Theoretical calculation of τ_c . Theoretical hydrodynamic calculation to determine the τ_c was done using the program HYDRONMR.¹⁷ Ensemble structures from PDB entries 2KYT and 2MY9 were used as input for atomic coordinates. The effective radius of atomic elements was set to 3.1 \AA , the temperature to 25°C and solvent viscosity to 9.1 mP to match our experimental conditions. N-H bonds with explicit hydrogens were chosen as the source of the dipole vectors to calculate the NMR parameters and dipolar couplings. The gyromagnetic ratio of N was set to $-2.7126 \times 10^7 \text{ rad s}^{-1}\text{T}^{-1}$, the N-H distance was set to 1.02 \AA and the CSA was set to -172 ppm . τ_c was calculated for two

magnetic fields, 14 T and 20 T to match our experimental data. The average τ_c was then calculated from the individual τ_c of each ensemble structures.

Supplementary:**Table S2.1A** Relaxation parameters of PLAAT3 obtained from T_1 , T_2 , and ^1H - ^{15}N NOE experiments at 600 MHz.

PLAAT3 600 MHz						
Residue	NOE	Error	T_1 [s]	Error	T_2 [s]	Error
A3	0.363	0.002	0.658	0.013	0.132	0.003
I5	0.143	0.002	0.705	0.021	0.219	0.007
E7	0.459	0.002	0.639	0.012	0.147	0.003
K9	0.671	0.003	0.704	0.021	0.100	0.006
G11	0.785	0.003	0.740	0.022	0.087	0.003
D12	0.403	0.001	0.685	0.009	0.118	0.002
L13	0.681	0.003	0.747	0.022	0.084	0.003
I14	0.753	0.003	0.732	0.020	0.086	0.002
E15	0.774	0.003	0.717	0.023	0.094	0.004
I16	0.814	0.002	0.742	0.023	0.095	0.003
F17	0.822	0.003	0.706	0.026	0.103	0.005
R18	0.694	0.003	0.772	0.025	0.096	0.003
F20	0.668	0.003	0.716	0.029	0.068	0.003
Y21	0.720	0.002	0.686	0.016	0.092	0.002
R22	0.632	0.002	0.692	0.017	0.094	0.002
H23	0.760	0.003	0.707	0.020	0.089	0.002
W24	0.629	0.002	0.787	0.030	0.093	0.003
A25	0.650	0.003	0.734	0.023	0.088	0.003
I26	0.695	0.002	0.723	0.018	0.083	0.002
Y27	0.808	0.003	0.690	0.025	0.098	0.005
V28	0.705	0.003	0.714	0.020	0.086	0.003
G31	0.757	0.003	0.725	0.022	0.082	0.003
Y32	0.723	0.002	0.700	0.015	0.087	0.002
V33	0.728	0.003	0.733	0.022	0.090	0.003
V34	0.713	0.003	0.738	0.022	0.085	0.002
H35	0.689	0.002	0.705	0.021	0.096	0.003
L36	0.737	0.003	0.716	0.020	0.089	0.003
A37	0.681	0.002	0.699	0.018	0.086	0.002
E41	0.194	0.003	0.686	0.046	0.162	0.009
V42	-0.103	0.001	0.715	0.012	0.230	0.004
A43	-0.379	0.002	0.774	0.020	0.274	0.009
G44	-1.095	0.006	1.136	0.119	0.000	0.000
G46	-0.683	0.004	0.945	0.061	0.317	0.024
M51	-0.090	0.002	0.716	0.017	0.206	0.004
L54	0.323	0.002	0.680	0.015	0.147	0.002
T55	0.101	0.002	0.673	0.035	0.207	0.008
D56	-1.190	0.009	0.993	0.129	0.000	0.000
K57	0.534	0.001	0.700	0.012	0.128	0.002
A58	0.539	0.002	0.672	0.012	0.103	0.002
I59	0.645	0.003	0.702	0.017	0.093	0.002
V60	0.354	0.002	0.759	0.017	0.113	0.003
K61	0.693	0.003	0.669	0.021	0.101	0.004
K62	0.712	0.002	0.752	0.016	0.096	0.002
E63	0.648	0.002	0.731	0.016	0.093	0.003
L64	0.676	0.002	0.759	0.017	0.087	0.002
L65	0.767	0.003	0.705	0.022	0.091	0.003
Y66	0.717	0.002	0.681	0.017	0.088	0.002
D67	0.676	0.002	0.707	0.014	0.090	0.002

V68	0.724	0.002	0.748	0.016	0.096	0.002
A69	0.714	0.002	0.685	0.014	0.087	0.002
G70	0.692	0.002	0.706	0.017	0.101	0.002
D72	0.287	0.001	0.758	0.010	0.147	0.002
K73	0.739	0.002	0.740	0.016	0.098	0.002
Y74	0.769	0.003	0.714	0.023	0.085	0.003
Q75	0.745	0.003	0.714	0.024	0.087	0.003
V76	0.680	0.002	0.766	0.016	0.098	0.002
N77	0.753	0.003	0.702	0.016	0.091	0.002
N78	0.731	0.002	0.779	0.015	0.094	0.002
K79	0.644	0.002	0.744	0.019	0.098	0.002
H80	0.703	0.002	0.685	0.017	0.097	0.002
D81	0.709	0.002	0.703	0.015	0.088	0.002
D82	0.710	0.002	0.695	0.014	0.092	0.002
K83	0.698	0.002	0.778	0.016	0.096	0.002
Y84	0.696	0.002	0.740	0.013	0.095	0.002
S85	0.668	0.002	0.785	0.014	0.107	0.002
L87	0.677	0.002	0.718	0.017	0.091	0.003
K91	0.670	0.002	0.740	0.018	0.089	0.002
I92	0.695	0.003	0.765	0.021	0.088	0.002
I93	0.686	0.003	0.758	0.019	0.088	0.002
Q94	0.732	0.002	0.726	0.013	0.093	0.002
R95	0.714	0.002	0.712	0.013	0.087	0.002
A96	0.767	0.002	0.728	0.013	0.082	0.002
E97	0.744	0.003	0.737	0.016	0.085	0.002
E98	0.709	0.002	0.734	0.012	0.085	0.001
L99	0.679	0.002	0.767	0.018	0.087	0.002
V100	0.720	0.002	0.738	0.014	0.086	0.002
G101	0.721	0.003	0.688	0.025	0.091	0.003
Q102	0.677	0.002	0.723	0.013	0.080	0.002
E103	0.726	0.001	0.719	0.007	0.093	0.001
V104	0.653	0.003	0.727	0.019	0.097	0.003
L105	0.665	0.002	0.720	0.018	0.109	0.003
Y106	0.529	0.002	0.733	0.015	0.111	0.002
K107	0.655	0.002	0.695	0.017	0.094	0.002
L108	0.679	0.002	0.720	0.016	0.095	0.003
T109	0.646	0.003	0.757	0.022	0.093	0.003
E111	0.761	0.003	0.669	0.024	0.083	0.003
N112	0.708	0.002	0.675	0.016	0.085	0.002
C113	0.721	0.002	0.656	0.017	0.084	0.002
E114	0.486	0.002	0.702	0.018	0.096	0.002
F116	0.747	0.003	0.702	0.018	0.082	0.002
V117	0.729	0.003	0.679	0.021	0.090	0.003
N118	0.689	0.002	0.685	0.014	0.092	0.002
E119	0.596	0.002	0.723	0.015	0.093	0.002
L120	0.769	0.002	0.703	0.015	0.088	0.002
R121	0.777	0.003	0.716	0.018	0.089	0.002
Y122	0.753	0.003	0.711	0.020	0.088	0.002
G123	0.737	0.003	0.710	0.017	0.094	0.002
V124	0.589	0.002	0.693	0.016	0.113	0.002

Table S2.1B Relaxation parameters of PLAAT3 obtained from T₁, T₂, and ¹H-¹⁵N NOE experiments at 850 MHz.

PLAAT3 850 MHz						
Residue	NOE	Error	T1[s]	Error	T2[s]	Error
A3	0.630	0.001	0.851	0.012	0.112	0.002
I5	0.161	0.001	0.845	0.032	0.160	0.001
E7	0.592	0.001	0.858	0.013	0.129	0.002
K9	0.876	0.002	1.055	0.007	0.084	0.002
G11	0.469	0.001	1.164	0.050	0.073	0.000
D12	0.818	0.001	0.951	0.017	0.083	0.001
L13	0.888	0.002	1.137	0.034	0.077	0.001
I14	0.867	0.002	1.134	0.037	0.075	0.000
E15	0.892	0.002	1.107	0.010	0.074	0.001
I16	0.885	0.002	1.137	0.017	0.077	0.001
F17	0.885	0.002	1.115	0.016	0.087	0.001
R18	0.842	0.001	1.189	0.028	0.078	0.001
F20	0.406	0.001	1.073	0.016	0.049	0.000
Y21	0.835	0.001	1.008	0.034	0.074	0.001
R22	0.765	0.002	1.033	0.007	0.087	0.001
H23	0.854	0.002	1.057	0.037	0.069	0.001
W24	0.841	0.002	1.258	0.016	0.073	0.001
A25	0.860	0.002	1.167	0.023	0.070	0.001
I26	0.853	0.001	1.114	0.078	0.074	0.001
Y27	0.881	0.002	1.025	0.043	0.076	0.001
V28	0.849	0.002	1.039	0.033	0.077	0.002
G31	0.863	0.002	1.148	0.040	0.077	0.002
Y32	0.877	0.002	1.077	0.009	0.078	0.001
V33	0.864	0.002	1.155	0.043	0.078	0.001
V34	0.852	0.002	1.158	0.009	0.078	0.001
H35	0.872	0.002	1.110	0.020	0.071	0.001
L36	0.883	0.002	1.073	0.017	0.073	0.001
A37	0.830	0.002	1.072	0.015	0.069	0.001
E41	0.184	0.001	0.867	0.050	0.151	0.004
V42	0.148	0.001	0.809	0.004	0.184	0.003
A43	0.061	0.001	0.824	0.014	0.222	0.004
G44	-0.425	0.002	1.071	0.033	0.395	0.009
G46	-0.106	0.002	0.992	0.034	0.347	0.021
M51	0.250	0.001	0.838	0.024	0.171	0.002
L54	0.498	0.001	0.850	0.011	0.148	0.005
T55	0.368	0.001	0.795	0.043	0.215	0.001
D56	-0.353	0.002	1.015	0.022	0.279	0.005
K57	0.685	0.001	0.927	0.006	0.105	0.000
A58	0.705	0.001	0.942	0.005	0.090	0.001
I59	0.827	0.002	1.064	0.024	0.079	0.001
V60	0.669	0.001	1.043	0.021	0.121	0.002
K61	0.480	0.001	1.013	0.017	0.080	0.002
K62	0.834	0.001	1.164	0.028	0.074	0.001
E63	0.847	0.001	1.128	0.018	0.077	0.001
L64	0.859	0.001	1.115	0.014	0.071	0.001
L65	0.464	0.001	1.063	0.030	0.072	0.001
Y66	0.414	0.001	1.025	0.019	0.078	0.001
D67	0.895	0.001	1.080	0.024	0.078	0.000
V68	0.842	0.001	1.116	0.015	0.082	0.002
A69	0.882	0.002	1.013	0.007	0.077	0.001
G70	0.868	0.001	1.103	0.017	0.081	0.001
D72	0.483	0.001	0.989	0.021	0.129	0.002

K73	0.850	0.002	1.097	0.010	0.084	0.000
Y74	0.889	0.002	1.060	0.029	0.072	0.000
Q75	0.865	0.002	1.110	0.051	0.071	0.001
V76	0.798	0.002	1.125	0.030	0.080	0.001
N77	0.880	0.002	1.062	0.019	0.068	0.001
N78	0.879	0.002	1.212	0.042	0.075	0.001
K79	0.834	0.001	1.124	0.009	0.075	0.001
H80	0.815	0.001	1.022	0.013	0.083	0.001
D81	0.880	0.002	1.082	0.007	0.072	0.000
D82	0.840	0.001	1.027	0.008	0.074	0.001
K83	0.809	0.001	1.177	0.022	0.087	0.000
Y84	0.826	0.001	1.133	0.032	0.088	0.001
S85	0.759	0.001	1.185	0.020	0.094	0.001
L87	0.790	0.002	1.062	0.010	0.077	0.001
K91	0.865	0.001	1.134	0.026	0.068	0.001
I92	0.868	0.002	1.151	0.015	0.077	0.001
I93	0.857	0.002	1.107	0.023	0.068	0.001
Q94	0.831	0.001	1.076	0.005	0.077	0.000
R95	0.826	0.001	1.067	0.006	0.075	0.000
A96	0.867	0.001	1.116	0.005	0.076	0.000
E97	0.856	0.001	1.162	0.010	0.072	0.000
E98	0.862	0.001	1.112	0.010	0.075	0.001
L99	0.846	0.001	1.134	0.035	0.073	0.001
V100	0.849	0.001	1.119	0.008	0.074	0.001
G101	0.861	0.002	1.041	0.014	0.074	0.002
Q102	0.432	0.001	1.061	0.024	0.073	0.001
E103	0.835	0.001	1.085	0.011	0.082	0.000
V104	0.786	0.002	1.075	0.010	0.077	0.001
L105	0.741	0.001	0.988	0.018	0.083	0.000
Y106	0.359	0.001	1.015	0.018	0.085	0.002
K107	0.378	0.001	1.006	0.026	0.074	0.001
L108	0.783	0.002	1.092	0.028	0.075	0.001
T109	0.748	0.002	1.073	0.021	0.073	0.001
E111	0.858	0.002	1.002	0.008	0.074	0.001
N112	0.841	0.002	1.039	0.031	0.076	0.001
C113	0.866	0.002	0.999	0.036	0.078	0.001
E114	0.793	0.001	1.040	0.013	0.087	0.001
F116	0.865	0.002	1.028	0.014	0.074	0.001
V117	0.891	0.002	1.020	0.020	0.074	0.001
N118	0.751	0.001	1.017	0.035	0.082	0.000
E119	0.822	0.001	1.050	0.005	0.087	0.001
L120	0.863	0.002	1.080	0.008	0.077	0.001
R121	0.879	0.002	1.086	0.041	0.074	0.001
Y122	0.875	0.002	1.111	0.027	0.075	0.000
G123	0.859	0.002	1.107	0.037	0.077	0.001
V124	0.767	0.001	0.984	0.019	0.095	0.001

Table S2.1C Relaxation parameters of PLAAT4 obtained from T_1 , T_2 , and ^1H - ^{15}N NOE experiments at 600 MHz.

PLAAT4 600 MHz						
Residue	NOE	Error	T_1 [s]	Error	T_2 [s]	Error

Chapter 2

E7	0.338	0.003	0.752	0.041	0.099	0.002
K9	0.724	0.004	0.893	0.048	0.060	0.002
G11	0.756	0.005	0.923	0.039	0.061	0.002
D12	0.727	0.003	0.845	0.030	0.057	0.002
L13	0.800	0.004	0.937	0.056	0.055	0.002
I14	0.748	0.005	0.918	0.028	0.058	0.001
E15	0.779	0.005	0.886	0.062	0.054	0.002
F17	0.765	0.005	0.892	0.036	0.057	0.002
R18	0.720	0.006	0.922	0.046	0.060	0.002
L19	0.693	0.004	0.878	0.080	0.000	0.000
Y21	0.755	0.005	0.866	0.045	0.054	0.003
E22	0.745	0.006	0.892	0.047	0.047	0.000
H23	0.731	0.006	0.877	0.049	0.056	0.003
A25	0.785	0.005	0.920	0.038	0.057	0.002
L26	0.750	0.005	0.952	0.058	0.058	0.002
Y27	0.795	0.005	0.879	0.050	0.059	0.003
I28	0.525	0.003	0.876	0.040	0.068	0.004
Y32	0.741	0.003	0.933	0.047	0.054	0.003
V33	0.763	0.005	0.932	0.060	0.059	0.003
I34	0.775	0.004	0.925	0.034	0.058	0.002
H35	0.759	0.006	0.863	0.044	0.056	0.003
G44	0.094	0.005	0.750	0.027	0.162	0.015
A45	0.076	0.003	0.775	0.044	0.181	0.008
V53	-0.718	0.002	0.879	0.027	0.247	0.014
L54	0.701	0.003	0.909	0.018	0.054	0.003
K61	0.741	0.006	0.839	0.035	0.057	0.002
R62	0.734	0.005	0.925	0.047	0.061	0.004
E63	0.755	0.005	0.921	0.054	0.058	0.002
R64	0.713	0.003	0.966	0.029	0.059	0.003
L65	0.734	0.004	0.909	0.023	0.056	0.002
E66	0.727	0.004	0.888	0.029	0.058	0.002
D67	0.751	0.004	0.924	0.043	0.055	0.002
V68	0.743	0.004	0.992	0.032	0.057	0.002
V69	0.711	0.004	0.900	0.028	0.052	0.003
G70	0.716	0.004	0.891	0.035	0.056	0.002
C72	0.713	0.004	0.877	0.028	0.060	0.002
C73	0.719	0.006	0.953	0.053	0.058	0.004
R75	0.746	0.006	0.894	0.124	0.056	0.003
V76	0.702	0.004	0.930	0.036	0.062	0.002
N77	0.750	0.004	0.883	0.042	0.056	0.003
N78	0.744	0.003	0.962	0.027	0.063	0.002
L80	0.411	0.002	0.821	0.043	0.075	0.001
D81	0.598	0.003	0.829	0.044	0.065	0.002
E83	0.690	0.004	0.916	0.035	0.060	0.002
Y84	0.693	0.004	0.913	0.025	0.057	0.001
Q85	0.684	0.003	0.939	0.047	0.064	0.002
R87	0.686	0.003	0.927	0.033	0.058	0.003
V89	0.729	0.003	0.910	0.058	0.056	0.002
E90	0.733	0.003	0.940	0.013	0.054	0.001
V91	0.766	0.004	0.895	0.047	0.056	0.001
I92	0.217	0.003	1.179	0.050	0.306	0.020
I93	0.695	0.004	0.937	0.044	0.054	0.004
S94	0.705	0.003	0.948	0.023	0.058	0.002
K97	0.637	0.004	0.958	0.052	0.058	0.001
E98	0.773	0.004	0.957	0.024	0.056	0.002

M99	0.728	0.004	0.943	0.047	0.059	0.002
V100	0.754	0.004	0.953	0.081	0.052	0.002
G101	0.778	0.006	0.875	0.069	0.058	0.004
K103	0.659	0.003	0.926	0.039	0.063	0.004
M104	0.689	0.004	0.911	0.043	0.053	0.004
K105	0.621	0.004	0.921	0.028	0.058	0.001
R111	0.235	0.004	0.811	0.062	0.100	0.011
N112	0.231	0.003	0.729	0.034	0.116	0.006
H115	0.748	0.006	0.885	0.042	0.054	0.003
F116	0.701	0.003	0.866	0.028	0.064	0.001
T118	0.769	0.006	0.907	0.099	0.049	0.000
Q119	0.567	0.002	0.861	0.024	0.068	0.001
L120	0.740	0.004	0.952	0.038	0.054	0.003
R121	0.759	0.005	0.932	0.079	0.053	0.002
Y122	0.800	0.006	0.967	0.046	0.055	0.002
G123	0.716	0.005	0.905	0.032	0.059	0.004

Table S2.1D Relaxation parameters of PLAAT4 obtained from T_1 , T_2 , and ^1H - ^{15}N NOE experiments at 850 MHz.

PLAAT4						
850 MHz						
Residue	NOE	Error	T1[s]	Error	T2[s]	Error
E7	0.542	0.003	0.917	0.039	0.092	0.003
K9	0.838	0.003	1.361	0.040	0.000	0.000
G11	0.877	0.004	1.428	0.051	0.047	0.000
D12	0.849	0.002	1.260	0.013	0.045	0.000
L13	0.874	0.003	1.449	0.075	0.044	0.000
I14	0.894	0.004	1.431	0.020	0.046	0.000
E15	0.888	0.004	1.397	0.073	0.044	0.000
F17	0.916	0.004	1.418	0.058	0.043	0.000
R18	0.777	0.005	1.510	0.053	0.054	0.002
L19	0.838	0.003	1.273	0.056	0.057	0.005
Y21	0.867	0.004	1.264	0.058	0.000	0.000
E22	0.845	0.004	1.330	0.086	0.000	0.000
H23	0.843	0.005	1.377	0.048	0.044	0.000
A25	0.899	0.004	1.453	0.073	0.047	0.000
L26	0.870	0.004	1.497	0.054	0.045	0.000
Y27	0.882	0.004	1.335	0.057	0.043	0.000
I28	0.681	0.002	1.292	0.113	0.057	0.002
Y32	0.883	0.003	1.420	0.021	0.042	0.000
V33	0.857	0.004	1.456	0.062	0.047	0.000
I34	0.846	0.003	1.438	0.100	0.046	0.000
H35	0.889	0.004	1.343	0.025	0.045	0.000
A45	0.411	0.003	0.858	0.048	0.152	0.010
V53	-0.125	0.001	0.931	0.014	0.195	0.005
L54	0.819	0.003	1.377	0.047	0.044	0.000
K61	0.867	0.004	1.319	0.040	0.045	0.000
R62	0.833	0.003	1.486	0.062	0.049	0.001
E63	0.879	0.003	1.406	0.035	0.005	0.000
R64	0.834	0.003	1.501	0.043	0.047	0.000
L65	0.864	0.004	1.426	0.035	0.047	0.000

Chapter 2

E66	0.850	0.003	1.311	0.046	0.000	0.000
D67	0.864	0.003	1.424	0.068	0.043	0.000
V68	0.858	0.003	1.478	0.024	0.045	0.000
V69	0.881	0.003	1.373	0.026	0.000	0.000
G70	0.838	0.003	1.344	0.026	0.000	0.000
C72	0.788	0.003	1.321	0.057	0.047	0.000
C73	0.834	0.004	1.391	0.070	0.044	0.000
R75	0.866	0.004	1.367	0.129	0.044	0.000
V76	0.833	0.003	1.399	0.072	0.051	0.001
N77	0.877	0.003	1.325	0.065	0.045	0.000
N78	0.854	0.003	1.485	0.059	0.053	0.002
L80	0.607	0.002	1.070	0.027	0.059	0.002
D81	0.765	0.003	1.203	0.057	0.052	0.002
E83	0.788	0.003	1.363	0.091	0.047	0.000
Y84	0.850	0.003	1.367	0.040	0.044	0.000
Q85	0.759	0.003	1.387	0.038	0.051	0.001
R87	0.810	0.002	1.433	0.023	0.046	0.000
V89	0.842	0.003	1.346	0.026	0.046	0.000
E90	0.859	0.003	1.351	0.011	0.043	0.000
V91	0.863	0.003	1.391	0.030	0.044	0.000
I92	0.641	0.003	1.346	0.131	0.067	0.004
I93	0.860	0.003	1.445	0.056	0.045	0.000
S94	0.842	0.003	1.391	0.019	0.045	0.000
K97	0.821	0.003	1.501	0.036	0.046	0.000
E98	0.860	0.002	1.437	0.027	0.045	0.000
M99	0.837	0.003	1.465	0.029	0.049	0.000
V100	0.864	0.003	1.472	0.054	0.041	0.000
G101	0.870	0.005	1.362	0.044	0.046	0.000
K103	0.767	0.003	1.415	0.025	0.049	0.000
M104	0.755	0.005	1.389	0.100	0.000	0.000
K105	0.795	0.004	1.366	0.052	0.046	0.000
R111	0.514	0.004	1.106	0.116	0.077	0.008
N112	0.456	0.003	0.889	0.024	0.096	0.004
H115	0.853	0.006	1.390	0.363	0.000	0.000
F116	0.801	0.002	1.285	0.049	0.051	0.001
T118	0.917	0.006	1.401	0.104	0.000	0.000
Q119	0.747	0.002	1.272	0.035	0.056	0.001
L120	0.867	0.003	1.471	0.069	0.043	0.000
R121	0.875	0.004	1.429	0.084	0.042	0.000
Y122	0.883	0.004	1.461	0.130	0.000	0.000
G123	0.844	0.004	1.372	0.064	0.000	0.000

Table S2.2A S^2 and τ_e values of PLAAT3 obtained from the model free fit of the relaxation parameters of individual residues obtained at 600 MHz and 850 MHz. M2 and TM2 corresponds to isotropic and anisotropic model free calculations using model 2.

PLAAT3									
600 MHz					850 MHz				
Res	S^2 (M2)	S^2 (TM2)	T_e (M2)	Error	Res	S^2 (M2)	S^2 (TM2)	T_e (M2)	Error
3	0.526	0.527	6.53E-10	2.02e-11	3	0.562	0.575	6E-10	1.75E-11
5	0.254	0.255	7.2E-10	6.99e-12	5	0.343	0.336	4.07E-10	4.56E-12
7	0.453	0.438	8.56E-10	2.00e-11	7	0.479	0.454	6.03E-10	1.38E-11
9	0.802	0.803	7.05E-11	7.43e-12	9	0.808	0.799	1.13E-11	3.28E-12
11	0.851	0.85	4.38E-11	7.50e-12	11	0.754	0.76	8.73E-11	8.61E-12
12	0.618	0.598	5.62E-10	2.75e-11	12	0.843	0.805	3.06E-11	5.02E-12
13	0.845	0.847	9.01E-11	1.26e-11	13	0.822	0.821	6.67E-12	3.51E-12
14	0.856	0.855	6.07E-11	9.34e-12	14	0.831	0.829	1.12E-11	3.74E-12
15	0.832	0.83	4.39E-11	6.54e-12	15	0.847	0.846	7E-12	4.24E-12
16	0.82	0.817	2.69E-11	5.25e-12	16	0.819	0.817	7.41E-12	3.44E-12
17	0.801	0.801	2.37E-11	4.62e-12	17	0.778	0.776	7.55E-12	2.69E-12
18	0.786	0.785	5.34E-11	5.37e-12	18	0.79	0.79	1.28E-11	2.85E-12
20	0.89	0.889	1.88E-10	7.39e-11	20	0.756	0.753	1.38E-10	2.3E-11
21	0.854	0.812	8.16E-11	1.22e-11	21	0.879	0.88	3.1E-11	6.69E-12
22	0.827	0.827	1.1E-10	1.52e-11	22	0.787	0.787	2.94E-11	3.36E-12
23	0.861	0.86	6.17E-11	9.92e-12	23	0.892	0.89	2.4E-11	6.87E-12
24	0.779	0.78	7.05E-11	6.42e-12	24	0.785	0.789	1.09E-11	2.71E-12
25	0.832	0.834	9.94E-11	1.33e-11	25	0.839	0.836	1.18E-11	3.95E-12
26	0.865	0.867	1.03E-10	1.77e-11	26	0.841	0.841	1.56E-11	4.11E-12
27	0.832	0.827	3.37E-11	6.03e-12	27	0.868	0.862	1.41E-11	5.18E-12
28	0.861	0.861	9.32E-11	1.50e-11	28	0.855	0.852	2.1E-11	4.84E-12
31	0.882	0.885	7.52E-11	1.40e-11	31	0.816	0.815	1.11E-11	3.38E-12
32	0.869	0.868	9.03E-11	1.53e-11	32	0.835	0.833	1.13E-11	3.91E-12
33	0.838	0.838	6.35E-11	8.49e-12	33	0.807	0.805	1.04E-11	3.17E-12
34	0.851	0.851	7.76E-11	1.12e-11	34	0.805	0.805	1.25E-11	3.14E-12
35	0.818	0.817	7.17E-11	8.32e-12	35	0.862	0.862	1.21E-11	4.78E-12
36	0.852	0.849	6.78E-11	9.92e-12	36	0.865	0.864	1.12E-11	4.95E-12
37	0.868	0.869	1.26E-10	2.52e-11	37	0.882	0.882	2.96E-11	6.62E-12
41	0.403	0.4	6.32E-10	1.19e-11	41	0.374	0.373	4.02E-10	5.18E-12
42	0.242	0.242	5.79E-10	6.09e-12	42	0.28	0.273	4.29E-10	3.6E-12
43	0.189	0.18	4.94E-10	5.50e-12	43	0.217	0.21	4.18E-10	2.52E-12
					44	0.0942	0.0917	3.2E-10	2.16E-12
46	0.162	0.167	4.06E-10	5.65e-12	46	0.11	0.111	3.97E-10	1.48E-12
51	0.291	0.3	5.48E-10	7.34e-12	51	0.315	0.299	4.63E-10	4.68E-12
54	0.464	0.443	6.83E-10	1.60e-11	54	0.394	0.374	5.75E-10	9.83E-12
55	0.275	0.279	6.75E-10	7.33e-12	55	0.219	0.227	5.67E-10	5.65E-12
					56	0.17	0.176	3.12E-10	2.5E-12
57	0.582	0.58	7.75E-10	2.79e-11	57	0.638	0.655	5.65E-10	2.05E-11
58	0.726	0.695	5.42E-10	4.56e-11	58	0.748	0.773	4.91E-10	2.86E-11
59	0.829	0.827	1.02E-10	1.36e-11	59	0.83	0.828	2.23E-11	4.03E-12
60	0.69	0.689	1.12E-10	8.21e-12	60	0.616	0.616	2.11E-11	1.33E-12
61	0.763	0.723	7.53E-10	6.23e-11	61	0.781	0.783	1.37E-10	2.61E-11
62	0.797	0.795	5.22E-11	5.65e-12	62	0.82	0.822	1.65E-11	3.52E-12
63	0.813	0.812	8.54E-11	9.69e-12	63	0.821	0.819	1.52E-11	3.55E-12
64	0.826	0.825	7.81E-11	9.38e-12	64	0.857	0.857	1.52E-11	4.64E-12

65	0.853	0.852	5.48E-11	8.59e-12	65	0.776	0.776	1.26E-10	2.05E-11
66	0.875	0.874	1.05E-10	1.99e-11	66	0.754	0.758	1.43E-10	2.54E-11
67	0.843	0.842	9.61E-11	1.37e-11	67	0.838	0.836	7.48E-12	3.99E-12
68	0.801	0.8	5E-11	5.65e-12	68	0.799	0.796	1.51E-11	3.09E-12
69	0.877	0.876	1.1E-10	2.17e-11	69	0.863	0.866	1.4E-11	4.97E-12
70	0.795	0.794	6.02E-11	6.23e-12	70	0.811	0.812	1.14E-11	3.31E-12
72	0.488	0.488	6.17E-10	1.59e-11	72	0.509	0.526	4.83E-10	1.03E-11
73	0.801	0.8	4.56E-11	5.39e-12	73	0.795	0.791	1.39E-11	3.01E-12
74	0.874	0.874	6.38E-11	1.14e-11	74	0.878	0.876	1.06E-11	5.53E-12
75	0.863	0.863	7.05E-11	1.13e-11	75	0.859	0.856	1.4E-11	4.7E-12
76	0.779	0.777	5.57E-11	5.32e-12	76	0.8	0.8	2.29E-11	3.29E-12
77	0.851	0.852	6.09E-11	9.14e-12	77	0.902	0.9	1.46E-11	7.11E-12
78	0.795	0.793	4.46E-11	5.09e-12	78	0.8	0.802	6.04E-12	3.01E-12
79	0.784	0.781	6.98E-11	6.59e-12	79	0.828	0.828	1.85E-11	3.78E-12
80	0.828	0.829	7.23E-11	8.96e-12	80	0.823	0.819	2.55E-11	4E-12
81	0.862	0.861	9.33E-11	1.52e-11	81	0.871	0.872	1.18E-11	5.21E-12
82	0.847	0.848	8.08E-11	1.14e-11	82	0.874	0.873	2.73E-11	6.04E-12
83	0.781	0.781	5.05E-11	5.03e-12	83	0.751	0.751	1.61E-11	2.33E-12
84	0.805	0.804	6.09E-11	6.59e-12	84	0.761	0.761	1.51E-11	2.47E-12
85	0.736	0.735	4.64E-11	3.78e-12	85	0.71	0.704	1.94E-11	1.94E-12
87	0.831	0.83	8.49E-11	1.08e-11	87	0.992	0.971	4.31E-10	9.55E-10
91	0.828	0.828	8.37E-11	1.03e-11	91	0.864	0.867	1.29E-11	4.81E-12
92	0.821	0.823	6.72E-11	7.90e-12	92	0.815	0.815	9.99E-12	3.34E-12
93	0.822	0.823	7.16E-11	8.42e-12	93	0.876	0.875	1.77E-11	5.53E-12
94	0.827	0.827	5.76E-11	7.35e-12	94	0.838	0.837	2.2E-11	4.23E-12
95	0.86	0.86	8.7E-11	1.36e-11	95	0.851	0.85	2.53E-11	4.85E-12
96	0.879	0.878	6.56E-11	1.20e-11	96	0.833	0.832	1.19E-11	3.83E-12
97	0.857	0.857	6.5E-11	9.95e-12	97	0.83	0.832	1.25E-11	3.7E-12
98	0.855	0.852	8.3E-11	1.23e-11	98	0.838	0.838	1.34E-11	3.99E-12
99	0.821	0.822	7.38E-11	8.59e-12	99	0.84	0.837	1.65E-11	4.06E-12
100	0.848	0.847	7.21E-11	1.01e-11	100	0.837	0.834	1.61E-11	3.98E-12
101	0.859	0.856	8.42E-11	1.31e-11	101	0.869	0.864	1.93E-11	5.34E-12
102	0.871	0.873	1.28E-10	2.64e-11	102	0.762	0.764	1.3E-10	2.09E-11
103	0.831	0.828	6.21E-11	7.99e-12	103	0.805	0.806	1.76E-11	3.27E-12
104	0.799	0.799	7.47E-11	7.68e-12	104	0.834	0.832	3.23E-11	4.65E-12
105	0.751	0.753	5.26E-11	4.46e-12	105	0.824	0.82	4.47E-11	5.47E-12
106	0.726	0.728	7.84E-11	5.66e-12	106	0.727	0.727	1.54E-10	2.64E-11
107	0.829	0.789	9.67E-11	1.26e-11	107	0.739	0.743	1.53E-10	2.77E-11
108	0.816	0.812	7.37E-11	8.38e-12	108	0.838	0.838	3.34E-11	4.87E-12
109	0.798	0.798	7.51E-11	7.62e-12	109	0.848	0.848	4.7E-11	6.57E-12
111	0.913	0.913	1.25E-10	3.88e-11	111	0.885	0.881	2.48E-11	6.6E-12
112	0.889	0.872	1.45E-10	4.04e-11	112	0.859	0.859	2.36E-11	5.12E-12
113	0.904	0.904	2.14E-10	1.26e-10	113	0.862	0.864	1.9E-11	5.08E-12
114	0.788	0.753	1.82E-10	3.63e-11	114	0.791	0.794	2.49E-11	3.25E-12
116	0.894	0.895	9.79E-11	2.13e-11	116	0.876	0.872	1.97E-11	5.74E-12
117	0.87	0.84	9.07E-11	1.57e-11	117	0.882	0.877	1.23E-11	5.81E-12
118	0.85	0.805	9.7E-11	1.46e-11	118	0.822	0.824	4.03E-11	4.95E-12
119	0.809	0.807	1.09E-10	1.33e-11	119	0.79	0.782	1.94E-11	3.05E-12
120	0.87	0.868	6.3E-11	1.09e-11	120	0.84	0.839	1.46E-11	4.08E-12
121	0.856	0.856	5.08E-11	8.40e-12	121	0.855	0.854	1.11E-11	4.54E-12
122	0.86	0.86	6.49E-11	1.02e-11	122	0.838	0.837	1.05E-11	3.96E-12
123	0.834	0.83	5.94E-11	7.91e-12	123	0.831	0.829	1.4E-11	3.8E-12
124	0.677	0.648	7.11E-10	3.91e-11	124	0.755	0.71	2.55E-11	2.7E-12

Table S2.2B S^2 and τ_e values of PLAAT4 obtained from the model free fit of the relaxation parameters of individual residues obtained at 600 MHz and 850 MHz. M2 and TM2 corresponds to isotropic and anisotropic model free calculations using model 2.

PLAAT4									
600 MHz					850 MHz				
Res	S^2 (M2)	S^2 (TM2)	τ_e (M2)	Error	Res	S^2 (M2)	S^2 (TM2)	τ_e (M2)	Error
7	0.508	0.524	7.23E-10	1.28e-11	7	0.463	0.476	6.18E-10	1.06e-11
9	0.91	0.916	4.24E-10	1.15e-10					-
11	0.906	0.905	7.65E-11	1.60e-11	11	0.932	0.932	2.16E-11	8.26e-12
12	0.914	0.881	4.54E-10	1.25e-10	12	0.943	0.942	6.02E-10	1.10e-10
13	0.946	0.946	9.6E-11	3.74e-11	13	0.953	0.951	2.99E-11	1.38e-11
14	0.926	0.925	1.17E-10	3.71e-11	14	0.946	0.945	1.69E-11	9.76e-12
15	0.954	0.953	2.4E-10	2.38e-10	15	0.978	0.977	5.11E-11	4.52e-11
17	0.946	0.945	2.2E-10	1.77e-10	17	0.984	0.984	9.68E-12	3.34e-11
18	0.903	0.902	9.8E-11	2.12e-11	18	0.833	0.834	2.42E-11	3.15e-12
				-	19	0.865	0.876	6.02E-10	4.53e-11
21	0.944	0.933	2.8E-10	2.21e-10					-
22	0.949	0.949	2.31E-10	2.04e-10					-
23	0.933	0.922	2.72E-10	1.79e-10	23	0.97	0.97	1.26E-10	1.30e-10
25	0.938	0.937	1E-10	3.47e-11	25	0.932	0.931	1.12E-11	7.31e-12
26	0.912	0.911	8.48E-11	1.93e-11	26	0.93	0.929	2.02E-11	7.72e-12
27	0.934	0.948	5.48E-10	1.58e-10	27	0.983	0.982	2.88E-10	3.15e-10
28	0.796	0.807	4.84E-10	4.31e-11	28	0.83	0.843	4.26E-10	2.64e-11
32	0.938	0.939	1.66E-10	8.46e-11	32	0.983	0.984	6.98E-11	8.50e-11
33	0.913	0.912	7.87E-11	1.79e-11	33	0.923	0.922	2.54E-11	7.64e-12
34	0.927	0.926	8.87E-11	2.49e-11	34	0.939	0.938	3.8E-11	1.22e-11
35	0.941	0.935	3.33E-10	2.01e-10	35	0.977	0.976	4.19E-10	2.28e-10
44	0.271	0.262	6.99E-10	4.32e-12					
45	0.234	0.231	7.07E-10	3.59e-12	45	0.241	0.232	5.9E-10	5.82e-12
53	0.159	0.158	4.23E-10	4.45e-12	53	0.176	0.174	3.81E-10	1.34e-12
54	0.925	0.925	2.07E-10	1.14e-10	54	0.963	0.963	1.35E-10	1.15e-10
61	0.913	0.918	5.21E-10	1.22e-10	61	0.963	0.963	4.6E-10	1.44e-10
62	0.9	0.9	8.39E-11	1.67e-11	62	0.886	0.886	2.29E-11	4.75e-12
63	0.925	0.925	1.07E-10	3.18e-11	63	0.993	0.993	1.35E-10	6.02e-10
64	0.893	0.889	8.51E-11	1.57e-11	64	0.905	0.902	2.62E-11	6.10e-12
65	0.935	0.933	1.91E-10	1.12e-10	65	0.931	0.931	2.66E-11	8.72e-12
66	0.93	0.9	2.63E-10	1.66e-10					-
67	0.939	0.938	1.57E-10	7.70e-11	67	0.97	0.969	6.2E-11	4.16e-11
68	0.894	0.895	6.75E-11	1.22e-11	68	0.938	0.937	2.92E-11	1.02e-11
69	0.931	0.93	2.23E-10	1.42e-10					-
70	0.929	0.929	2.34E-10	1.49e-10					-
72	0.904	0.921	4.43E-10	1.08e-10	72	0.932	0.942	3.34E-10	7.32e-11
73	0.907	0.905	1.01E-10	2.31e-11	73	0.964	0.963	9.87E-11	6.97e-11
75	0.94	0.938	2.23E-10	1.63e-10	75	0.979	0.964	1.36E-10	2.01e-10
76	0.889	0.888	9.12E-11	1.67e-11	76	0.891	0.891	2.63E-11	5.36e-12
77	0.94	0.94	2.64E-10	1.96e-10	77	0.967	0.982	4.78E-10	1.65e-10
78	0.869	0.869	5.39E-11	8.04e-12	78	0.851	0.851	1.41E-11	3.11e-12
80	0.699	0.723	5.52E-10	2.62e-11	80	0.722	0.74	5.29E-10	1.79e-11
81	0.81	0.817	5.83E-10	4.91e-11	81	0.86	0.866	5.58E-10	4.02e-11
83	0.904	0.902	1.28E-10	3.33e-11	83	0.937	0.936	8.31E-11	3.00e-11
84	0.917	0.917	1.78E-10	7.56e-11	84	0.973	0.96	1.4E-10	1.65e-10

85	0.867	0.866	7.86E-11	1.14e-11	85	0.893	0.893	4.93E-11	8.77e-12
87	0.91	0.91	1.52E-10	4.93e-11	87	0.934	0.933	5.42E-11	1.58e-11
89	0.933	0.934	1.9E-10	1.06e-10	89	0.959	0.946	3.2E-10	1.23e-10
90	0.932	0.933	1.51E-10	6.37e-11	90	0.978	0.972	1.81E-10	2.61e-10
91	0.947	0.932	2.14E-10	1.74e-10	91	0.972	0.969	7.69E-11	5.92e-11
92	0.208	0.206	9.78E-12	2.14e-13	92	0.743	0.737	2.88E-11	2.12e-12
93	0.919	0.922	1.7E-10	6.95e-11	93	0.95	0.95	3.7E-11	1.47e-11
94	0.906	0.902	1.11E-10	2.65e-11	94	0.956	0.955	6.43E-11	2.96e-11
97	0.887	0.89	1.36E-10	3.15e-11	97	0.916	0.916	3.38E-11	8.00e-12
98	0.926	0.925	8.46E-11	2.31e-11	98	0.952	0.951	3.93E-11	1.61e-11
99	0.902	0.901	8.83E-11	1.82e-11	99	0.897	0.896	2.46E-11	5.48e-12
100	0.942	0.94	1.47E-10	7.05e-11	100	0.972	0.969	5.64E-11	3.98e-11
101	0.935	0.948	4.66E-10	1.62e-10	101	0.958	0.959	4.62E-11	2.18e-11
103	0.874	0.873	9.92E-11	1.65e-11	103	0.9	0.899	4.93E-11	9.34e-12
104	0.921	0.92	2.11E-10	1.13e-10					-
105	0.891	0.891	1.92E-10	6.75e-11	105	0.952	0.95	1.39E-10	9.35e-11
111	0.515	0.501	6.22E-10	1.15e-11	111	0.599	0.59	5.14E-10	1.04e-11
112	0.414	0.409	7.06E-10	8.53e-12	112	0.425	0.416	5.73E-10	7.84e-12
115	0.943	0.94	2.41E-10	1.93e-10					-
116	0.864	0.882	6.14E-10	7.17e-11	116	0.897	0.906	5.01E-10	5.07e-11
118	0.956	0.956	2.16E-10	2.09e-10					-
119	0.797	0.786	5.5E-10	4.37e-11	119	0.85	0.843	4.9E-10	3.32e-11
120	0.931	0.931	1.32E-10	4.82e-11	120	0.957	0.957	3.46E-11	1.64e-11
121	0.945	0.945	1.64E-10	9.35e-11	121	0.981	0.98	7.51E-11	8.33e-11
122	0.929	0.929	6.56E-11	1.83e-11					-
123	0.922	0.921	1.61E-10	6.52e-11					-

Table S2.3 Exchange parameters for millisecond dynamics of amide ^{15}N nuclei in PLAAT3 and PLAAT4, assuming a two-state exchange.

PLAAT3				PLAAT4			
Residue	k_{ex} (10^3 s^{-1})	pB (%)	$ \Delta\omega $ (ppm)	Residues	k_{ex} (10^3 s^{-1})	pB (%)	$ \Delta\omega $ (ppm)
Global Fit (W24, V50, M51, D56, D81)	1.2(0.3)	n.d	n.d	Dynamic Cluster (R18, L19, Y21, H23, K61, H35)	1.9(0.2)	1.0(0.1)	R18: 2.3(0.3) L19: 1.2(0.1) Y21: 2.6(0.3) H23: 2.0(0.2) H35: 1.2(0.1) K61: 1.3(0.2)

PLA/AT-3

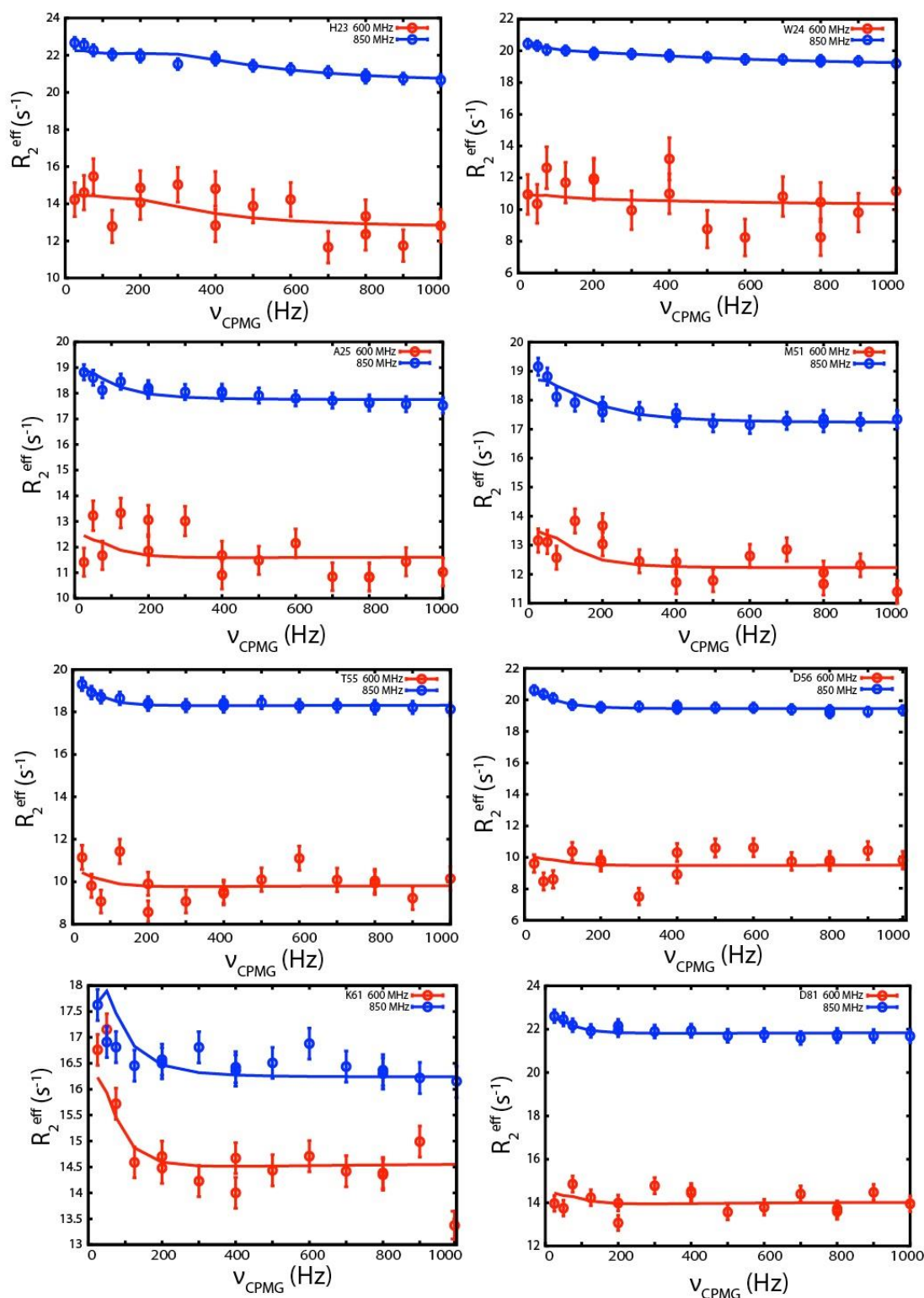
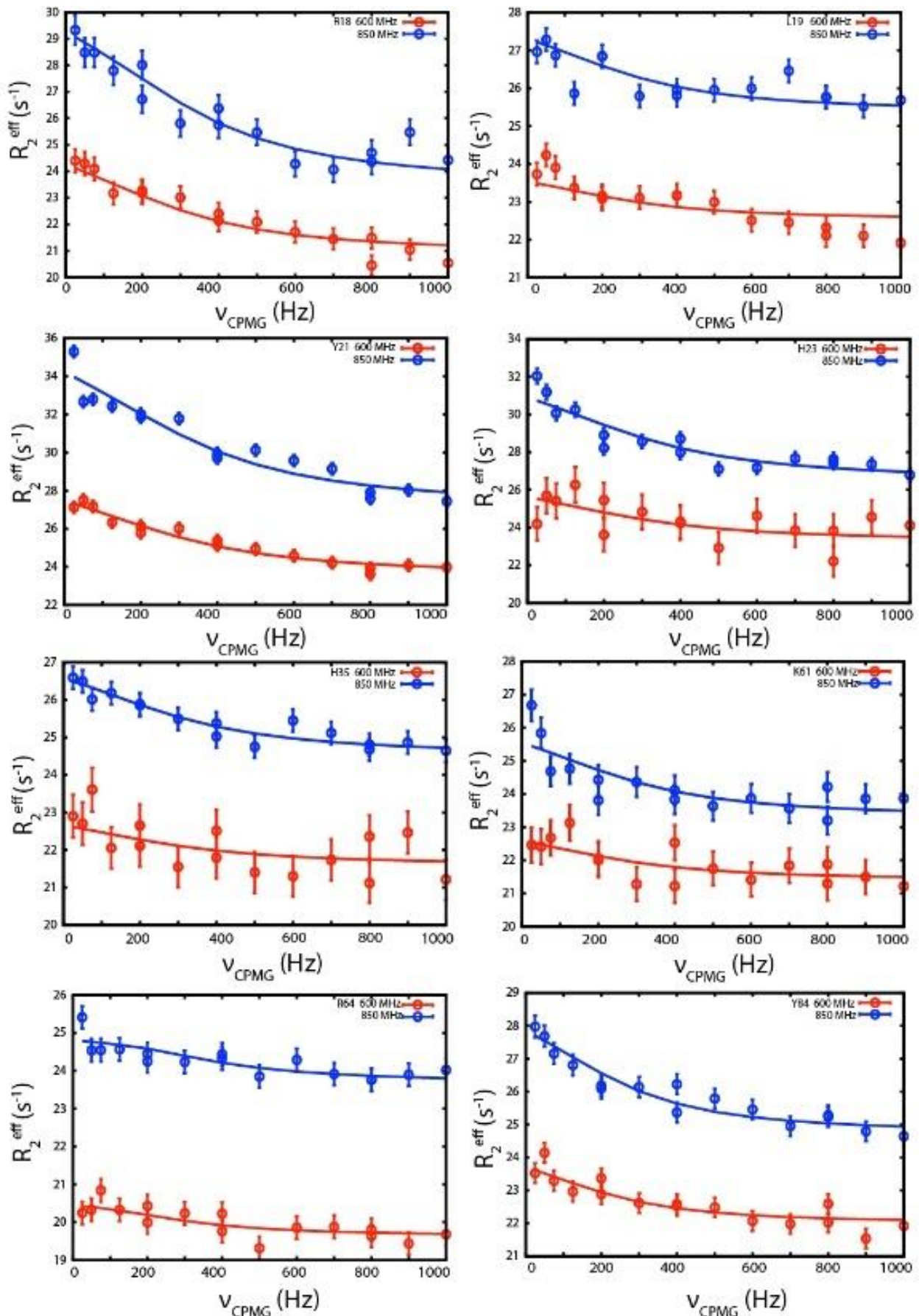


Figure S2.1 Relaxation dispersion curves for PLA/AT-3. The effective transverse relaxation rates are plotted against the CPMG frequency for the indicated residues. The red and blue curves represent data acquired at 14 T and 20 T, respectively. The experimental data are indicated by circles. The solid lines indicate fits of the combined two-field data to a two-state exchange model.

PLA/AT-4



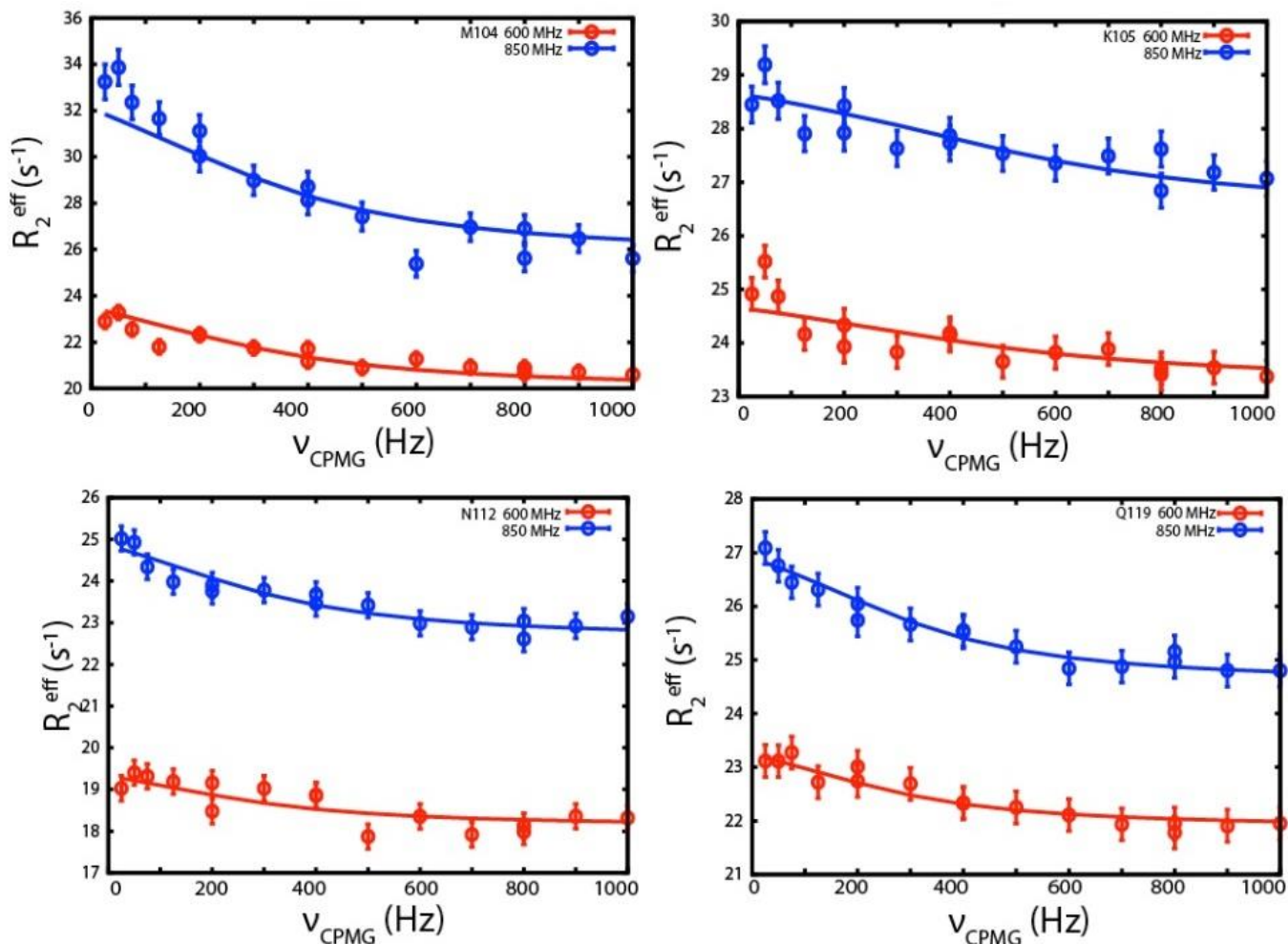


Figure S2.2 Relaxation dispersion curves for PLAAT4. The effective transverse relaxation rates are plotted against the CPMG frequency for the indicated residues. The red and blue curves represent data acquired at 14 T and 20 T, respectively. The experimental data are indicated by circles. The solid lines indicate fits of the combined two-field data to a two-state exchange model.

References

- (1) Golczak, M., Kiser, P. D., Sears, A. E., Lodowski, D. T., Blaner, W. S., and Palczewski, K. (2012) Structural basis for the acyltransferase activity of lecithin:retinol acyltransferase-like proteins. *J. Biol. Chem.* 287, 23790–23807.
- (2) Anantharaman, V., and Aravind, L. (2003) Evolutionary history, structural features and biochemical diversity of the NlpC/P60 superfamily of enzymes. *Genome Biol.* 4, R11–R11.
- (3) Hajnal, A., Klemen, R., and Schäfer, R. (1994) Subtraction cloning of H-rev107, a gene specifically expressed in H-ras resistant fibroblasts. *Oncogene* 9, 479–490.
- (4) Akiyama, H., Hiraki, Y., Noda, M., Shigeno, C., Ito, H., and Nakamura, T. (1999) Molecular cloning and biological activity of a novel Ha-Ras suppressor gene predominantly expressed in skeletal muscle, heart, brain, and bone marrow by differential display using clonal mouse EC cells, ATDC5. *J. Biol. Chem.* 274, 32192–32197.
- (5) Shyu, R.-Y., Hsieh, Y.-C., Tsai, F.-M., Wu, C.-C., and Jiang, S.-Y. (2008) Cloning and functional characterization of the HRASLS2 gene. *Amino Acids* 35, 129–137.
- (6) Uyama, T., Ikematsu, N., Inoue, M., Shinohara, N., Jin, X.-H., Tsuboi, K., Tonai, T., Tokumura, A., and Ueda, N. (2012) Generation of N-acylphosphatidylethanolamine by members of the phospholipase A/acyltransferase (PLA/AT) family. *J. Biol. Chem.* 287, 31905–31919.
- (7) Jin, X.-H., Uyama, T., Wang, J., Okamoto, Y., Tonai, T., and Ueda, N. (2009) cDNA cloning and characterization of human and mouse Ca²⁺-independent phosphatidylethanolamine N-acyltransferases. *Biochim. Biophys. Acta - Mol. Cell Biol. Lipids* 1791, 32–38.
- (8) Husmann, K., Sers, C., Fietze, E., Mincheva, A., Lichter, P., and Schäfer, R. (1998) Transcriptional and translational downregulation of H-REV107, a class II tumour suppressor gene located on human chromosome 11q11-12. *Oncogene* 17, 1305.
- (9) Ueda, N., Tsuboi, K., and Uyama, T. (2010) N-acylethanolamine metabolism with special reference to N-acylethanolamine-hydrolyzing acid amidase (NAAA). *Prog. Lipid Res.* 49, 299–315.
- (10) Ara, I., Rahman, S., Tsuboi, K., Uyama, T., and Ueda, N. (2014) New players in the fatty acyl ethanolamide metabolism OH OH OH. *Pharmacol. Res.* 86, 1–10.
- (11) Ren, X., Lin, J., Jin, C., and Xia, B. (2010) Solution structure of the N-terminal catalytic domain of human H-REV107--a novel circularly permuted NlpC/P60 domain. *FEBS Lett.* 584, 4222–4226.
- (12) Wei, H., Wang, L., Ren, X., Yu, W., Lin, J., Jin, C., and Xia, B. (2015) Structural and functional characterization of tumor suppressors TIG3 and H-REV107. *FEBS Lett.* 589, 1179–1186.
- (13) Uyama, T., Jin, X.-H., Tsuboi, K., Tonai, T., and Ueda, N. (2009) Characterization of the

- human tumor suppressors TIG3 and HRASLS2 as phospholipid-metabolizing enzymes. *Biochim. Biophys. Acta - Mol. Cell Biol. Lipids* 1791, 1114–1124.
- (14) Pang, X.-Y., Cao, J., Addington, L., Lovell, S., Battaile, K. P., Zhang, N., Rao, J. L. U. M., Dennis, E. A., and Moise, A. R. (2012) Structure/function relationships of adipose phospholipase A2 containing a Cys-His-His catalytic triad. *J. Biol. Chem.* 287, 35260–35274.
- (15) Ren, X., Lin, J., Jin, C., and Xia, B. (2010) ¹H, ¹³C and ¹⁵N resonance assignments of human H-REV107 N-terminal domain. *Biomol. NMR Assign.* 4, 175–178.
- (16) Wang, L., Yu, W., Ren, X., Lin, J., Jin, C., and Xia, B. (2012) ¹H, ¹³C, and ¹⁵N resonance assignments of the N-terminal domain of human TIG3. *Biomol. NMR Assign.* 6, 201–203.
- (17) de la Torre, J., Huertas, M. L., Carrasco, B., García de la Torre, J., Huertas, M. L., and Carrasco, B. (2000) HYDRONMR: prediction of NMR relaxation of globular proteins from atomic-level structures and hydrodynamic calculations. *J. Magn. Reson.* 147, 138–146.
- (18) Lipari, G., and Szabo, A. (1982) Model-free approach to the interpretation of nuclear magnetic resonance relaxation in macromolecules. 1. Theory and range of validity. *J. Am. Chem. Soc.* 104, 4546–4559.
- (19) Lipari, G., and Szabo, A. (1982) Model-free approach to the interpretation of nuclear magnetic resonance relaxation in macromolecules. 2. Analysis of experimental results. *J. Am. Chem. Soc.* 104, 4559–4570.
- (20) Golczak, M., Sears, A. E., Kiser, P. D., and Palczewski, K. (2015) LRAT-specific domain facilitates Vitamin A metabolism by domain swapping in HRASLS3. *Nat. Chem. Biol.* 11, 26–32.
- (21) Palmer, A. (2013) Protein dynamics from NMR spectroscopy and MD simulation. *Biophys. J.* 104, 45a.
- (22) Krepl, M., Cléry, A., Blatter, M., Allain, F. H. T., and Sponer, J. (2016) Synergy between NMR measurements and MD simulations of protein/RNA complexes: application to the RRM, the most common RNA recognition motifs. *Nucleic Acids Res.* 44, 6452–6470.
- (23) Trbovic, N., Kim, B., Friesner, R. A., and Palmer 3rd, A. G. (2008) Structural analysis of protein dynamics by MD simulations and NMR spin-relaxation. *Proteins* 71, 684–694.
- (24) Zhang, L., Bouguet-Bonnet, S., and Buck, M. (2012) Combining NMR and molecular dynamics studies for insights into the allostery of small GTPase-protein interactions. *Methods Mol. Biol.* 796, 235–259.
- (25) Jiang, B., Yu, B., Zhang, X., Liu, M., and Yang, D. (2015) A ¹⁵N CPMG relaxation dispersion experiment more resistant to resonance offset and pulse imperfection. *J. Magn. Reson.* 257, 1–7.
- (26) Clore, G. M., Szabo, A., Bax, A., Kay, L. E., Driscoll, P. C., and Gronenborn, A. M. (1990) Deviations from the simple two-parameter model-free approach to the interpretation of nitrogen-15

nuclear magnetic relaxation of proteins. *J. Am. Chem. Soc.* 112, 4989–4991.

(27) Orekhov, V. Y., Korzhnev, D. M., Diercks, T., Kessler, H., and Arseniev, A. S. (1999) ^1H - ^{15}N NMR dynamic study of an isolated α -helical peptide (1–36)- bacteriorhodopsin reveals the equilibrium helix-coil transitions. *J. Biomol. NMR* 14, 345–356.

(28) Fushman, D., Cahill, S., and Cowburn, D. (1997) The main-chain dynamics of the dynamin pleckstrin homology (PH) domain in solution: analysis of ^{15}N relaxation with monomer/dimer equilibration. Edited by P.E. Wright. *J. Mol. Biol.* 266, 173–194.

(29) Korzhnev, D. M., Billeter, M., Arseniev, A. S., and Orekhov, V. Y. (2001) NMR studies of Brownian tumbling and internal motions in proteins. *Prog. Nucl. Magn. Reson. Spectrosc.* 38, 197–266.

(30) Mandel, A. M., Akke, M., and Palmer Arthur G., I. I. I. (1995) Backbone dynamics of *Escherichia coli* ribonuclease HI: correlations with structure and function in an active enzyme. *J. Mol. Biol.* 246, 144–163.

(31) Altschul, S. F., Madden, T. L., Schäffer, A. A., Zhang, J., Zhang, Z., Miller, W., and Lipman, D. J. (1997) Gapped BLAST and PSI-BLAST: a new generation of protein database search programs. *Nucleic Acids Res.* 25, 3389–3402.

3

Chapter

Molecular dynamics simulations reveal loop rearrangements in PLAAT4.

This chapter is based on joint work with Rubin Dasgupta

The work in this chapter was published as: Chatterjee, S. D., Zhou, J., Dasgupta, R., Cramer-Blok, A., Timmer, M., van der Stelt, M., and Ubbink, M. (2021) Protein Dynamics Influence the Enzymatic Activity of Phospholipase A/Acyltransferases 3 and 4. *Biochemistry* 60, 1178–1190.

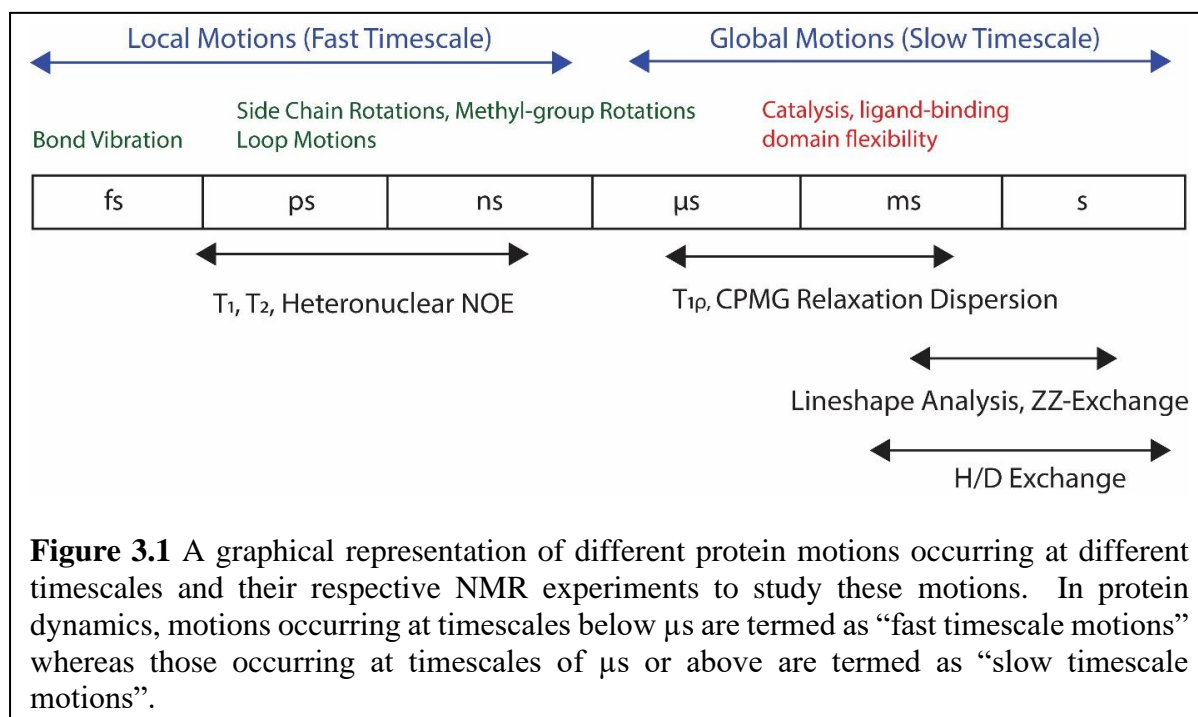
Abstract

Molecular dynamics simulations are becoming increasingly commonplace to complement findings from NMR spectroscopy to study protein dynamics. In this study, we took a closer look at the dynamics of PLAAT3 and PLAAT4 to complement the knowledge obtained from NMR dynamics experiments. MD simulations support our earlier findings that PLAAT4 is inherently more flexible than PLAAT3. The active site of PLAAT4 is more mobile, in line with the observation that the resonances of many nuclei are missing in the ^{15}N - ^1H HSQC spectrum due to exchange effects. An instability of the catalytic triad followed by a conformational rearrangement of L2(B6) in PLAAT4 was observed. The increased dynamics of this loop may relate to the higher activity of PLAAT4.

Introduction

To understand structure-function relationships of proteins, not only the ground state structures but also their dynamic properties need to be studied.^{1,2} Protein dynamics occur at many timescales (Figure 3.1) and are linked to specific events such as bond vibrations (femtosecond timescale), side-chain rotations and loop motions (pico-nanosecond timescale) and biologically crucial processes such as folding, ligand binding and catalysis (micro-millisecond timescale).³ Various spectroscopic techniques, including NMR spectroscopy and computational approaches such as molecular dynamics (MD) simulations, are used to study such motions to provide insight into the function of proteins. While NMR spectroscopy is an experimental technique that allows us to study fast (ns-ps) and slow motions (μs -ms) of a protein, it does not provide us with direct structural insights. MD simulations are used to study regions of protein, such as loops, that are flexible on a faster timescale and the technique provide us with direct structural insights. These loop regions can be crucial in protein-protein and protein-ligand interactions.^{4,5} MD simulations are therefore often used to complement the findings from fast-timescale dynamics experiments (T_1 , T_2 and cross relaxation parameters). NMR derived parameters, such as order parameters,^{6,7} heteronuclear NOEs⁸ and residual dipolar couplings⁹ can be back-

calculated from MD simulations and compared with the experimental data to establish whether the simulation offers a good model for the true dynamics in a protein.



MD simulations of proteins started to be used in the early 1980s.¹⁰ Since then the technique has gained power enormously with the growth of computation power and parallelization techniques. The high-resolution information about exact position of an atom at any given time in the trajectory is one of the best features of this technique. However, the two major limitations of this technique are the length of the conformational sampling time and quality of the force-fields.¹¹

In MD simulations, Newtonian equations of motions are solved for atoms taking into account interatomic forces. The parameters used to describe the forces between atoms are derived from various experimental and quantum mechanical calculations. Force fields take into account parameters for bond length, bond angles, torsion angles, van der Waals and electrostatic interactions.^{12–15} Three things are essential for simulations, a starting structure (usually a pdb file), a force field, and a solvation model. A starting structure provides the atomic coordinates that can be obtained from experimental structures or homology models. The potential energy of the system in simulation is obtained from the force field, a parameterization of the energy surface of the protein. There are many different force field models and the most commonly used are the CHARMM,¹⁶ AMBER,^{17–19} and GROMOS^{20,21} force fields. Frequently used

simulation software packages are CHARMM,²² AMBER,¹⁴ GROMACS,²³ and NAMD.¹² These packages share common capabilities and features but vary in their capacities, and underlying philosophies. The third important aspect of MD simulation is the choice of the solvent model, since the purpose for the simulation is to study protein motions under experimental conditions. The protein molecule is solvated using either of the two water models—the implicit or explicit solvent models. Implicit solvent does not take into account the movement of solvent molecules but rather averages the solvent conformations over its degrees of freedom.²⁴ The explicit solvent models allow the solvent molecules to be defined with a possibility of neutralising the system by adding counterions inside a solvent box. Various explicit solvent models exist such as TIP3P, TIP4P, TIP5P, SPC.^{25–27}

A typical MD simulation starts with the energy minimization of the starting structure, followed by explicit solvation, the equilibration step and the final production step. In the equilibration step, the solvent molecules that were defined in case of explicit solvent models are allowed to move (equilibrate) by raising the temperature in small steps while protein positions are fixed. Equilibration steps are done under constant temperature and constant pressure conditions. In the production step the positional constraints on the protein are removed to let the protein and solvent to relax.

The trajectories are analysed to extract from the large data sets the information that is relevant for model building and comparison with experimental data. With modern processing units (CPUs, GPUs and supercomputing nodes) and efficient algorithms, large proteins or protein complexes can be simulated for 100s of ns and even μ s. Analysis of the trajectories can be classified into four types: 1) Checking the integrity of the simulation and global analysis of the protein, including calculation of the root-mean-square deviation (RMSD) over time, the total energy of the system, the radius of gyration and the temperature and pressure fluctuations, 2) Cluster analysis by grouping the RMSD into separate conformational groups by k-means clustering or hierarchical approach,^{28–30} 3) Principal component analysis to extract the correlated protein motions, also known as essential dynamics from sampled conformations,^{31–34} and 4) Correlation function analysis of the bond-vectors to derive order parameters or atomic fluctuations to evaluate concerted motions in different parts of the protein.^{35–37}

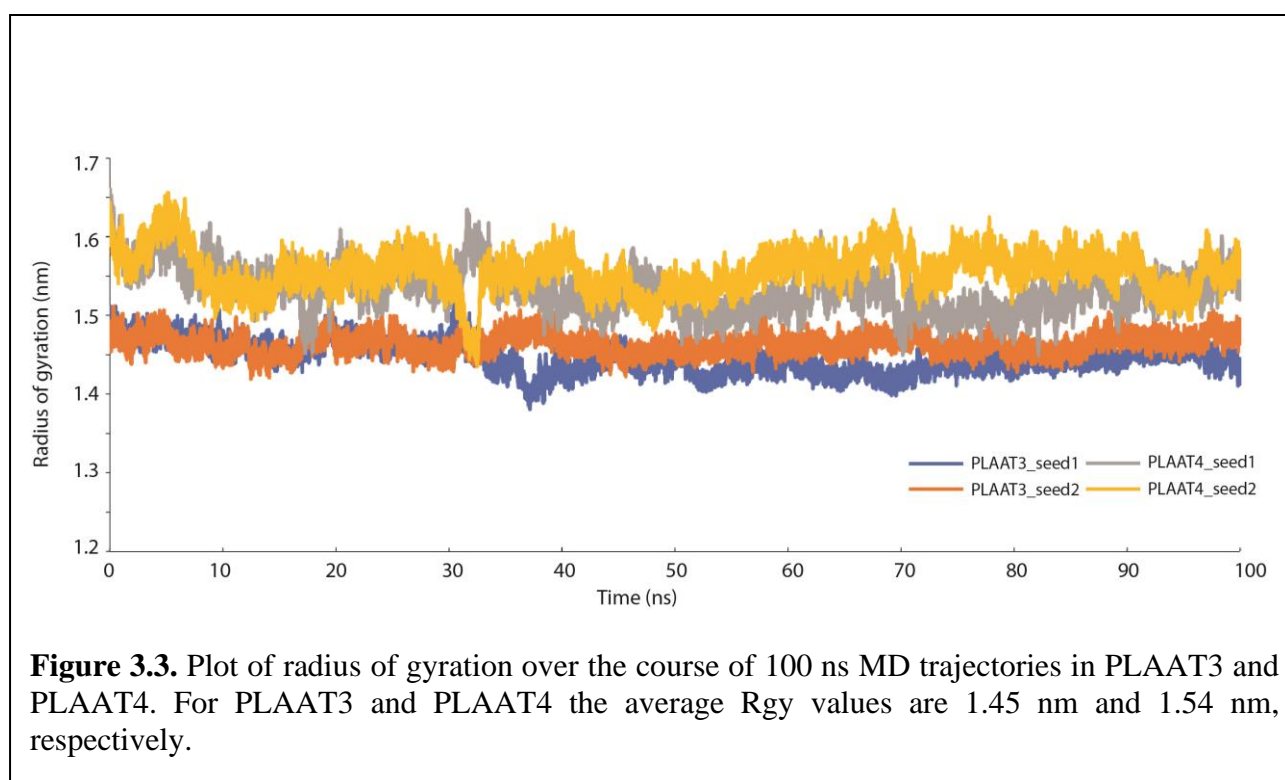
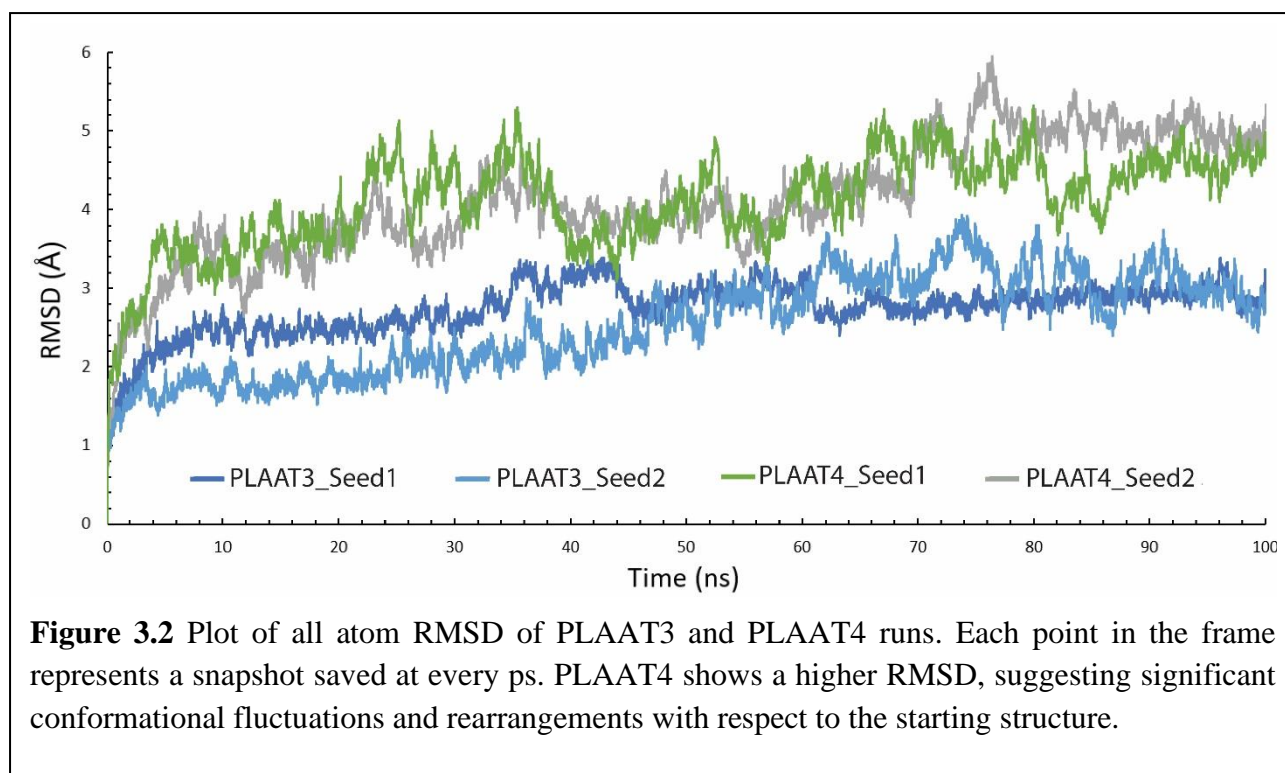
To complement the findings obtained from NMR dynamics studies of PLAAT3 and PLAAT4 (Chapter 2), we used MD simulations to study the internal motions of PLAAT3 and PLAAT4 to gain insights into the dynamics of the two proteins. In Chapter 2, we found contrasting

dynamics profile between the two proteins, especially for the flexible loop L1, residues around the active site and residues with nuclei missing resonance assignments in the NMR spectra, suggesting flexibility. Since the two proteins differ in phospholipase activity, MD simulations were performed to visualise protein dynamics to aid in our understanding of the two proteins. The results indicate significant differences between PLAAT3 and PLAAT4 active site dynamics, strengthening the findings from NMR experiments.

Results

Classical all-atom MD simulations on proteins were performed using NMR structures solvated in a rectangular water box, neutralized by counter ions and using the AMBER ff99sb-ILDN force-field. We used the GROMACS package, as it is open source, supports parallelization and GPU acceleration for faster non-bonded atomic calculations and possesses a large number of external tools for trajectory analysis.³⁸ Two runs of 100 ns were performed with different starting velocities for both PLAAT3 and PLAAT4.

Structural stability. The root mean-square deviation (RMSD) is an indicator of the global conformational stability of a structure during the simulation. Figure 3.2 presents the RMSD of the structural snapshots as compared to the starting structure over the course of the simulation. An initial jump in RMSD is normally observed within the first picosecond, which occurs due to the inherent fluctuation of atomic coordinates of the starting model as the spatial restrictions on the model are lifted. In the first 10 ns, the RMSD steadily increases as the protein samples different conformations. The RMSD value stabilizes after about 10 ns, with relatively minor fluctuations in the conformation. The larger RMSD observed for PLAAT4 indicates that considerable structural fluctuations are taking place over the course of the simulations. For example, in run 2 (seed 2), toward 70 ns, the RMSD increases further, suggesting that the protein undergoes a significant conformational rearrangement relative to the starting structure. In PLAAT3, the structure appears to remain relatively stable after the initial relaxation, suggesting that no significant structural fluctuations occur over the 100 ns period. The radii of gyration were also determined. They fluctuated around a value that remained stable during the MD simulations, with average values of 1.45 and 1.54 nm for PLAAT3 and PLAAT4, respectively (Figure 3.3).



Essential dynamics. To observe and analyse important concerted motions (often known as essential dynamics), principal component analysis was performed. RMS fluctuations were calculated for all residues globally (Figure S3.1) and also for the top two eigenvectors (the two most significant principal components) to study essential dynamics (Figure 3.4). Residues with the highest RMS fluctuations of any atom above 2 Å were analysed and plotted on the NMR structures (Figure 3.5). In the course of the 100 ns simulations, it was observed that PLAAT3 maintains largely a rigid conformation, especially an ordered secondary structure. Apart from the disordered loop L1 (residues 43-55), only residues 19-22, along with 83-84 and the C-terminal residues 124-125 showed concerted flexibility. The distances between the active site atoms C113S_γ and H23N_δ and between H23N_ε and H35N_δ all remained below 5 Å (Figure S3.2), indicating that the active site triad (see Chapter 2, Figure 2.1.) remained intact.

In PLAAT4, more concerted motions were observed (Figure 3.4B). More residues in the flexible loop L1 (40-56), as well as residues 82-86, 88, 90, L2(B6) (108-111) and the N and C termini residues showed fluctuations above 2 Å, suggesting that these parts have correlated motions. In the active site of PLAAT4, C113S_γ exhibited an RMS fluctuation of 2.3 Å, while its backbone atoms were more rigid. This side-chain fluctuation came about as part of a significant rearrangement that took place in L2(B6). Since the α-helix A3, of which C113 is a part, is connected to this loop, its rearrangement rendered the active site quite mobile. The interaction between the cysteine of the catalytic triad and the histidine rings was disrupted during each of the two runs. Movements of the nucleophile residue C113S_γ and the base H23N_δ/N_ε and a concerted set of molecular rearrangements in the loop L2(B6) brought R111N_ε in close proximity of C113S_γ (Figure 3.6, panels A and B). The arginine side-chain was stabilized by the formation of two salt bridges with E114O_ε and E22O_ε. The interaction with the E114 was stable over almost the entire run. The distance between the side-chains of E22 and R111 showed some correlation with that between C113 and R111 (Figure 3.6, panels C and D). The interconversion between the active site in the native and disrupted active site states appears to happen fast and, thus, can be described by a two-state model, illustrated in Figure 3.7.

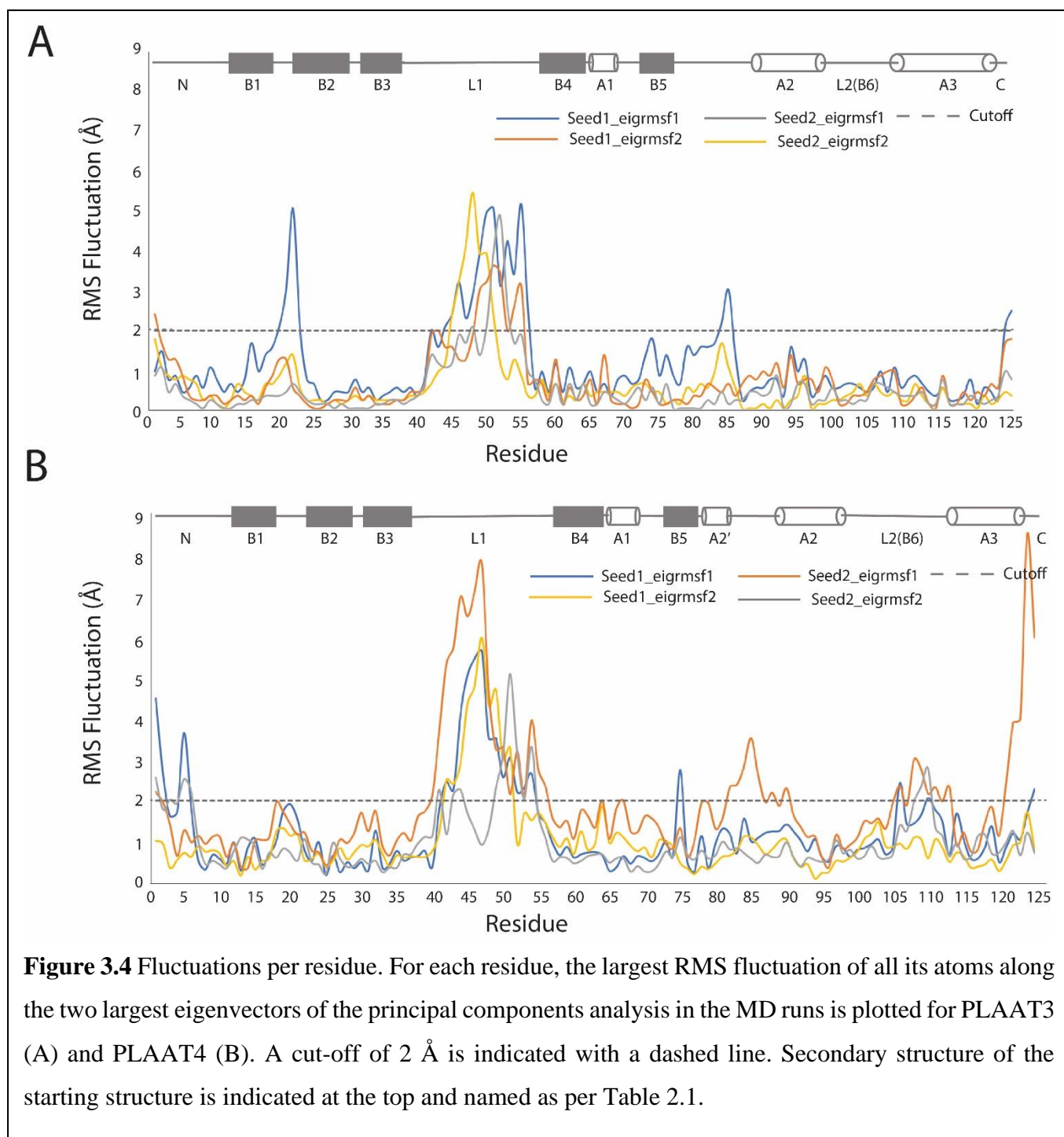
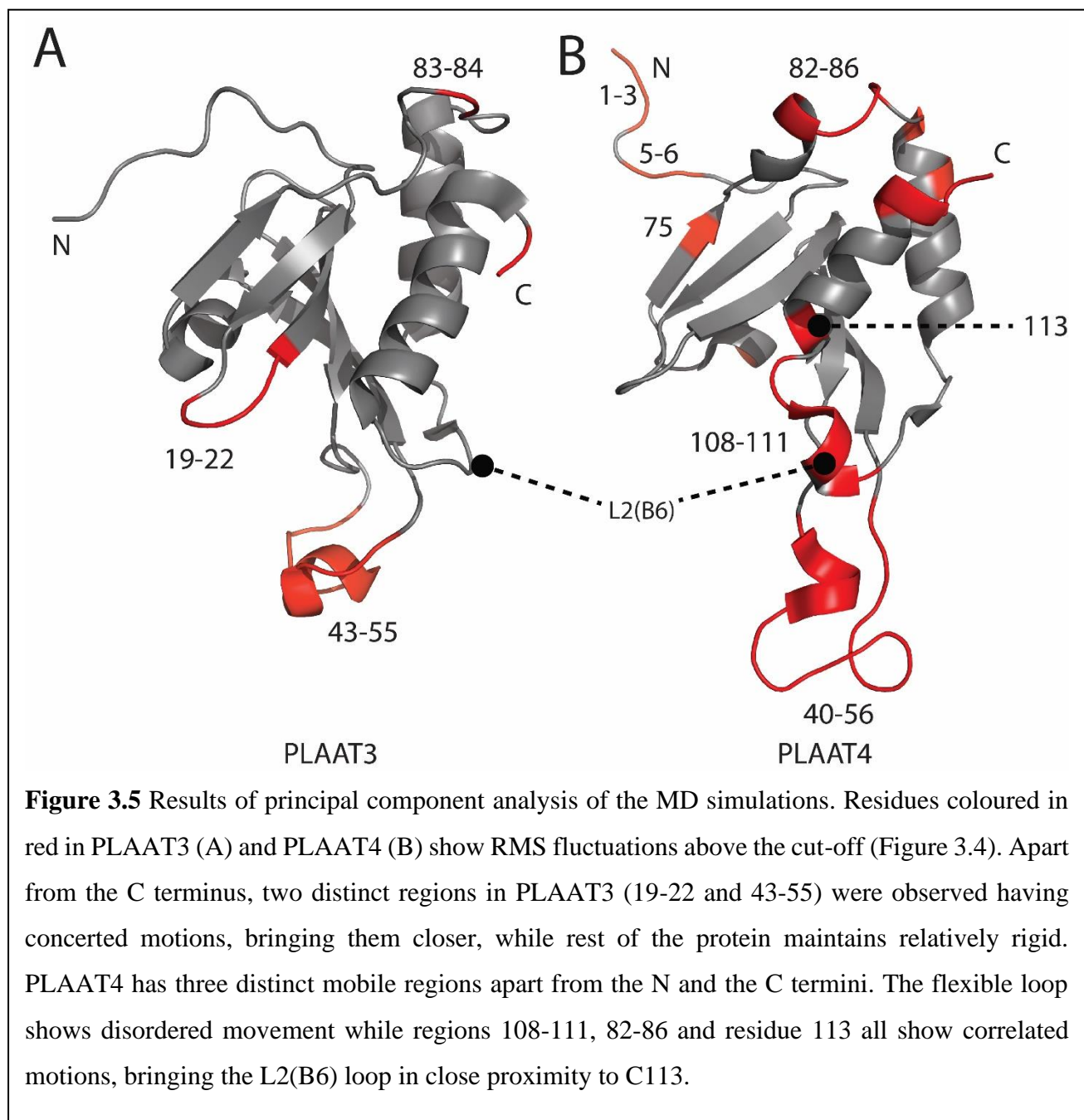
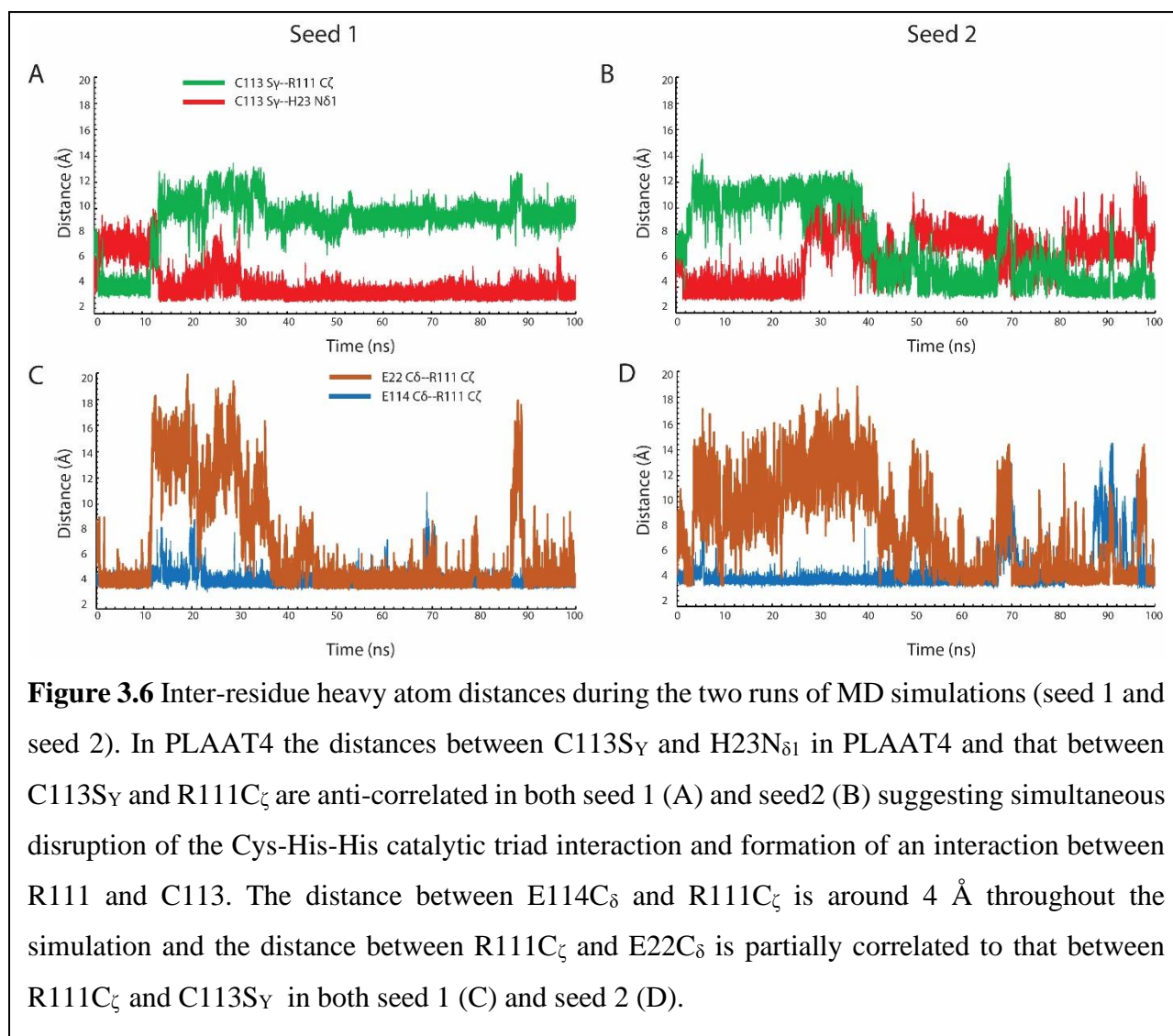


Figure 3.4 Fluctuations per residue. For each residue, the largest RMS fluctuation of all its atoms along the two largest eigenvectors of the principal components analysis in the MD runs is plotted for PLAAT3 (A) and PLAAT4 (B). A cut-off of 2 Å is indicated with a dashed line. Secondary structure of the starting structure is indicated at the top and named as per Table 2.1.

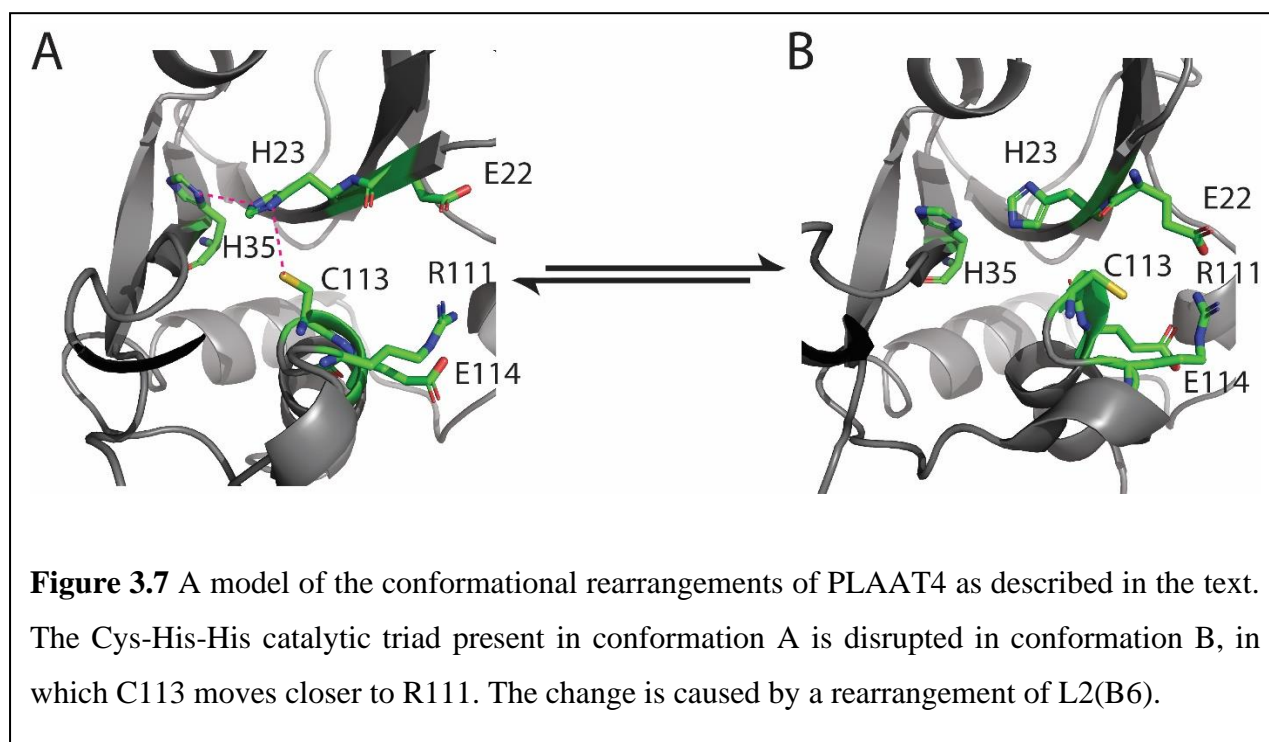




Discussion

Based on the observations obtained from both fast and slow timescale protein dynamics NMR experiments, as well as the MD simulations, a model is proposed for a two-state conformational rearrangement occurring in the catalytic region in PLAAT4, illustrated in Figure 3.7. In the starting structure the nucleophile residue C113 and the base residue H23 interact via a hydrogen bond. H23 is bound to H35, as part of the catalytic triad (panel A). The C113-H23 interaction can be broken and the imidazole rotates away. Simultaneously, L2(B6) and A3 rearrange, bringing the side-chains of R111 and C113 closer to form a new state. The observation of this mobility is in line with the experimental evidence for motion in this region. Nine out of 11 residues comprising L2(B6) in PLAAT4 either lack resonance assignments due to line broadening or show fast timescale dynamics. In PLAAT3 such dynamics is not observed.

Thus, these observations raise the question whether the mobility of L2(B6) relates to the activity difference between PLAAT3 and PLAAT4. Increased flexibility could play a role in substrate accessibility or induced fit. Since both PLAAT3 and PLAAT4 are membrane-anchored enzymes, a better substrate accessibility could lead to a higher (phospholipase) activity. To test this hypothesis, it would be interesting to test whether L2(B6) loop exchange between the two proteins would lead to different activities. Also interesting would be to study if this L2(B6) loop mobility affects native salt-bridge networks in PLAAT3 and PLAAT4 since salt bridges might infer protein rigidity/flexibility.^{39,40} The findings are presented in chapter 4.



Materials and Methods

MD simulations were performed using Gromacs-5.1.^{38,23} The NMR structure of PLAAT3 (2KYT)⁴¹ and PLAAT4 (2MY9)⁴² were selected for the simulations as starting structures and topology files were created from them. The AMBER ff99sb-ILDN force-field provided with GROMACS was used.⁴³ The models were then solvated in a periodic water box of 1 nm and 2 nm cubic edge length for (PLAAT3) and (PLAAT4), respectively. The latter is larger due to the elongated conformation of the protein. The TIP3P water model was used.^{44,45} Three Na⁺ counterions were automatically placed by the GROMACS program throughout the water box such that the final system had net zero charge. After solvation and neutralization, the systems were energy minimized by 5000 steps of minimization using the steepest descent algorithm. Minimized systems were further equilibrated under NVT and NPT conditions for 500 ps with a step size of 2 fs using position restraints on the protein and a temperature of 300 K and 1 atm. pressure controlled by the velocity rescaling (modified Berendsen) thermostat⁴⁶ and Parrinello-Rahman barostat.⁴⁷ The equilibrated systems were finally subjected to a 100 ns simulation run under NPT without any position restraints, and coordinates were saved after every ps. Two simulations were carried out with different starting seeds for both PLAAT3 and PLAAT4 where each seed represents a simulation at a different velocity. The trajectories were analysed using the inbuilt modules available in the GROMACS suite and visualized by means of the VMD⁴⁸/Chimera⁴⁹ program.

Principal component analysis was carried out by first building the covariance matrix of atomic fluctuations and then generating a set of eigenvectors and eigenvalues by the diagonalization of the covariance matrix. The two eigenvectors that corresponded to the two largest eigenvalues were chosen as the principal components describing most of the collective motions or essential dynamics. The residues involved in these two largest eigenvectors were extracted by using a cut-off of 2 Å RMS fluctuations of individual atoms described by the two eigenvectors using an in-house program. The motions of these residues were further analysed by observing the MD trajectory.

Supplementary Figures

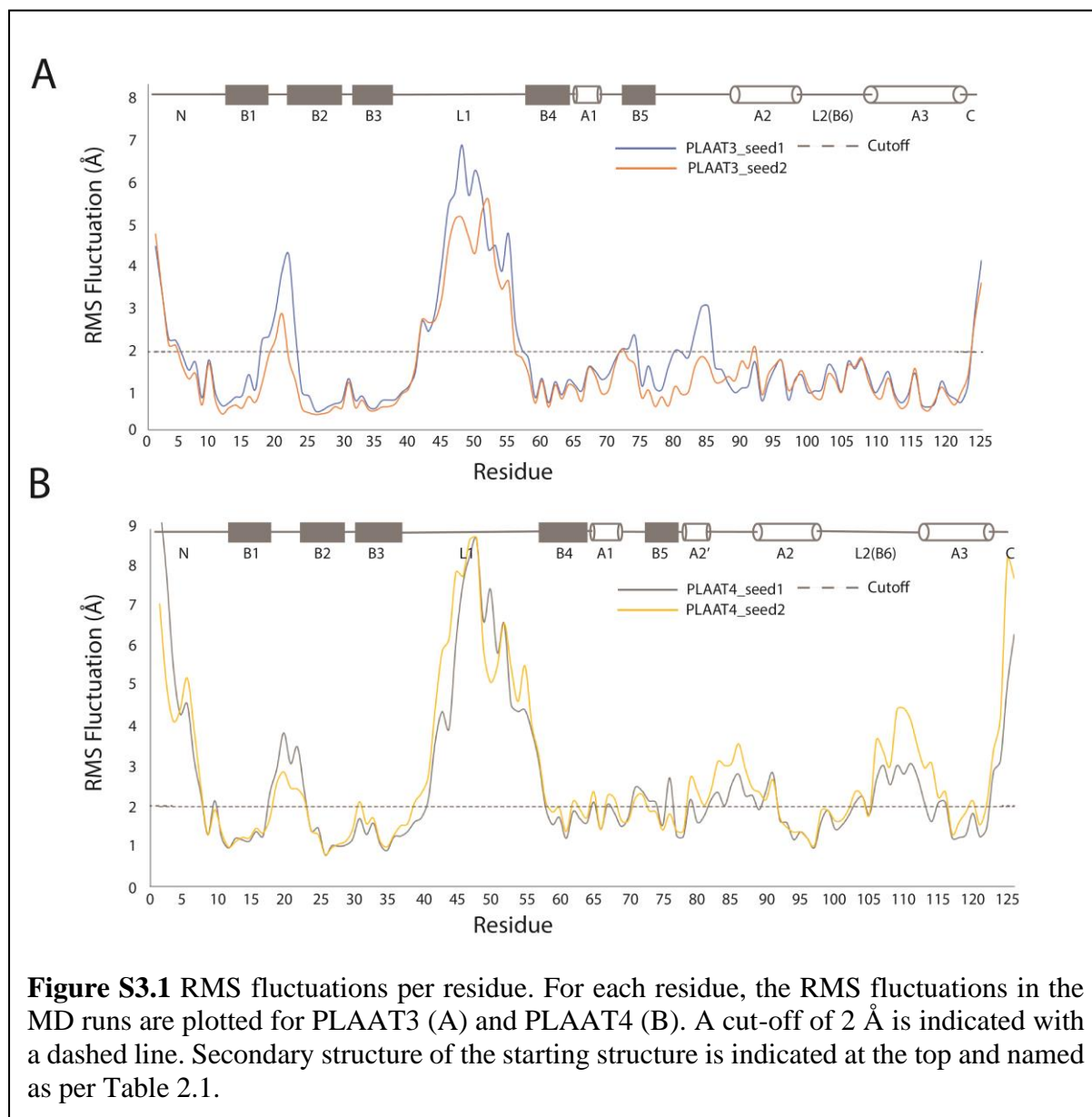
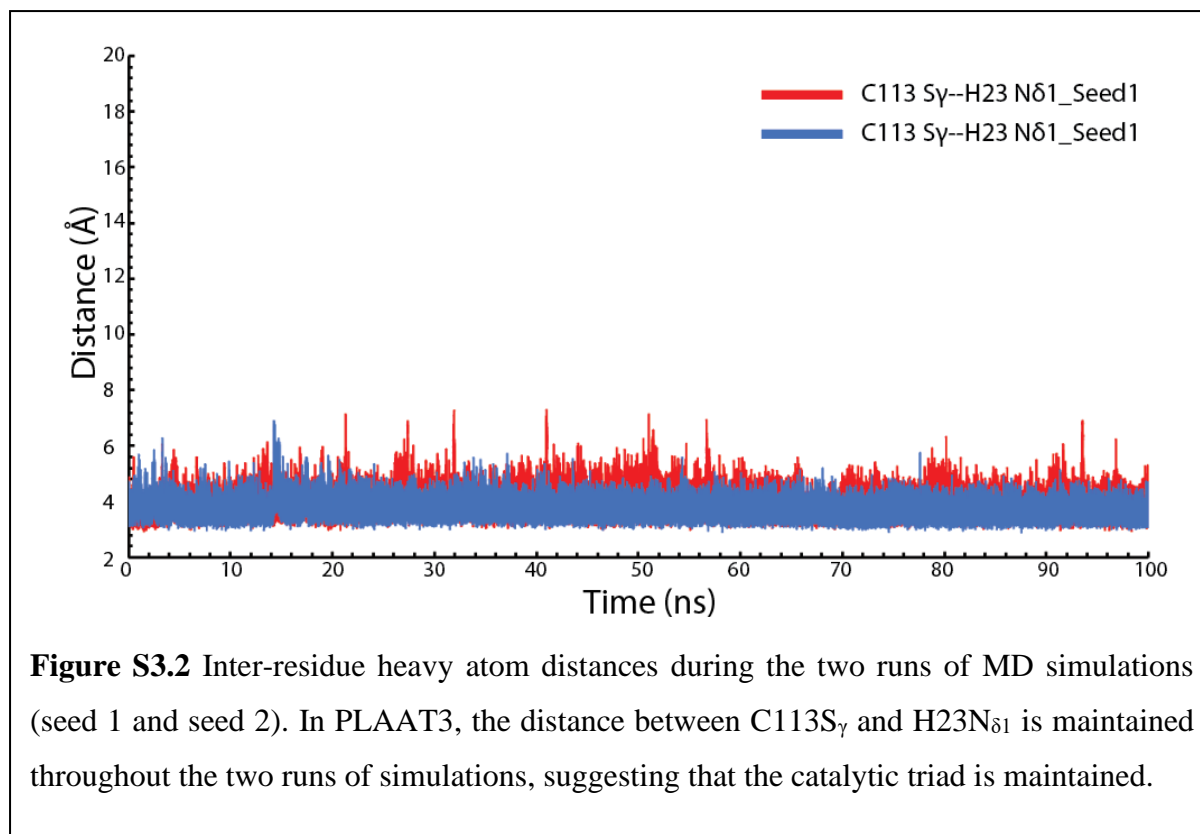


Figure S3.1 RMS fluctuations per residue. For each residue, the RMS fluctuations in the MD runs are plotted for PLAAT3 (A) and PLAAT4 (B). A cut-off of 2 Å is indicated with a dashed line. Secondary structure of the starting structure is indicated at the top and named as per Table 2.1.



References

- (1) Chu, Y.-P., Chang, C.-H., Shiu, J.-H., Chang, Y.-T., Chen, C.-Y., and Chuang, W.-J. (2011) Solution structure and backbone dynamics of the DNA-binding domain of FOXP1: insight into its domain swapping and DNA binding. *Protein Sci.* 20, 908–924.
- (2) Moorman, V. R., Valentine, K. G., Bédard, S., Kasinath, V., Dogan, J., Love, F. M., and Wand, A. J. (2014) Dynamic and thermodynamic response of the Ras protein Cdc42Hs upon association with the effector domain of PAK3. *J. Mol. Biol.* 426, 3520–3538.
- (3) Guenneugues, M., Gilquin, B., Wolff, N., Ménez, A., and Zinn-Justin, S. (1999) Internal motion time scales of a small, highly stable and disulfide-rich protein: A 15N, 13C NMR and molecular dynamics study. *J. Biomol. NMR* 14, 47–66.
- (4) Chua, C. E. L., and Tang, B. L. (2015) The role of the small GTPase Rab31 in cancer. *J. Cell. Mol. Med.* 19, 1–10.
- (5) Ma, L., Sham, Y. Y., Walters, K. J., and Towle, H. C. (2007) A critical role for the loop region of the basic helix-loop-helix/leucine zipper protein Mlx in DNA binding and glucose-regulated transcription. *Nucleic Acids Res.* 35, 35–44.
- (6) Sunada, S., and Go, N. (1996) Calculation of nuclear magnetic resonance order parameters in proteins by normal mode analysis. II. Contribution from localized high frequency motions. *J. Chem. Phys.* 105, 6560–6564.
- (7) Gu, Y., Li, D.-W., and Brüschweiler, R. (2014) NMR order parameter determination from long molecular dynamics trajectories for objective comparison with experiment. *J. Chem. Theory Comput.* 10, 2599–2607.
- (8) Chalmers, G., Glushka, J. N., Foley, B. L., Woods, R. J., and Prestegard, J. H. (2016) Direct NOE simulation from long MD trajectories. *J. Magn. Reson.* 265, 1–9.
- (9) Tolman, J. R., Al-Hashimi, H. M., Kay, L. E., and Prestegard, J. H. (2001) Structural and dynamic analysis of residual dipolar coupling data for proteins. *J. Am. Chem. Soc.* 123, 1416–1424.
- (10) McCammon, J. A., Gelin, B. R., and Karplus, M. (1977) Dynamics of folded proteins. *Nature* 267, 585.
- (11) Krepl, M., Cléry, A., Blatter, M., Allain, F. H. T., and Sponer, J. (2016) Synergy between NMR measurements and MD simulations of protein/RNA complexes: application to the RRM, the most common RNA recognition motifs. *Nucleic Acids Res.* 44, 6452–6470.
- (12) Phillips, J. C., Braun, R., Wang, W., Gumbart, J., Tajkhorshid, E., Villa, E., Chipot, C., Skeel, R. D., Kalé, L., and Schulten, K. (2005) Scalable molecular dynamics with NAMD. *J. Comput. Chem.* 26, 1781–1802.

- (13) Pronk, S., Páll, S., Schulz, R., Larsson, P., Bjelkmar, P., Apostolov, R., Shirts, M. R., Smith, J. C., Kasson, P. M., van der Spoel, D., Hess, B., and Lindahl, E. (2013) GROMACS 4.5: a high-throughput and highly parallel open source molecular simulation toolkit. *Bioinformatics* 29, 845–854.
- (14) Case, D. A., Cheatham 3rd, T. E., Darden, T., Gohlke, H., Luo, R., Merz Jr, K. M., Onufriev, A., Simmerling, C., Wang, B., and Woods, R. J. (2005) The Amber biomolecular simulation programs. *J. Comput. Chem.* 26, 1668–1688.
- (15) Dror, R. O., Dirks, R. M., Grossman, J. P., Xu, H., and Shaw, D. E. (2012) Biomolecular simulation: a computational microscope for molecular biology. *Annu. Rev. Biophys.* 41, 429–452.
- (16) Foloppe, N., and MacKerell Alexander D., J. (2000) All-atom empirical force field for nucleic acids: I. Parameter optimization based on small molecule and condensed phase macromolecular target data. *J. Comput. Chem.* 21, 86–104.
- (17) Duan, Y., Wu, C., Chowdhury, S., Lee, M. C., Xiong, G., Zhang, W., Yang, R., Cieplak, P., Luo, R., Lee, T., Caldwell, J., Wang, J., and Kollman, P. (2003) A point-charge force field for molecular mechanics simulations of proteins based on condensed-phase quantum mechanical calculations. *J. Comput. Chem.* 24, 1999–2012.
- (18) Cornell, W. D., Cieplak, P., Bayly, C. I., Gould, I. R., Merz, K. M., Ferguson, D. M., Spellmeyer, D. C., Fox, T., Caldwell, J. W., and Kollman, P. A. (1995) A second generation force field for the simulation of proteins, nucleic acids, and organic molecules. *J. Am. Chem. Soc.* 117, 5179–5197.
- (19) Kollman, P. A. (1996) Advances and continuing challenges in achieving realistic and predictive simulations of the properties of organic and biological molecules. *Acc. Chem. Res.* 29, 461–469.
- (20) Oostenbrink, C., Villa, A., Mark, A. E., and Van Gunsteren, W. F. (2004) A biomolecular force field based on the free enthalpy of hydration and solvation: The GROMOS force-field parameter sets 53A5 and 53A6. *J. Comput. Chem.* 25, 1656–1676.
- (21) Schuler, L. D., Daura, X., and van Gunsteren, W. F. (2001) An improved GROMOS96 force field for aliphatic hydrocarbons in the condensed phase. *J. Comput. Chem.* 22, 1205–1218.
- (22) Brooks, B. R., Brooks 3rd, C. L., Mackerell Jr, A. D., Nilsson, L., Petrella, R. J., Roux, B., Won, Y., Archontis, G., Bartels, C., Boresch, S., Caflisch, A., Caves, L., Cui, Q., Dinner, A. R., Feig, M., Fischer, S., Gao, J., Hodoscek, M., Im, W., Kuczera, K., Lazaridis, T., Ma, J., Ovchinnikov, V., Paci, E., Pastor, R. W., Post, C. B., Pu, J. Z., Schaefer, M., Tidor, B.,

- Venable, R. M., Woodcock, H. L., Wu, X., Yang, W., York, D. M., and Karplus, M. (2009) CHARMM: the biomolecular simulation program. *J. Comput. Chem.* 30, 1545–1614.
- (23) Hess, B., Kutzner, C., van der Spoel, D., and Lindahl, E. (2008) GROMACS 4: algorithms for highly efficient, load-balanced, and scalable molecular simulation. *J. Chem. Theory Comput.* 4, 435–447.
- (24) Roux, B., and Simonson, T. (1999) Implicit solvent models. *Biophys. Chem.* 78, 1–20.
- (25) Jorgensen, W. L., Chandrasekhar, J., Madura, J. D., Impey, R. W., and Klein, M. L. (1983) Comparison of simple potential functions for simulating liquid water. *J. Chem. Phys.* 79, 926–935.
- (26) Mahoney, M. W., and Jorgensen, W. L. (2000) A five-site model for liquid water and the reproduction of the density anomaly by rigid, nonpolarizable potential functions. *J. Chem. Phys.* 112, 8910–8922.
- (27) Berendsen, H. J. C., Grigera, J. R., and Straatsma, T. P. (1987) The missing term in effective pair potentials. *J. Phys. Chem.* 91, 6269–6271.
- (28) Shao, J., Tanner, S. W., Thompson, N., and Cheatham, T. E. (2007) Clustering molecular dynamics trajectories: 1. characterizing the performance of different clustering algorithms. *J. Chem. Theory Comput.* 3, 2312–2334.
- (29) Karpen, M. E., Tobias, D. J., and Brooks, C. L. (1993) Statistical clustering techniques for the analysis of long molecular dynamics trajectories: analysis of 2.2-ns trajectories of YPGDV. *Biochemistry* 32, 412–420.
- (30) Shenkin, P. S., and McDonald, D. Q. (2018) Cluster analysis of molecular conformations. *J. Comput. Chem.* 15, 899–916.
- (31) David, C. C., and Jacobs, D. J. (2014) Principal component analysis: a method for determining the essential dynamics of proteins. *Methods Mol. Biol.* 1084, 193–226.
- (32) Berendsen, H. J. C., and Hayward, S. (2000) Collective protein dynamics in relation to function. *Curr. Opin. Struct. Biol.* 10, 165–169.
- (33) Amadei, A., Linssen, A. B. M., de Groot, B. L., van Aalten, D. M. F., and Berendsen, H. J. C. (1996) An efficient method for sampling the essential subspace of proteins. *J. Biomol. Struct. Dyn.* 13, 615–625.
- (34) Amadei, A., Linssen, A. B. M., and Berendsen, H. J. C. (2018) Essential dynamics of proteins. *Proteins Struct. Funct. Bioinforma.* 17, 412–425.
- (35) Salsbury, F. R., Crowder, M. W., Kingsmore, S. F., and Huntley, J. J. A. (2008) Molecular dynamic simulations of the metallo-beta-lactamase from *Bacteroides fragilis* in the presence and absence of a tight-binding inhibitor. *J. Mol. Model.* 15, 133.

- (36) Wrabl, J. O., Shortle, D., and Woolf, T. B. (2000) Correlation between changes in nuclear magnetic resonance order parameters and conformational entropy: Molecular dynamics simulations of native and denatured staphylococcal nuclease. *Proteins Struct. Funct. Bioinforma.* 38, 123–133.
- (37) Radkiewicz, J. L., and Brooks, C. L. (2000) Protein dynamics in enzymatic catalysis: exploration of dihydrofolate reductase. *J. Am. Chem. Soc.* 122, 225–231.
- (38) Van Der Spoel, D., Lindahl, E., Hess, B., Groenhof, G., Mark, A. E., and Berendsen, H. J. C. (2005) GROMACS: Fast, flexible, and free. *J. Comput. Chem.* 26, 1701–1718.
- (39) Panja, A. S., Maiti, S., and Bandyopadhyay, B. (2020) Protein stability governed by its structural plasticity is inferred by physicochemical factors and salt bridges. *Sci. Rep.* 10, 1822.
- (40) Mamonova, T. B., Glyakina, A. V, Galzitskaya, O. V, and Kurnikova, M. G. (2013) Stability and rigidity/flexibility—Two sides of the same coin? *Biochim. Biophys. Acta - Proteins Proteomics* 1834, 854–866.
- (41) Ren, X., Lin, J., Jin, C., and Xia, B. (2010) Solution structure of the N-terminal catalytic domain of human H-REV107--a novel circular permuted NlpC/P60 domain. *FEBS Lett.* 584, 4222–4226.
- (42) Wei, H., Wang, L., Ren, X., Yu, W., Lin, J., Jin, C., and Xia, B. (2015) Structural and functional characterization of tumor suppressors TIG3 and H-REV107. *FEBS Lett.* 589, 1179–1186.
- (43) Lindorff-Larsen, K., Piana, S., Palmo, K., Maragakis, P., Klepeis, J. L., Dror, R. O., and Shaw, D. E. (2010) Improved side-chain torsion potentials for the Amber ff99SB protein force field. *Proteins* 78, 1950–1958.
- (44) Jorgensen, W. L. (1981) Quantum and statistical mechanical studies of liquids. 10. Transferable intermolecular potential functions for water, alcohols, and ethers. Application to liquid water. *J. Am. Chem. Soc.* 103, 335–340.
- (45) Mark, P., and Nilsson, L. (2001) Structure and dynamics of the TIP3P, SPC, and SPC/E water models at 298 K. *J. Phys. Chem. A* 105, 9954–9960.
- (46) Bussi, G., Donadio, D., and Parrinello, M. (2007) Canonical sampling through velocity rescaling. *J. Chem. Phys.* 126, 14101.
- (47) Parrinello, M., and Rahman, A. (1981) Polymorphic transitions in single crystals: A new molecular dynamics method. *J. Appl. Phys.* 52, 7182–7190.
- (48) Humphrey, W., Dalke, A., and Schulten, K. (1996) VMD: Visual molecular dynamics. *J. Mol. Graph.* 14, 33–38.

(49) Pettersen, E. F., Goddard, T. D., Huang, C. C., Couch, G. S., Greenblatt, D. M., Meng, E. C., and Ferrin, T. E. (2004) UCSF Chimera—A visualization system for exploratory research and analysis. *J. Comput. Chem.* 25, 1605–1612.

4

Chapter

Introduction of the PLAAT4 L2(B6) in PLAAT3 disrupts salt bridges and increases activity.

This chapter is based on joint work with Rubin Dasgupta and Juan Zhou.

The work in this chapter was published as: Chatterjee, S. D., Zhou, J., Dasgupta, R., Cramer-Blok, A., Timmer, M., van der Stelt, M., and Ubbink, M. (2021) Protein Dynamics Influence the Enzymatic Activity of Phospholipase A/Acytransferases 3 and 4. *Biochemistry* 60, 1178–1190.

Abstract

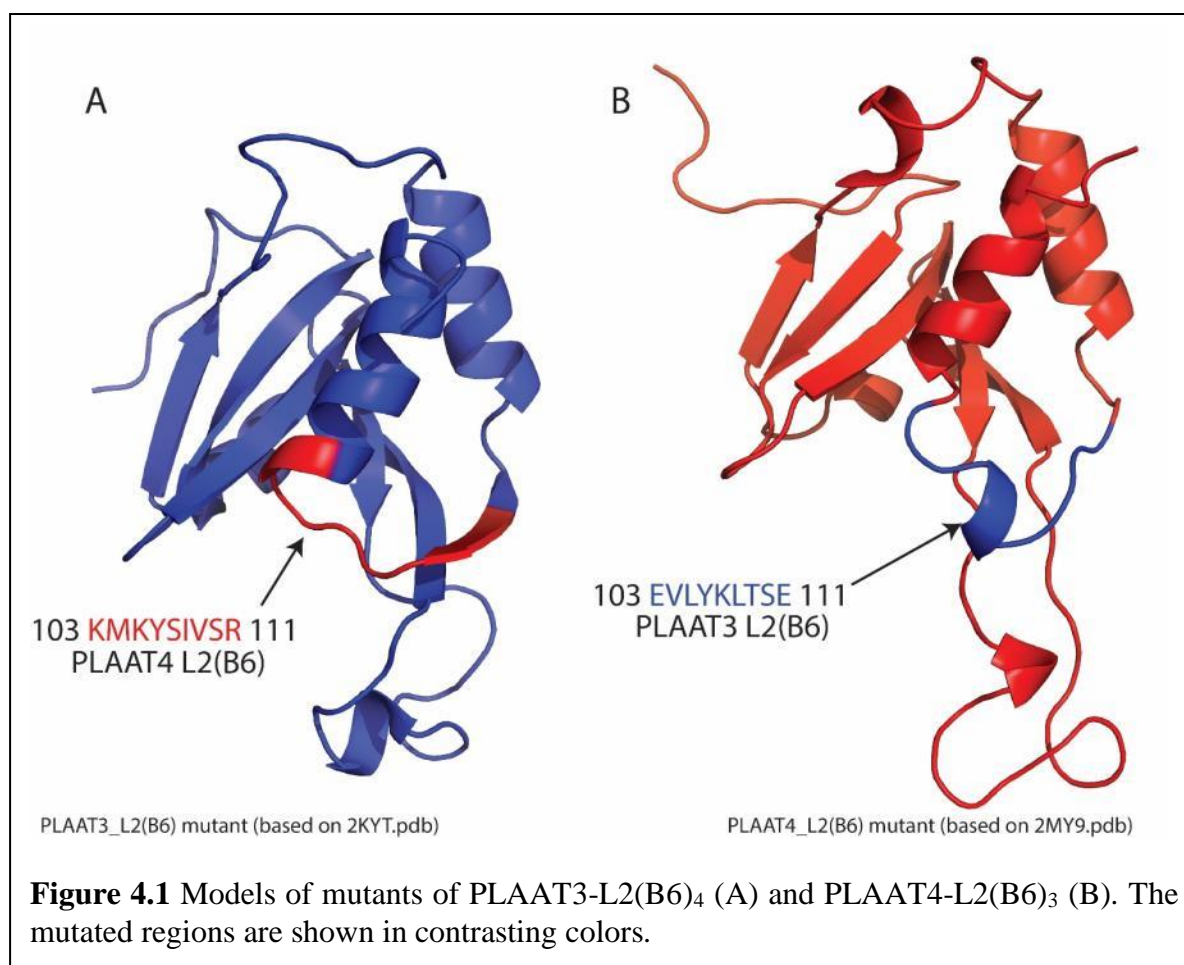
NMR experiments and MD simulations provided us with insights of the differences in dynamics between PLAAT3 and PLAAT4. The rearrangement of L2(B6) loop was found unique to PLAAT4 which prompted us to observe the significance of the loop. Site directed mutagenesis followed by phospholipase assay revealed that swapping of loop L2(B6) in PLAAT3 and PLAAT4 bring about significant increase in activity. On the basis of molecular dynamics simulations, we speculate that this increase in activity is due to the disruption of existing salt bridges in the wild type proteins, thereby rendering the loop-mutants more flexible in order for better substrate accessibility and accommodation as revealed by salt-bridge lifetime analysis.

Introduction

Observations reported in Chapters 2 and 3 provided us with significant insights into the distinct dynamic profiles of the soluble domains of PLAAT3 and PLAAT4. The two proteins differ in the number and dispersion of salt bridges, which is a likely cause for the difference in melting temperature. NMR experiments and MD simulations provided evidence for large differences in dynamics. An interesting rearrangement of loop L2(B6) unique to PLAAT4 was seen, making its active site region more mobile than that of PLAAT3. The main research question being why the two proteins differ in activity, despite sharing similar sequence and structure, we wondered whether the dynamics of loop L2(B6) plays a role in the activity difference. This hypothesis was tested by swapping the L2(B6) region of PLAAT3 and PLAAT4 and studying the effects using *in vitro* activity tests and MD calculations. According to the hypothesis, a gain-of-function in the PLAAT3 variant with the L2(B6) region of PLAAT4 was expected, whereas for PLAAT4 with the L2(B6) region of PLAAT3 the opposite was foreseen.

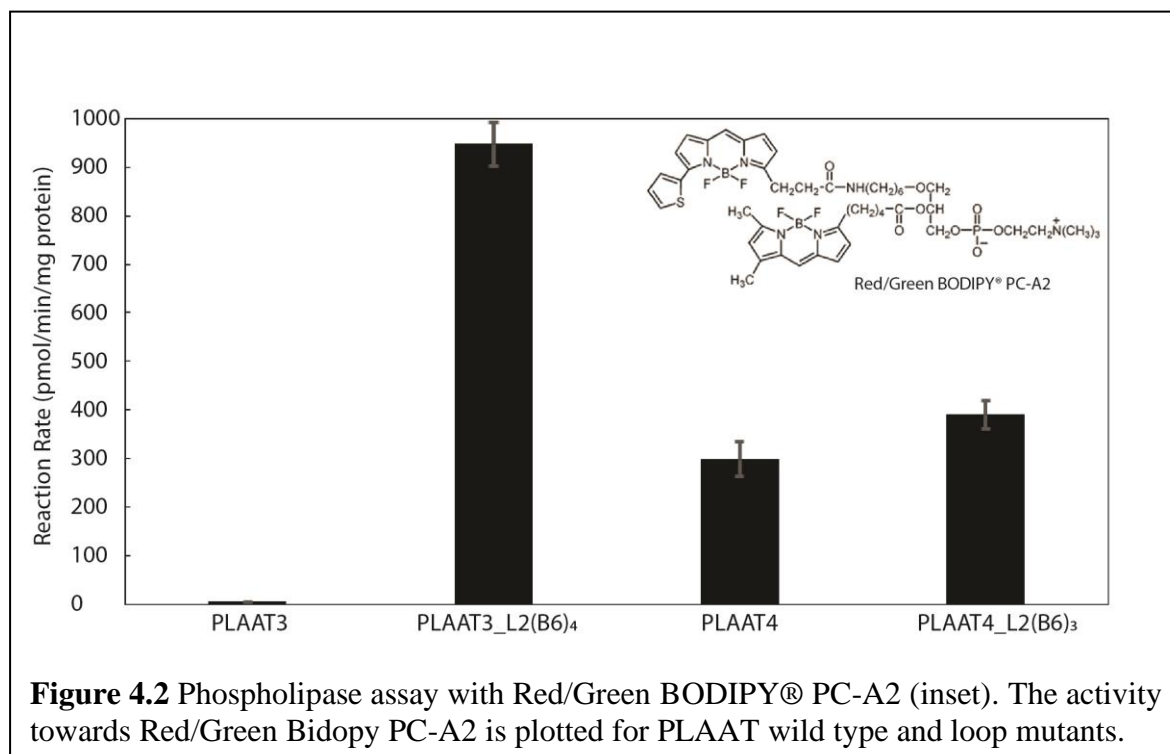
Results

To probe whether the mobility of L2(B6) contributes to the activity of PLAAT4, mutagenesis was performed, both *in silico* and *in vitro*. Wild type PLAAT3 and PLAAT4 were mutated by swapping their L2(B6) loop (residues 103-111) *in vitro* to test whether L2(B6) is critical for conferring enhanced dynamics in PLAAT4 (Figure 4.1). The mutants were named PLAAT3_L2(B6)₄ and PLAAT4_L2(B6)₃ to indicate the mutants of PLAAT3(4) with the L2(B6) region from PLAAT4(3). Phospholipase assay was performed to establish the functional effects of the mutagenesis. The dynamics of the mutants were probed by MD simulations.



Phospholipase assay. A phospholipase assay with the fluorescent substrate Red/Green BODIPYTM PC-A2 was performed to check the activity of both wild type and mutant proteins. The assay releases the green fluorescent fatty acid BODIPYTM FL C5 from the *sn*-2 position of the substrate. The reaction rate (expressed in pmol/min/mg protein) of each protein is plotted in Figure 4.2. The results show that the reaction rate of wild type PLAAT4 was high, whereas wild type PLAAT3 has background activity. Interestingly, PLAAT3_L2(B6) shows a large

increase in the reaction rate. This observation suggests that either the natural L2(B6) in PLAAT3 was inhibiting the activity or that PLAAT4 L2(B6) enables activity. When the PLAAT4 L2(B6) was replaced with the analogous loop of PLAAT3, a small increase in activity was seen, as compared to wild type PLAAT4. Thus, replacement of L2(B6)₃ with L2(B6)₄ in PLAAT3 enables activity, whereas the opposite mutation does not inhibit activity in PLAAT4.



Conformational freedom in the mutants. Molecular dynamics (MD) simulations were performed to sample the trajectories for both the wild type and the L2(B6) mutants for 100 ns. Two seeds starting the simulation at different points in the energy landscape were used. The first model of each of the published NMR structures^{1,2} was used as starting structure for the wild type proteins, whereas the starting structures for the mutants were generated by in silico mutagenesis (Materials and Methods). The fluctuations during the MD runs were visualized by plotting the all-atom RMSD of the L2(B6) as a function of the runtime. The results for the mutants were compared with the corresponding wild type proteins. Insertion of L2(B6)₄ did not significantly alter the overall RMSD of PLAAT3. The RMSD stabilizes around 2.5 Å (Figure 4.3.A). Similarly, the PLAAT4-L2(B6)₃ mutant displays an RMSD trajectory that resembles that of wild type PLAAT4. Wild type and mutant PLAAT4 proteins exhibit larger

RMSD ($\sim 4.5 \text{ \AA}$) than PLAAT3, indicating that PLAAT4 samples a larger structural space than PLAAT3 (Figure 4.3.B).

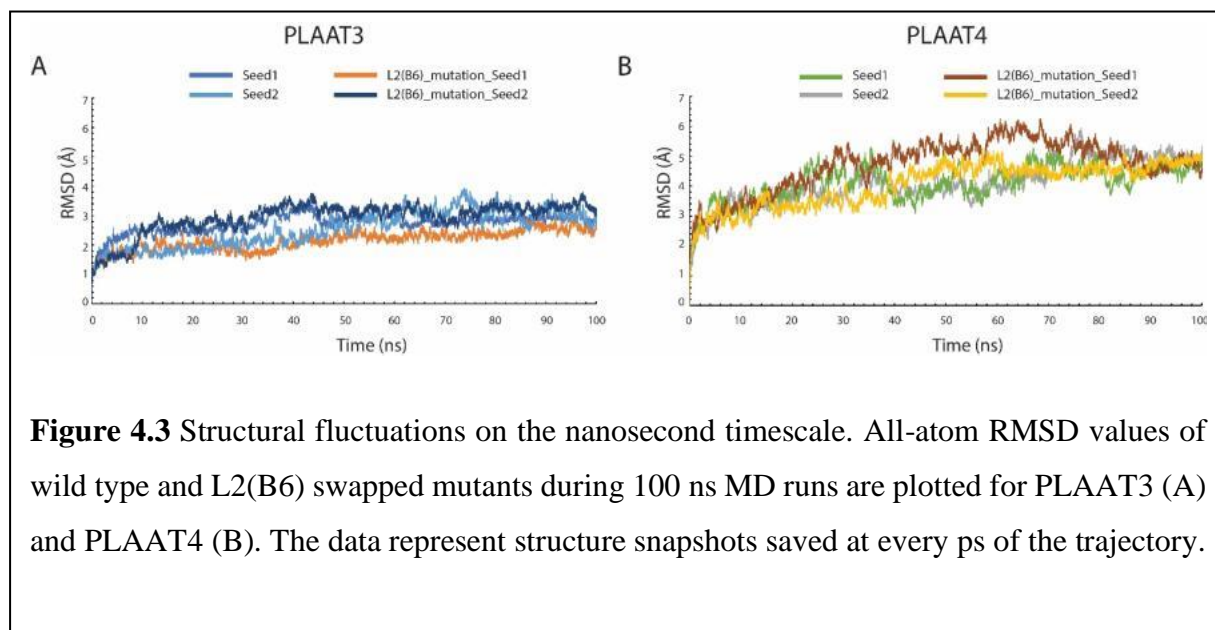
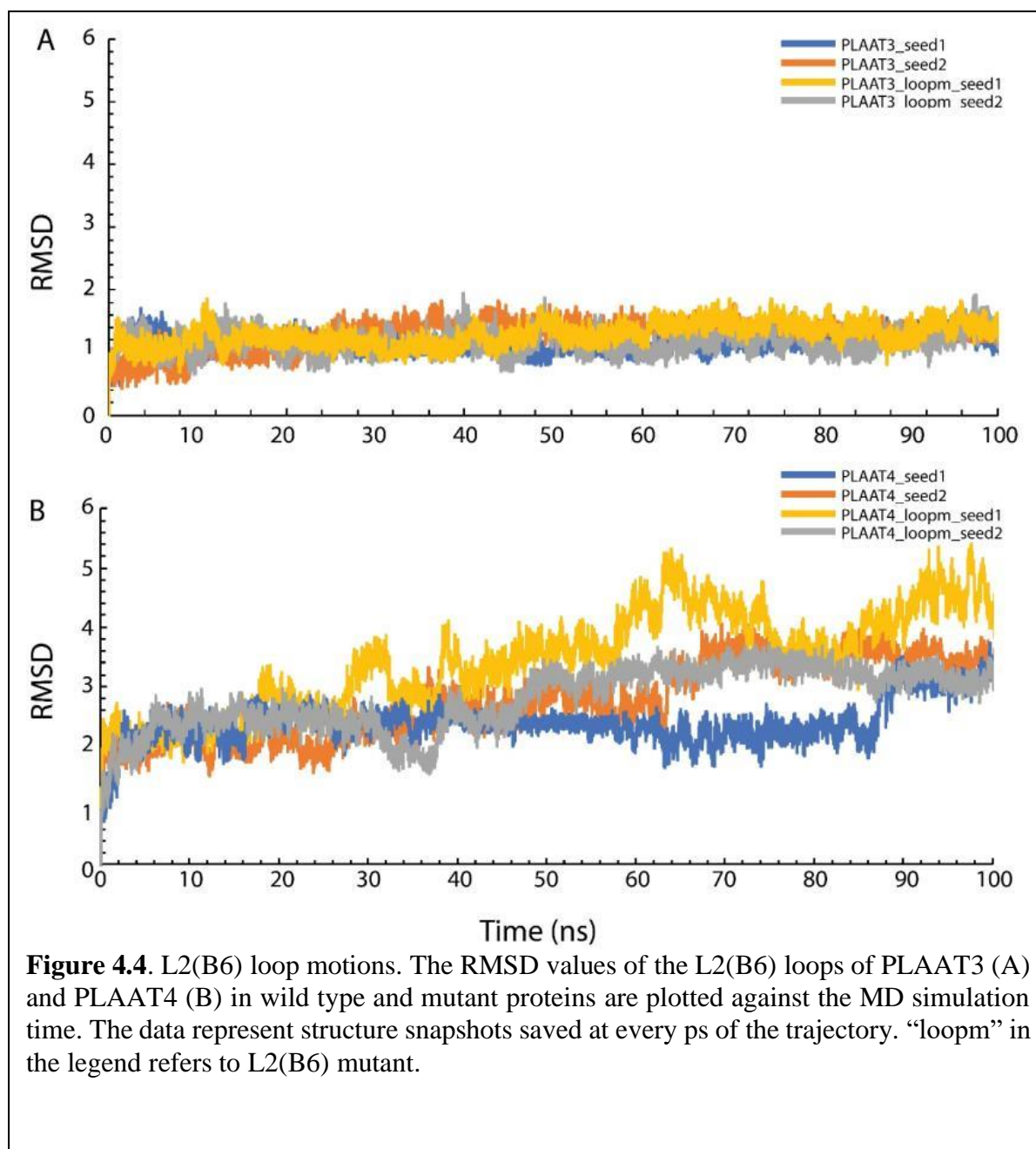


Figure 4.3 Structural fluctuations on the nanosecond timescale. All-atom RMSD values of wild type and L2(B6) swapped mutants during 100 ns MD runs are plotted for PLAAT3 (A) and PLAAT4 (B). The data represent structure snapshots saved at every ps of the trajectory.

Since the overall RMSD is strongly influenced by the presence of the highly dynamic loop L1, the RMSD of the L2(B6) loop alone in both wild type and mutant proteins as a function of the runtime was also analysed (Figure 4.4). Interestingly, substitution of L2(B6)₃ with L2(B6)₄ did not significantly increase the conformational freedom of the loop in PLAAT3 (Figure 4.4A). Analogously, in PLAAT4 the large motions of the loop in the wild type protein are not reduced by introduction of L2(B6)₃. The motions rather appear to be enhanced somewhat (Figure 4.4B).



To test for the presence of larger, correlated motions that influence the accessibility of the active site, the variation of the length of two vectors connecting distant parts of the proteins was analysed. The first vector runs along the His residues of the catalytic triad and connects the C α atoms of residues R22 and K62, which are located in different strands of the twisted β -sheet. The second vector is oriented roughly perpendicular, going across the active site and connecting the C α atoms of residues V68 (α -helix A1) and C113, the active site cysteine residue (α -helix A3), see Figure 4.5. In the MD runs of both wild type and mutant PLAAT3, the length of vector 1 is stable at 18 Å, with rapid fluctuations of about 1 Å, indicating a lack of correlated

motions along this vector over the time of the simulation. For the wild type PLAAT3 the vector connecting V68 and C113 is also stable at 13-14 Å, after initial equilibration during the first 10-15 ns. For PLAAT3_L2(B6)₄ the vector shows more variation with a large excursion to 18 Å for about 10 ns in one of the runs and shorter excursions to increased length in the other run (Figure 4.5). This could be an indication that PLAAT3_L2(B6)₄ undergoes relatively slow, correlated motions that affect the active site. For PLAAT4, a similar analysis shows that also here vector 1 has a stable length over the time of the simulation. Vector 2 shows large excursions with prolonged lifetimes, similar to PLAAT3_L2(B6)₄, for both the wild type PLAAT4 and PLAAT4_L2(B6)₃ (Figure 4.6).

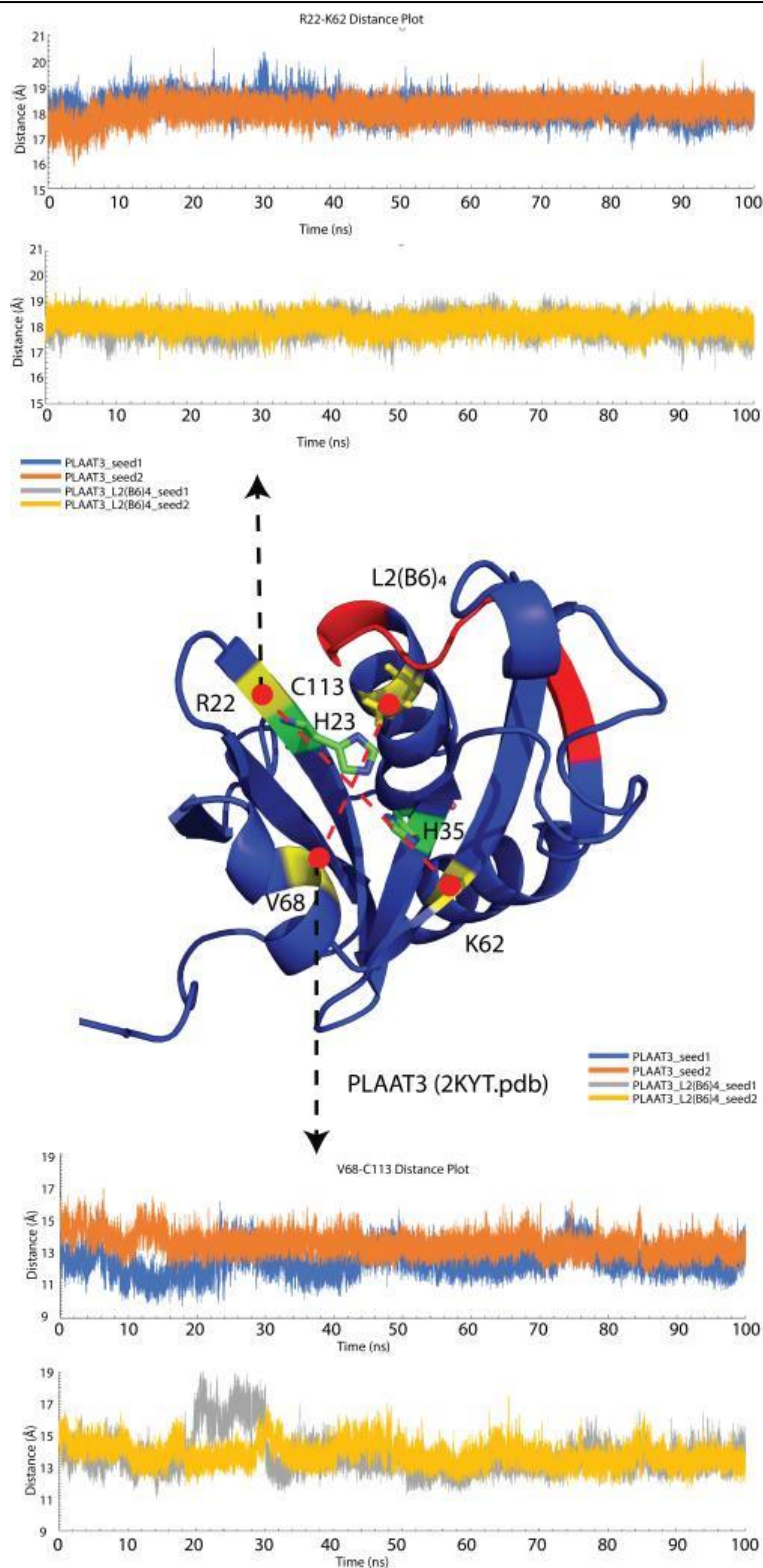
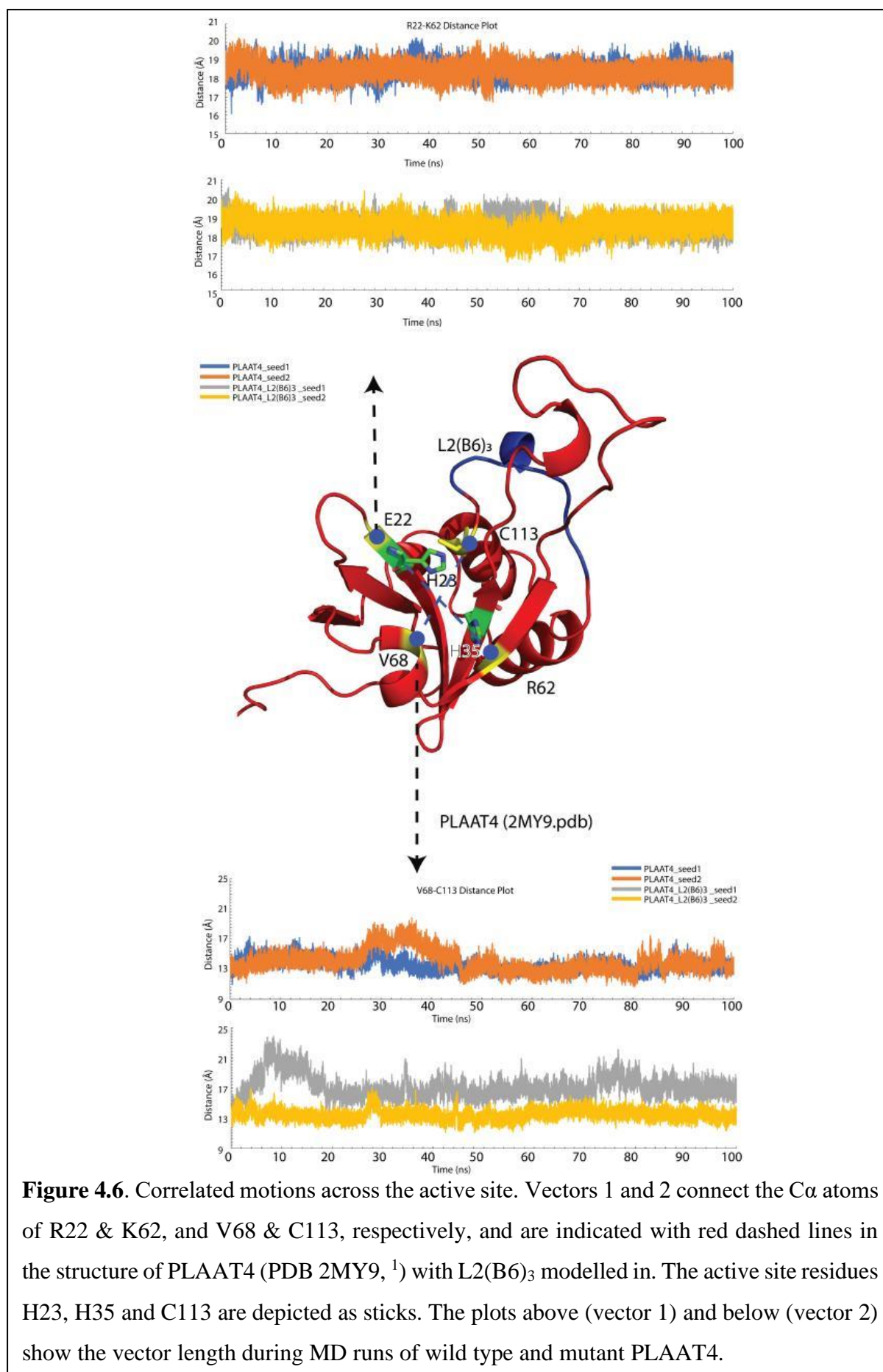


Figure 4.5. Correlated motions across the active site. Vectors 1 and 2 connect the C α atoms of R22 & K62, and V68 & C113, respectively, and are indicated with red dashed lines in the structure of PLAAT3 (PDB 2KYT, ²) with L2(B6)₄ modelled in. The active site residues H23, H35 and C113 are depicted as sticks. The plots above (vector 1) and below (vector 2) show the vector length during MD runs of wild type and mutant PLAAT3.



Salt-bridges. Another measure of structural integrity is the presence of salt bridges during the MD run. For regions that sample the same conformations in wild type and mutant forms of the protein, it is expected that salt bridges are formed during the same fraction of the time. The presence of salt bridges was sampled every 10 ps over the entire MD trajectory and considered significant if the interaction was present on average over two runs for at least 20% of the time. Surprisingly large differences were found between wild type and loop mutants. In wild type PLAAT3, 11 salt bridges were identified (Table 4.1, Figure 4.7), whereas in PLAAT3_L2(B6)₄ only five of these remained. The lost interactions involved residues in the L2B6 loop but also across the active site and even at the other end of the protein. Residues that lose the bridges found in the wild type protein form new ones with other charged residues. A similar picture arises from the data of PLAAT4. Out of seven salt-bridges in wild type PLAAT4, only three were found in PLAAT4_L2(B6)₃ (Table 4.2, Figure 4.7). The lost bridges are in the loop, the active site and around D81, at the other end of the protein. Only one new salt-bridge was found in PLAAT4_L2(B6)₃. It is concluded that, despite the lack of changes in the overall and loop RMSD, the average structures clearly differ in details between wild type and loop mutants.

Table 4.1. Salt bridges in PLAAT3. The populations of salt bridges (in %) in PLAAT3 and PLAAT3_L2(B6)₄ during 100 ns MD runs are reported for two runs (Seeds 1 and 2). Average populations of $\geq 20\%$ are considered significant. Interactions that are insignificant are shown underlined. Salt bridges absent in wild type PLAAT3 but observed in PLAAT3_L2(B6)₄ are demarcated by a solid line (salt bridges in 12-14).

Populations (%)							
	Salt Bridges	WT Seed 1	WT Seed 2	Average	L2(B6) ₄ Seed 1	L2(B6) ₄ Seed 2	Average
1	ASP12--LYS9	29	20	24.5	12	33	22.5
2	ASP67--ARG2	10	31	20.5	5	0	<u>2.5</u>
3	ASP72--ARG18	24	39	31.5	35	5	20
4	ASP81-- ARG121	3	80	41.5	0	0	<u>0</u>
5	ASP82--LYS83	29	25	27	0	8	<u>4</u>
6	GLU103-- LYS57	34	42	38	0	0	<u>0</u>
7	GLU114-- LYS79	13	33	23	32	20	26
8	GLU15-- ARG22	23	31	27	24	4	<u>14</u>
9	GLU41--LYS61	53	54	53.5	17	1	<u>9</u>
10	GLU63--HIS35	44	39	41.5	35	35	35
11	GLU97--LYS62	43	43	43	51	47	49
12	ASP12-- ARG121	0	0	<u>0</u>	75	6	40.5
13	ASP56--LYS57	4	2	<u>3</u>	34	27	30.5
14	GLU119-- HIS115	0	6	<u>3</u>	0	29	<u>14.5</u>
15	GLU98-- ARG95	0	1	<u>0.5</u>	11	43	27

Table 4.2. Salt bridges in PLAAT4. The populations of salt bridges (in %) in PLAAT4 and PLAAT4_L2(B6)₃ during 100 ns MD runs are reported for two runs (Seeds 1 and 2). Average populations of $\geq 20\%$ are considered significant. Interactions that are insignificant are shown in underlined. Salt bridges absent in wild type PLAAT4 but observed in PLAAT4_L2(B6)₃ are demarcated by a solid line (salt bridge in 8).

Populations (%)							
	Salt Bridges	Seed 1	Seed 2	Average	L2(B6)₃ Seed 1	L2(B6)₃ Seed 2	Average
1	ASP12--LYS9	25	43	34	43	33	38
2	ASP67-- ARG64	35	32	33.5	23	42	32.5
3	ASP81-- ARG121	36	49	42.5	0	17	<u>8.5</u>
4	GLU114-- ARG111	39	46	42.5	0	0	<u>0</u>
5	GLU15-- ARG75	19	35	27	49	66	57.5
6	GLU22-- ARG111	37	17	27	0	0	<u>0</u>
7	GLU59-- LYS103	31	28	29.5	0	0	<u>0</u>
8	GLU111-- HIS23	0	0	<u>0</u>	0	32	<u>16</u>

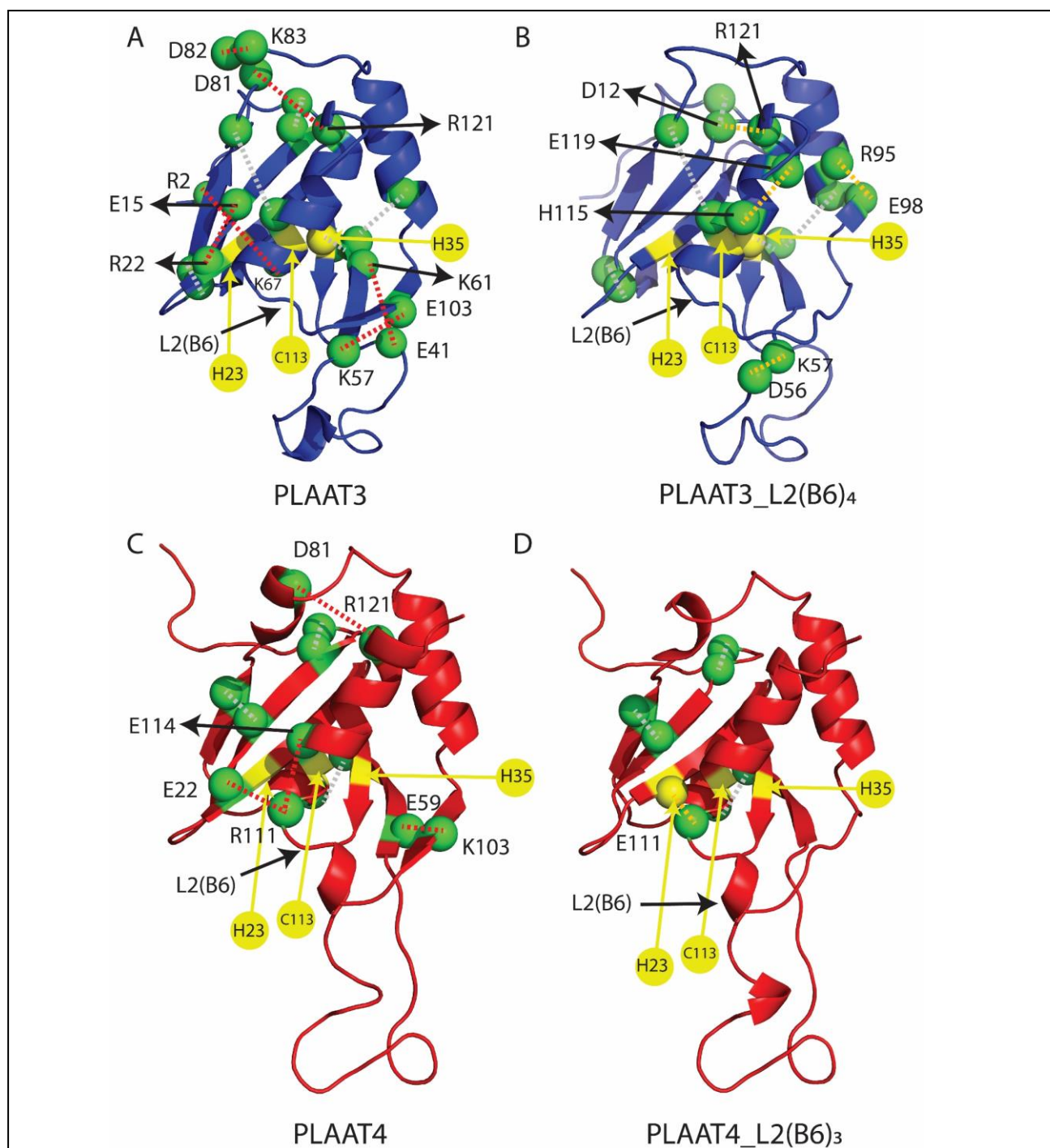


Figure 4.7 Salt bridges in wild type and loop mutant PLAAT proteins. Residues involved in salt bridges with a combined average lifetime of at least 20% in the two 100 ns MD runs are shown with green spheres for $C\alpha$ atoms. Dashed lines indicate the presence of salt bridges between the side chains of the connected residues, in wild type only (red), wild type and mutant (grey) or mutant only (yellow), for PLAAT3 (A), PLAAT3_L2(B6)₄ (B), PLAAT4 (C) and PLAAT4_L2(B6)₃ (D). The residues of the catalytic triad are marked in yellow.

Discussion

While further investigating the cause of differences in PLAAT3/4 phospholipase activity, we gathered interesting observations from the last two chapters on whose basis, we formed a hypothesis. We found that PLAAT4 is inherently more dynamic than PLAAT3 due to less salt bridges and that residues around the PLAAT4 active site might have more solvent accessibility, due to L2(B6) mobility. In this chapter we performed experiments and simulations to test our hypothesis.

The phospholipase assay showed that wild type PLAAT4 has a higher reaction rate compared to wild type PLAAT3, which is in agreement with the literature ³. Furthermore, by changing the loop region of PLAAT3 for the loop region of PLAAT4 the activity increases compared to wild type PLAAT3. This strongly indicated that the L2(B6) mutation in PLAAT3 introduced greater dynamics around the active site region causing increased substrate accessibility. However, when PLAAT3 L2(B6) was introduced in PLAAT4, the activity increased as well. Therefore, it can be concluded that the loop region alone does not determine the activity, but it does have a large effect on the activity.

We performed in-silico mutagenesis by swapping the L2(B6) between PLAAT3 and PLAAT4 and performed two runs of MD simulations for 100 ns, followed by an analysis of salt-bridge lifetimes during the MD simulations. We found that the RMSD profiles of PLAAT3 and PLAAT3_L2(B6) were similar, while the RMSD profiles of PLAAT4 and PLAAT4_L2(B6), although distinct in the middle of an MD run, converged at the end of the runs suggesting that the PLAAT4 and PLAAT4_L2(B6) are not very different with respect to conformation. Furthermore, the study of concerted motions of the two opposite vectors involving R22-K62 and V68-C113 residue pairs also did not yield clear differences in dynamics between the wild-type and mutant proteins. As discussed in Chapter 2, PLAAT3 has a well-dispersed network of salt bridges, so the effect of PLAAT4 L2(B6) introduction on the existing salt bridges was analyzed.

Salt bridge life-time analysis revealed that introduction of PLAAT4 L2(B6) in PLAAT3 caused disappearance of 50% existing salt bridges, while adding 5 more in different parts of the structure. The existing salt bridge in the wild type PLAAT3 L2(B6) disappeared in the mutant, allowing its movement. This mobility due to lack of salt bridges might be crucial for greater

solvent accessibility. A similar effect was observed in PLAAT4_L2(B6)₃, which caused disappearance of 50% existing salt bridges in PLAAT4 suggesting that the swapping of L2(B6) changes the chemical environment and existing salt bridge networks in both PLAAT3 and PLAAT4. This observation, along with the data from phospholipase assay, strongly support our hypothesis that the L2(B6) mutation in PLAAT3 restructured the salt bridges and introduced greater dynamics around the active site region, causing increased substrate accessibility. Further analysis on the structure is needed to determine how these loop residues alter the activities.

Materials and Methods

Mutagenesis. Fragment-based mutagenesis⁴ was carried out by forward and reverse primers (final concentration of 12 μ M) designed to swap the L2(B6) loop of PLAAT3 (103E-V-L-Y-K-L-T-S-E111) with that of PLAAT4 (103K-M-K-Y-S-I-V-S-R111) and vice versa. PCR amplification of the two fragments were performed by a cycle of the following temperature steps- 95°C for 10 minutes followed by 25 cycles of 95°C for 30 seconds, 55°C for 30 seconds, 68°C for 1 minute followed by termination of the reaction at 68°C for 10 minutes. The amplified fragments obtained thereby were purified (GFXTM PCR DNA purification Kit, GE Healthcare) and combined using a second similar PCR step before subcloning into *E. coli* KA797 cells using the common NcoI and XhoI restriction sites in the PLAAT genes.

Protein Production and Purification. DNA sequences encoding the human N-terminal soluble form (residues 1–125) of PLAAT3 or PLAAT4 (Uniprot ID P53816 and Q9UL19, respectively) with N-terminal His₆ tag and a TEV cleavage site were ordered from GeneArt. The fragments were inserted in-frame into bacterial expression vector pET-28a using the NcoI and XhoI restriction sites. Chemically competent *Escherichia coli* BL21-DE3pLys cells were transformed with the plasmids for protein production. The bacteria were cultured overnight in 50 mL of LB medium with 50 μ g/mL kanamycin at 37°C under shaking. 5 mL of the overnight pre-culture was transferred to 500 mL LB medium with 50 μ g/mL kanamycin. When the OD₆₀₀ reached 0.6, the temperature was lowered to 22°C and gene expression was induced by addition of 0.5 mM IPTG. The culture was incubated for 5 hours before cells were harvested by centrifugation at 6000 rpm at 4°C. The pellet was resuspended in 5 mL of 50 mM Tris-HCl buffer (pH 7.5) followed by freezing at -80°C overnight. The cells were thawed the next day in presence of DNase I and lysozyme and lysed by French press. The lysate was centrifuged at

4°C at 25000g for 45 min. The supernatant of the cell lysate containing the His₆-tagged soluble protein was then loaded on a HiTrap-Nickel column, equilibrated with 50 mM Tris pH 7.5, 500 mM NaCl and 5 mM Imidazole. The protein was eluted using a linear imidazole concentration gradient from 0 to 0.5 M. The collected fractions were pooled and dialyzed overnight using a 3.5 kDa molecular weight cut-off cellulose membrane at 4°C in 50 mM Tris, pH 7.5, 500 mM NaCl, 0.5mM EDTA buffer to remove imidazole. His₆-tagged TEV protease was added for the cleavage of the His₆-tag on PLAAT during dialysis overnight. The mixture was loaded again on a His₆-Trap Nickel column to collect the N-terminal PLAAT3 and PLAAT4 domains. The buffer was changed into 50 mM Tris-HCl, 50 mM NaCl, 10 mM DTT, pH 7.5. The volume of the sample was reduced to 2.5 mL using a 5 kDa MWCO Amicon Ultracentrifugal filter (EMD Millipore) at 2200 g and 15 °C. The concentrated sample was loaded on and eluted from a Superose12 gel filtration column in 30 mM sodium phosphate buffer with 30 mM NaCl and 10 mM DTT at pH 7.0.

Phospholipase assay. [These assays were performed by Juan Zhou.] Protein solutions (200 µL, 0.1 mg/mL) were diluted with equal volume of buffer A (50 mM Tris-HCl, pH 8, 50 mM NaCl, 2 mM DTT). These solutions were added to white 96-well plates (60 µL per well, in triplicate). A standard dilution series of the product BODIPYTM PC-A2 (ThermoFischer Scientific) was prepared in pure DMSO of the following concentrations: 0.0 µM (pure DMSO), 0.005 µM, 0.01 µM, 0.05 µM, 0.1 µM, 0.5 µM, 1 µM. The product was diluted with a 1:1 mixture of buffer A and buffer B (50 mM Tris-HCl pH 8, 100 mM NaCl, 1 mM CaCl₂). The solutions of standards were added in the 96-well plate (100 µL each). The liposome mixture was prepared by mixing DOPC (5.1 µL, 10 mM stock in ethanol), DOPG (5.1 µL, 10 mM stock in ethanol) and the substrate Red/Green BODIPYTM PC-A2 dissolved in pure DMSO (5.1 µL, 1.5 mM, ThermoFischer Scientific). The mixture was injected slowly (in about 45 sec.), under vortexing, into a glass vial containing 1.5 mL assay buffer, using a pipette fitted with a narrow orifice gel-loading tip. The liposome mixture (50 µL) was added to each well of the 96-well plate in which the enzymes were to be tested. Then, PLAAT protein solutions (50 µL) were transferred from the white 96-well plate to the black microplate wells containing the liposome mixture at 37 °C. The fluorescence measurement was started immediately, every 20 seconds in 60 minutes on a Tecan GENios with a gain of about 54 and an excitation filter at 488 nm and emission filter at 530/590 nm.

In-silico mutagenesis. L2(B6) loops were swapped between PLAAT3 and PLAAT4 by mutating the wild type NMR structures with Chimera ⁵ and selecting the most favourable conformation for each mutated residue. Clashes were removed during energy minimisation in Gromacs ⁶.

MD simulations. MD simulations were performed using Gromacs-5.1.⁶⁷ The NMR structure of PLAAT3 (2KYT) ², PLAAT4 (2MY9) ¹ and the corresponding derived structures from *in-silico* mutagenesis were taken as starting structures and to create topology files. The AMBER ff99sb-ILDN force-field provided with GROMACS was used.⁸ The models were then solvated in a periodic water box of 1 nm and 2 nm cubic edge length for PLAAT3 and PLAAT4, respectively. The latter is larger due to the elongated conformation of the protein. The TIP3Pwater model was used.^{9,10} Three Na⁺ counter ions were automatically placed by the GROMACS program throughout the water box such that the final system had net zero charge. After solvation and neutralization, the systems were energy minimized by 5000 steps of minimization using the steepest descent algorithm. Minimized systems were further equilibrated under NVT and NPT conditions for 500 ps with a step size of 2 fs using position restraints on the protein and a temperature of 300 K and 1 atm. pressure, controlled by the velocity rescaling (modified Berendsen) thermostat ¹¹ and Parrinello-Rahman barostat.¹² The equilibrated systems were subjected to a 100 ns simulation run under NPT without any position restraints, and coordinates were saved after every ps. Two simulations were carried out with different starting seeds, where each seed represents a simulation at a different velocity. The trajectories were analysed using the inbuilt modules available in the GROMACS suite and visualized by means of the VMD¹³/Chimera⁵ program.

Salt-bridge analysis. Salt bridge populations were calculated using VMD¹³ by sampling a structure every 10 ps. The data were extracted and analysed using an in-house written python program. Only residue-pairs with salt bridges having populations of 20% or more, averaged over both runs, were taken into consideration.

References

- (1) Wei, H., Wang, L., Ren, X., Yu, W., Lin, J., Jin, C., and Xia, B. (2015) Structural and functional characterization of tumor suppressors TIG3 and H-REV107. *FEBS Lett.* 589, 1179–1186.
- (2) Ren, X., Lin, J., Jin, C., and Xia, B. (2010) Solution structure of the N-terminal catalytic domain of human H-REV107--a novel circularly permuted NlpC/P60 domain. *FEBS Lett.* 584, 4222–4226.
- (3) Golczak, M., Kiser, P. D., Sears, A. E., Lodowski, D. T., Blaner, W. S., and Palczewski, K. (2012) Structural basis for the acyltransferase activity of lecithin:retinol acyltransferase-like proteins. *J. Biol. Chem.* 287, 23790–23807.
- (4) Heydenreich, F. M., Miljuš, T., Jaussi, R., Benoit, R., Milić, D., and Veprintsev, D. B. (2017) High-throughput mutagenesis using a two-fragment PCR approach. *Sci. Rep.* 7, 6787.
- (5) Pettersen, E. F., Goddard, T. D., Huang, C. C., Couch, G. S., Greenblatt, D. M., Meng, E. C., and Ferrin, T. E. (2004) UCSF Chimera—A visualization system for exploratory research and analysis. *J. Comput. Chem.* 25, 1605–1612.
- (6) Van Der Spoel, D., Lindahl, E., Hess, B., Groenhof, G., Mark, A. E., and Berendsen, H. J. C. (2005) GROMACS: Fast, flexible, and free. *J. Comput. Chem.* 26, 1701–1718.
- (7) Hess, B., Kutzner, C., van der Spoel, D., and Lindahl, E. (2008) GROMACS 4: algorithms for highly efficient, load-balanced, and scalable molecular simulation. *J. Chem. Theory Comput.* 4, 435–447.
- (8) Lindorff-Larsen, K., Piana, S., Palmo, K., Maragakis, P., Klepeis, J. L., Dror, R. O., and Shaw, D. E. (2010) Improved side-chain torsion potentials for the Amber ff99SB protein force field. *Proteins* 78, 1950–1958.
- (9) Jorgensen, W. L. (1981) Quantum and statistical mechanical studies of liquids. 10. Transferable intermolecular potential functions for water, alcohols, and ethers. Application to liquid water. *J. Am. Chem. Soc.* 103, 335–340.
- (10) Mark, P., and Nilsson, L. (2001) Structure and dynamics of the TIP3P, SPC, and SPC/E water models at 298 K. *J. Phys. Chem. A* 105, 9954–9960.
- (11) Bussi, G., Donadio, D., and Parrinello, M. (2007) Canonical sampling through velocity rescaling. *J. Chem. Phys.* 126, 14101.
- (12) Parrinello, M., and Rahman, A. (1981) Polymorphic transitions in single crystals: A new molecular dynamics method. *J. Appl. Phys.* 52, 7182–7190.
- (13) Humphrey, W., Dalke, A., and Schulten, K. (1996) VMD: Visual molecular dynamics. *J.*

Mol. Graph. 14, 33–38.

5

Chapter

Removal of slow-pulsing artifacts in in-phase ^{15}N relaxation dispersion experiments using broadband ^1H decoupling

The work in this chapter was published as: Chatterjee, S. D., Ubbink, M., and van Ingen, H. (2018) Removal of slow-pulsing artifacts in in-phase ^{15}N relaxation dispersion experiments using broadband ^1H decoupling. *J. Biomol. NMR* 71, 69–77.

Abstract

Understanding of the molecular mechanisms of protein function requires detailed insight into the conformational landscape accessible to the protein. Conformational changes can be crucial for biological processes, such as ligand binding, protein folding, and catalysis. NMR spectroscopy is exquisitely sensitive to such dynamic changes in protein conformations. In particular, Carr–Purcell–Meiboom–Gill (CPMG) relaxation dispersion experiments are a powerful tool to investigate protein dynamics on a millisecond time scale. CPMG experiments that probe the chemical shift modulation of ^{15}N in-phase magnetization are particularly attractive, due to their high sensitivity. These experiments require high power ^1H decoupling during the CPMG period to keep the ^{15}N magnetization in-phase. Recently, an improved version of the in-phase ^{15}N -CPMG experiment was introduced, offering greater ease of use by employing a single ^1H decoupling power for all CPMG pulsing rates. In these experiments however, incomplete decoupling of off-resonance amide ^1H spins introduces an artefactual dispersion of relaxation rates, the so-called slow-pulsing artifact. Here, we analyze the slow-pulsing artifact in detail and demonstrate that it can be suppressed through the use of composite pulse decoupling (CPD). We report the performances of various CPD schemes and show that CPD decoupling based on the $90_x-240_y-90_x$ element results in high-quality dispersion curves free of artifacts, even for amides with high ^1H offset.

Introduction

Biological macromolecules such as nucleic acids and proteins are non-rigid entities that can populate a variety of conformers in their energy landscape^{1–3}. The lowest energy conformation,

the ground state, is often able to transiently access higher-energy conformations. Even when their population is low (< 10%) and life times is short (~ ms), these excited states can be crucial for biologically important processes such as enzyme catalysis^{4–8}, ligand binding or protein-protein interaction^{9–14}, and protein folding^{15–20}. While these states cannot be detected directly due to their transient and lowly populated nature, NMR experiments^{21–23} are uniquely able to provide a detailed, atomistic description of the energy landscape. In particular, relaxation dispersion and chemical exchange saturation transfer experiments are particularly powerful herein, as they give access to the population, life times and structures of excited states^{24–31}.

In Carr–Purcell–Meiboom–Gill (CPMG) relaxation dispersion experiments, the characterization of the minor state is derived from the major state peaks by measurement of their effective transverse relaxation rate $R_{2,eff}$, as a function of the pulsing rate in the CPMG period. Signals of nuclear spins that experience exchange between states with different chemical shifts are affected by exchange-induced line broadening, an effect that depends on the free precession interval ($2\tau_{cp}$) between the refocusing pulses in the CPMG element^{24,27}. Analysis of the resulting relaxation dispersion curve, a plot of the $R_{2,eff}$ versus CPMG frequency ($1/4\tau_{cp}$), allows determination of the rate of exchange (k_{ex}), population of minor state (p_b) and the absolute chemical shift difference ($|\Delta\omega|$) between the exchanging states. Importantly, since the shape of the dispersion profile depends on $\Delta\omega$, data is typically acquired at two fields to accurately determine the exchange parameters²⁷.

The ^{15}N backbone amide spin is the most popular nucleus for CPMG RD experiments, due to the simplicity of isotope-labeling, the straightforwardness of the two-spin ^1H – ^{15}N spin system, and the high sensitivity and resolution afforded by these experiments. A critical aspect of these experiments is appropriate handling of differences in the intrinsic R_2 of the in-phase ($N_{x,y}$) and anti-phase ($2N_{x,y}H_z$) ^{15}N magnetization which are generated in the free evolution periods. Anti-phase terms have higher intrinsic relaxation rates due to a contribution of ^1H spin flips to their decay. The original implementation of the ^{15}N CPMG RD experiment uses a relaxation-compensation scheme to average the $N_{x,y}$ and $2N_{x,y}H_z$ relaxation rates³². The ^{15}N CPMG sequence of Hansen *et al.*³³ (CW–CPMG) measures the dispersion profile of pure in-phase $N_{x,y}$ by applying high-power

continuous wave (CW) ^1H decoupling during the CPMG train, offering enhanced sensitivity for non-deuterated proteins³³. Recently, Jiang *et al.*³⁴ modified this sequence (ST–CW–CPMG) to use a single CPMG train with the Yip and Zuiderweg phase cycle (2004) and a single CW decoupling power, yielding dispersion curves free of off-resonance artifacts for a wider range of ^{15}N offset frequencies³⁵.

Both CW–CPMG sequences are nevertheless sensitive to artifacts from ^1H off-resonance effects^{33,35}. Amide ^1H spins that are far off-resonance from the CW decoupling field are not fully decoupled from the ^{15}N spin, resulting in generation of $2N_{x,y}H_z$ magnetization through the residual J -coupling. Consequently, higher $R_{2,eff}$ values will be measured for low ν_{CPMG} values, for which free precession periods are long and more of the antiphase terms will be generated. This so-called slow-pulsing artifact shows up as an artefactual dispersion curve, interfering with accurate extraction of minor-state parameters.

Here, we analyze the slow-pulsing artifact in ^{15}N CW–CPMG sequences in detail and demonstrate a simple method for its removal. In that, we took inspiration from the work of Chakrabarti *et al.*³⁶, where composite pulse decoupling (CPD) was used to suppress ^1H off-resonance effects in exchange mediated saturation transfer experiments. We investigated the performance of various CPD schemes in CW–CPMG sequences and demonstrate here that high power CPD based on the $90_x-240_y-90_x$ element achieves artifact-free dispersion curves over a wide range of ^1H offsets.

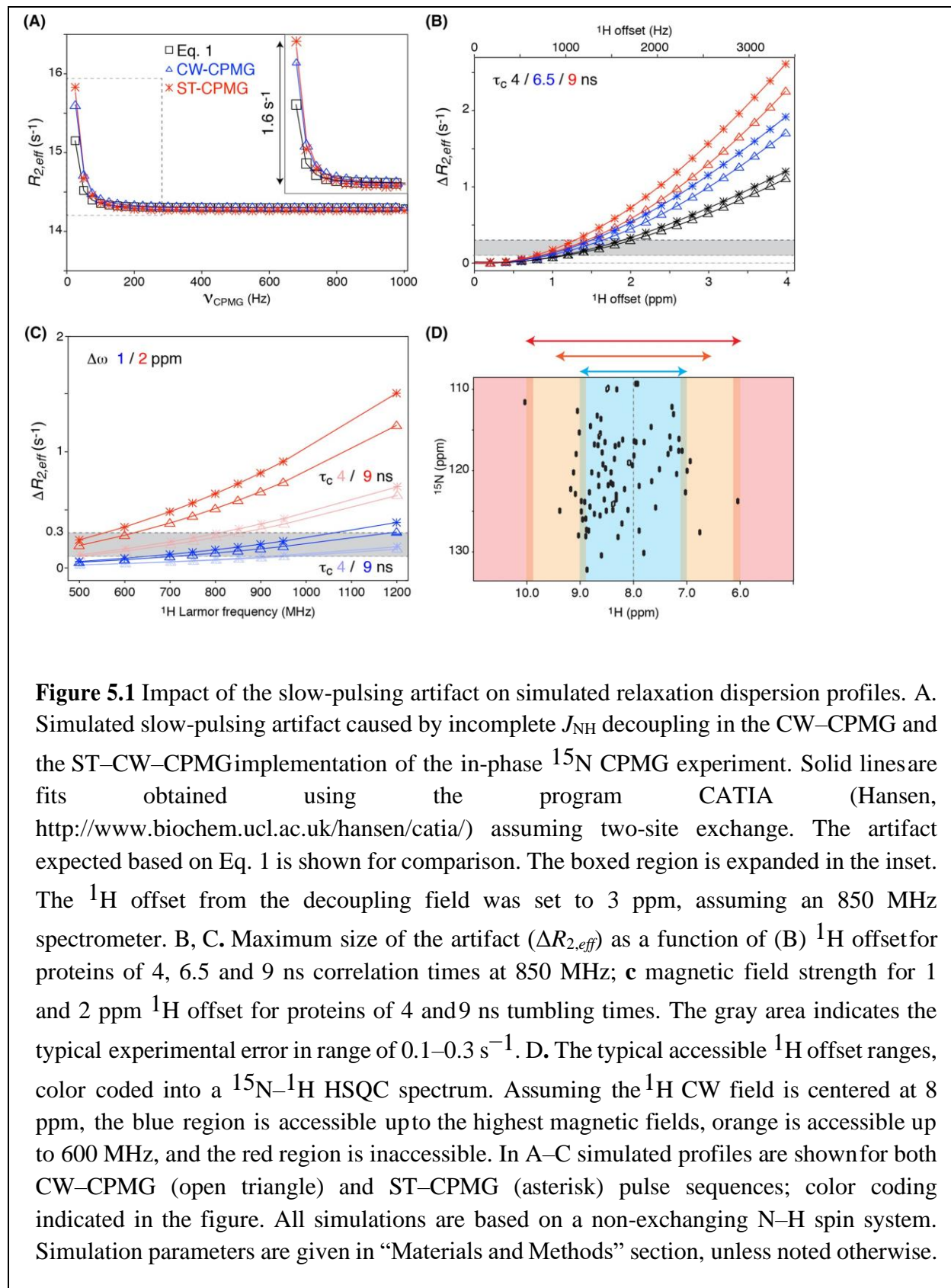
Results

Measurement of in-phase ^{15}N CPMG relaxation dispersion profiles critically relies on H decoupling to measure the pure in-phase $N_{x,y}$ relaxation rate without contamination by the anti-phase relaxation rate. As pointed out in the work of Jiang *et al.*³⁴, the decoupling field strength has a practical limit of roughly 14 kHz, resulting in a residual J coupling interaction for amide protons at non-zero offset to the decoupling field. This interaction causes slow interconversion of in-phase and anti-phase magnetization during the CPMG period, which will lead to undesired averaging of the in-phase and anti-phase relaxation rates^{32,33}. To first approximation, this averaging can be described by the equation derived by Palmer *et al.*⁴² for calculating the effective relaxation rate in spin echo sequences. Here, it is adapted and reformulated to express to the size of the slow-pulsing artifact A :

$$A = \frac{1}{2} (R_2^{anti} - R_2^{in}) (1 - \text{sinc} \pi J_r 2\tau_{cp}) \quad (1)$$

where R_2^{in} and R_2^{anti} are the ^{15}N in-phase and anti-phase transverse relaxation rates, J_r is the residual J -coupling, and $2\tau_{cp}$ is the inter-pulse delay in the CPMG pulse train. In the limit of perfect decoupling $J_r \approx 0$, the sinc factor approaches 1 and $A \approx 0$ for all τ_{cp} values. For non-zero J_r , A approaches zero in the limit of fast pulsing where τ_{cp} is very small. For slow pulsing, however, there is a non-zero artifact, with a theoretical limit of 0.5 ($R_{2,anti} - R_{2,in}$) for infinitely slow pulsing. In practice, J_r can be as much 16 Hz (for 3 ppm ^1H offset at 850 MHz) and $2\tau_{cp}$ is typically at most 20 ms, which would generate a maximum artifact of roughly 10% of the difference between the anti-phase and in-phase relaxation rate.

To assess more precisely how the slow pulsing artifact is manifested in ^{15}N CPMG–CW and ST–CW experiments, numerical simulations of these sequences were performed in Liouville space for a non-exchanging two spin N–H system. Figure 5.1A compares the obtained dispersion profiles for the two experiments with the predicted curve based on Eq. 1, for a N–H system with 3 ppm ^1H offset at an 850 MHz spectrometer. Whereas a flat curve is expected for a non-exchanging system, systematically increased $R_{2,eff}$ values are measured in the slow pulsing regime for both pulse sequences. While Eq. 1 is derived for periods of free evolution in absence of a decoupling field, the curvature of the slow-pulsing artifact matches the predicted sinc dependence on the pulsing rate.



The size of the artifact is somewhat underestimated by Eq. 1. The original CW sequence shows slightly lower sensitivity to the artifact than the ST–CW experiment. This difference can be traced back to presence of the ^{15}N refocusing pulse in between the two halves of the total CPMG period in the CW experiment. Importantly, since the shape of the artifact is virtually indistinguishable from a *bona-fide* dispersion profile, the artefactual $R_{2,eff}$ values can be fitted to an actual dispersion curve (see solid lines in Figure 5.1A), illustrating the potential impact on the extracted exchange parameters.

Since the size of the slow pulsing artifact is governed by the relaxation difference between in-phase and anti-phase magnetization, it is dependent on protein size. Large proteins have more efficient ^1H – ^1H spin flips which increase the anti-phase relaxation rate. Figure 5.1B compares the magnitude of the artifact for three different protein sizes as function of ^1H offset from the decoupling field. For larger proteins, where the chance of finding amide protons at high offset is also higher, the artifact can be well above 1 s^{-1} . At offsets larger than $\sim 1000\text{ Hz}$ the slow pulsing artifact will be higher than the typical experimental error (on the order of $0.1\text{--}0.3\text{ s}^{-1}$)⁴³, as also noted by Jiang *et al.*³⁴.

Since relaxation dispersion data need to be acquired at two magnetic fields in order to extract accurate protein dynamics parameters, we compared the size of the slow pulsing artifact for amide groups at 1 and 2 ppm ^1H offset as function of magnetic field strength in Figure 5.1C. High field strengths are not only attractive because of the sensitivity and resolution they afford, but also because they are more sensitive to exchange processes as they increase the frequency difference between states, $\Delta\omega$. However, for a given resonance, the offset from the decoupling field, and thus the slow pulsing artifact, will increase with increasing magnetic field strength. Strikingly, the artifact will already be significant at 1 ppm offsets for medium-sized proteins in a future 1.2 GHz spectrometer. To illustrate the impact of the slow pulsing artifact, generated by the inability of CW irradiation to decouple the full width of the amide spectrum, the HSQC can be divided in three areas: a narrow region $\pm \sim 1\text{ ppm}$ around the carrier frequency of the decoupling field that will be free of significant artifacts, the region beyond $\pm \sim 2\text{ ppm}$ in which significant artifacts will

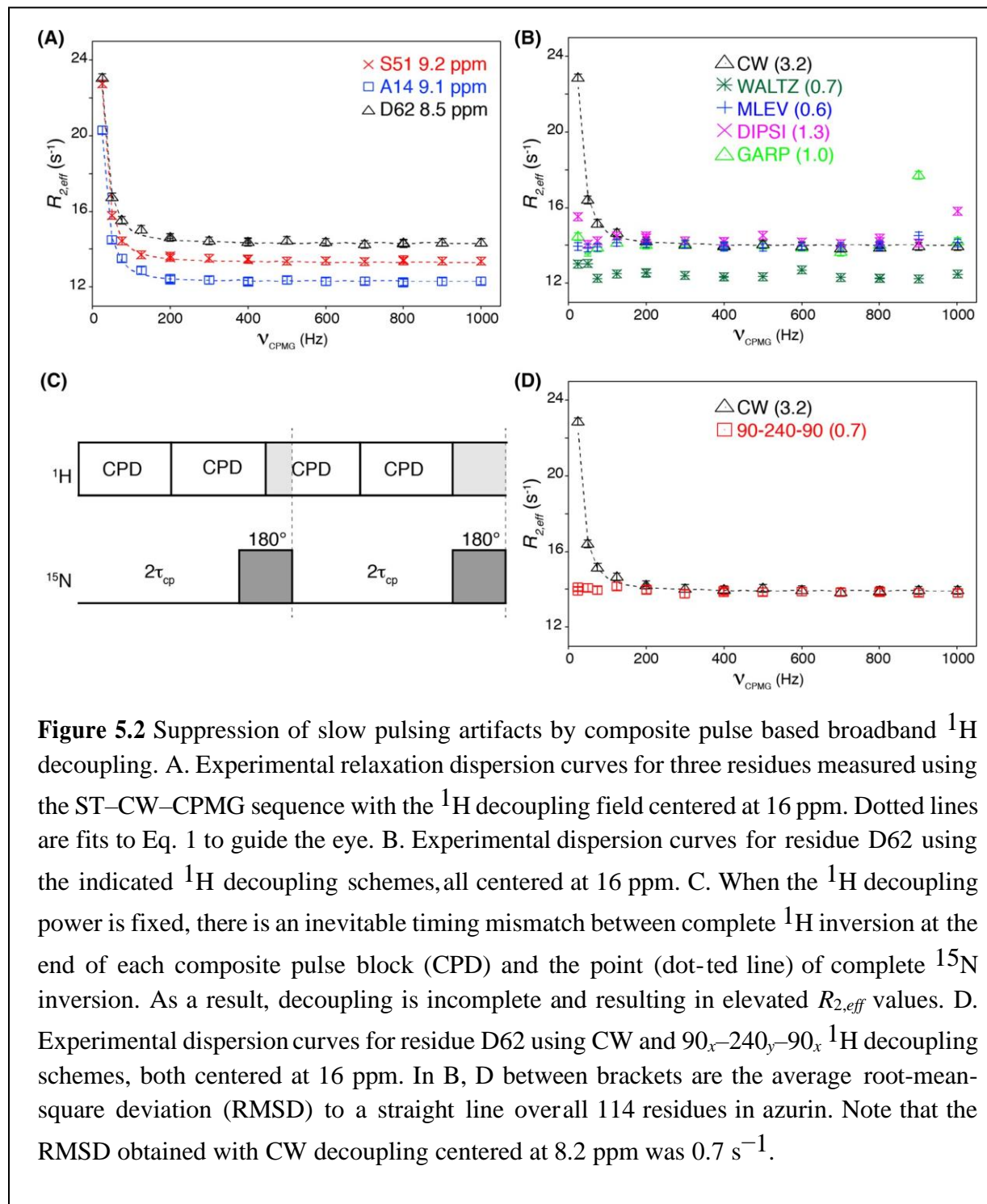
already occur at the lowest typical field strength, and the intermediate region (Figure 5.1D). To confirm the results obtained from simulations, we experimentally demonstrated the problem using the ST–CW–CPMG pulse sequence on a sample containing azurin, a 16 kDa electron transfer metalloprotein⁴⁴. A small subset of residues in azurin have been reported to undergo conformational exchange on the millisecond timescale⁴⁵. To emphasize the slow pulsing artifact, we purposely centered the ¹H decoupling field at 16 ppm such that the dispersion profiles are dominated by the artifact (Figure 5.2A). Using this setup, we next screened several broadband decoupling sequences for their ability to suppress the artifact. These sequences rely on composite pulses to offer good population inversion even in the presence of off-resonance effects⁴⁶, and thus should be able to suppress the artifact in theory. As can be seen in Figure 5.2B, a wide range of CPD schemes indeed suppressed the artifact. Notably, the use of GARP⁴⁷ and DIPS12⁴⁸ results in spurious elevated $R_{2,eff}$ values at high pulsing rates, rendering the dispersion curves unusable. These spikes originate from the timing mismatch between the continuous train of (composite) 180° pulses on the ¹H channel on the one hand and the repetition of free-evolution and 180° refocusing pulses on the ¹⁵N channel on the other hand. This mismatch results in incomplete decoupling at the end of each τ_{cp} period and thus elevated $R_{2,eff}$ values (Figure 5.2C). As noted by Jiang *et al.*³⁴, the duration of the mismatch is short when using adequately high power CW ¹H decoupling, and thus the effect is small. Both DIPS12 and GARP use particularly long composite pulses (corresponding to the length of 2590° and 1054° rotation, respectively), which aggravates the impact of the timing mismatch, in particular at high pulsing rates, where the effects from each τ_{cp} period are compounded. Indeed, use of WALTZ (540° duration)⁴⁹ and MLEV (360° duration)^{50–52} with shorter duration of the composite pulse did not cause such high spikes. We next applied the 90_x–240_y–90_x CPD scheme, which was recently used to suppress artifacts from incomplete ¹H decoupling in exchange mediated saturation transfer experiments³⁶. The 90_x–240_y–90_x CPD sequence has a short overall duration (420° rotation) and offers relatively broadband inversion, free from off-resonance effects without relying on supercycles^{52,53}. Gratifyingly, the 90_x–240_y–90_x sequence effectively eliminated the artifacts without causing appreciable spikes or scatter in $R_{2,eff}$ values (Figure 5.2D). The requirement for a short duration of the CPD element also means that the broadband performance of CPD decoupling cannot be used to reduce the decoupling power. Tests showed that reducing the decoupling power to 7 kHz (34 μs decoupling pulse) resulted

in spurious artifacts dominating the dispersion curves at high CPMG pulsing rates (data not shown).

While successful in suppressing the slow-pulsing artifacts, the use of composite pulse sequences for decoupling results in systematic differences in $R_{2,eff}$ values compared to those obtained using CW decoupling. This is most apparent from the WALTZ data in Figure 5.2B, showing systematically reduced $R_{2,eff}$ values compared to the CW reference data. Such offsets between the CPD-derived and CW-derived dispersion curve are also found for MLEV and $90_x-240_y-90_x$ decoupling, although typically much smaller. When using the $90_x-240_y-90_x$ sequence, the average offset over all residues was found to be $\sim 0.3 \text{ s}^{-1}$ with 90% of the profiles having offsets below 0.6 s^{-1} (see Supplemental Table S5.1). Since this offset is small and the absolute value of $R_{2,eff}$ is not of importance when fitting dispersion curves, it will have negligible impact on the usefulness of the data obtained with CPD decoupling schemes.

Having established that WALTZ, MLEV and $90_x-240_y-90_x$ decoupling sequences are able to suppress the slow pulsing artifact, we further tested their efficacy in a regular experimental setup with the decoupling field centered at 8.2 ppm. The obtained $R_{2,eff}$ values were compared point-by-point between the CPD and the CW data-set, and the root-mean-square deviation (RMSD) between data sets was calculated with and without compensating for the systematic offset in $R_{2,eff}$ values between the two datasets (Figure 5.3A). Clearly, the $90_x-240_y-90_x$ sequence performs best with an average RMSD to the reference CW data set of 0.17 s^{-1} , which is on the order of the experimental error. The high quality of the data is visible from comparison of profiles obtained for residues with negligible ^1H offset, such as shown in Figure 5.3B. At high ^1H offset from the decoupling field, the CW data suffers from the slow pulsing artifact, which is absent when using the $90_x-240_y-90_x$ CPD sequence, as exemplified for T52 in Figure 5.3C. Notably, this residue shows the slow pulsing artifact superimposed on a genuine dispersion of $R_{2,eff}$ values. From the comparison to the CPD-based experiment, it becomes clear that the data point at 25 Hz ν_{CPMG} pulsing rate is strongly affected by the slow pulsing artifact with $R_{2,eff}$ value spuriously elevated by $\sim 1 \text{ s}^{-1}$. As a final experiment, we recorded both CW and CPD-based dispersion profiles at the national ultra-high field NMR Facility at 950 MHz. At this field, the resonance with the

highest ^1H offset shows a slow-pulsing artifact of $\sim 1.5 \text{ s}^{-1}$ in the CW experiment, which is effectively suppressed when using the $90_x-240_y-90_x$ decoupling sequence (Figure 5.3D).



Discussion

We have investigated the impact of the slow-pulsing artifact in in-phase ^{15}N relaxation dispersion experiments by theoretical considerations, numerical simulations and experiments. We show that the artifact can be removed by using CPD-based ^1H decoupling during the CPMG period. Out of the tested CPD sequences, the $90_x-240_y-90_x$ sequence offers the best performance: the artifact is fully suppressed, while retaining shape of the dispersion curve obtained using CW decoupling within experimental error. Notably, this is done without introducing spurious spikes in $R_{2,\text{eff}}$ values at high pulsing rates, and with minimal offset to the CW-based dispersion profiles. Critical to its performance seems to be short duration of the composite pulse combined with relatively high quality of off-resonance performance.

The cause of the slight offset between the CPD and CW- based dispersion profiles is unclear. Closer inspection shows that the magnitude of the offset shows no correlation to either the N , H_N , or H_α chemical shift and that both reference (no CPMG delay) and dispersion experiment (with CPMG delay) have slightly altered intensities ($\sim 2-5\%$) in the CPD experiment compared to the CW experiment. The effect on the reference experiment, where the decoupling block is carried out before the recycle delay, signifies that the both types of decoupling result in a different steady-state magnetization, presumably both for water and protein protons.

As for the water magnetization, a disadvantage of using CPD over CW decoupling is the loss of control over its state. Whereas in the CW case the water magnetization is spin-locked and returned to $+z$ after the CPMG period, continuous alteration between x and y -pulse phase during the $90_x-240_y-90_x$ CPD element causes dephasing and loss of water polarization. Experimental tests Hiller *et al.*⁵⁴ demonstrate this effect and show that after a 2 s delay, corresponding to the recycle delay to the next proton excitation pulse, there is minimal difference between the water polarization in the CPD and CW case (see Supplemental Figure S5.1). Here, radiation damping caused by the high Q of the cryogenic probe likely aids the recovery of the water magnetization in the CPD case. Additionally, the low pH of the sample (5.5) will slow down amide-water exchange and thus additionally dampen the effect of (residual) water saturation.

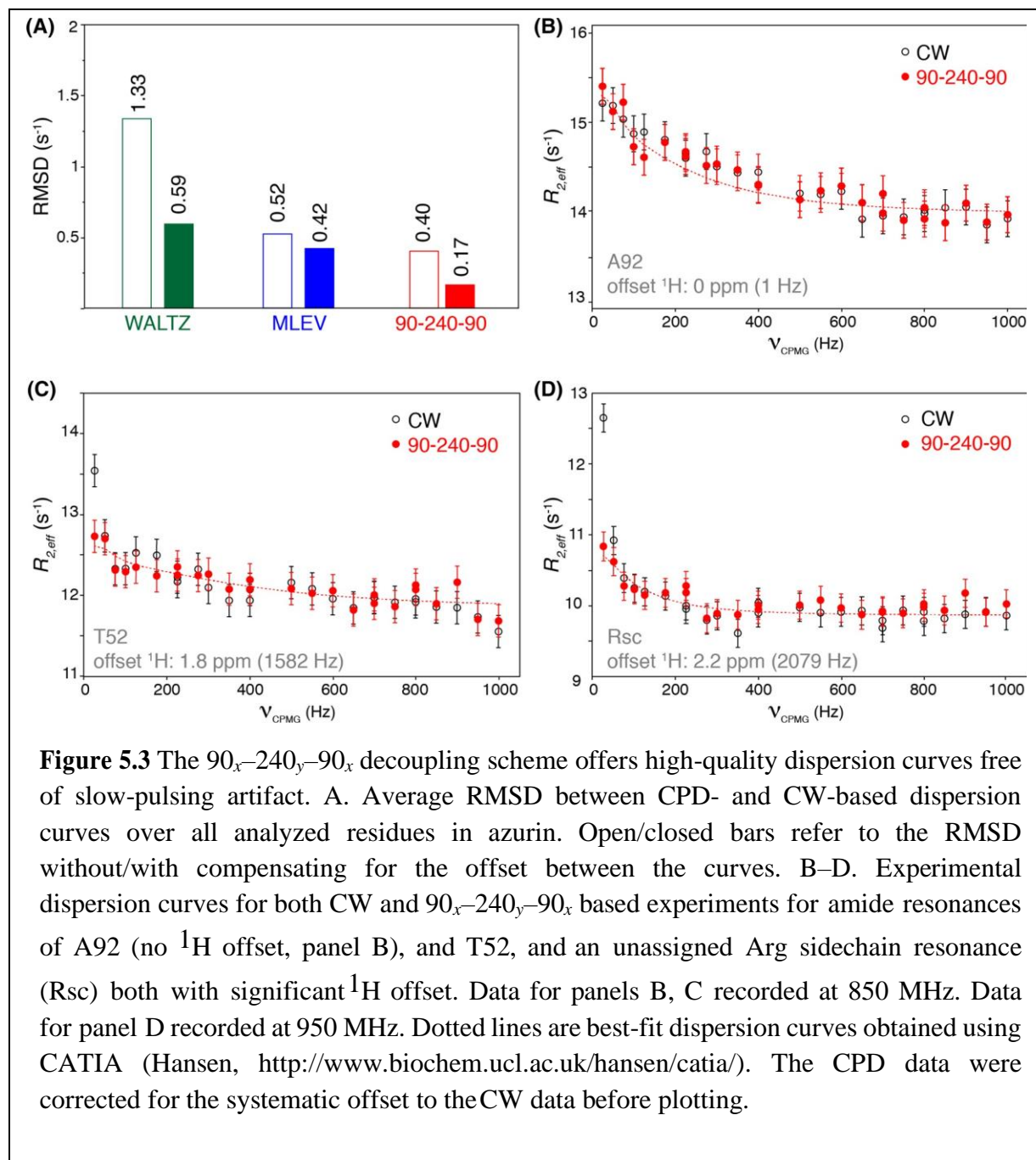


Figure 5.3 The $90_x-240_y-90_x$ decoupling scheme offers high-quality dispersion curves free of slow-pulsing artifact. A. Average RMSD between CPD- and CW-based dispersion curves over all analyzed residues in azurin. Open/closed bars refer to the RMSD without/with compensating for the offset between the curves. B–D. Experimental dispersion curves for both CW and $90_x-240_y-90_x$ based experiments for amide resonances of A92 (no ¹H offset, panel B), and T52, and an unassigned Arg sidechain resonance (Rsc) both with significant ¹H offset. Data for panels B, C recorded at 850 MHz. Data for panel D recorded at 950 MHz. Dotted lines are best-fit dispersion curves obtained using CATIA (Hansen, <http://www.biochem.ucl.ac.uk/hansen/catia/>). The CPD data were corrected for the systematic offset to the CW data before plotting.

In the original implementation of the in-phase dispersion experiment described by Hansen *et al.*³³, the strength of the decoupling field is matched to the CPMG pulsing rate to avoid the timing mismatch as indicated in Figure 5.2C. In principle, such matching could also be done when using CPD decoupling schemes, which should result in decreased scatter in the dispersion curves. While simulations indeed show such improvement in performance, an experimental test showed a severe increase in scatter, presumably due to a point-to-point variation in the steady state of the

water and aliphatic proton magnetization.

As noted in Figure 5.1, the slow-pulsing artifact will be particularly problematic at high magnetic field strengths. At such high fields, it may be better to use TROSY–CPMG sequences⁵⁵, which do not suffer from the slow-pulsing artifact, even for non-deuterated moderately sized proteins. The relative sensitivity of TROSY and in-phase CPMG experiments is best assessed experimentally as it not only depends on magnetic field strength but also on protein size, labeling pattern, and temperature. Next to the absolute sensitivity, one may also consider that lower ¹⁵N relaxation rates during the CPMG period allow the use of longer CPMG delays, increasing the sensitivity to slow motions⁵⁵, as well as spectral quality of TROSY spectra (reduced overlap vs. presence of anti-TROSY lines). Additionally, in case data at lower field strength have been recorded using the in-phase CPMG experiment it may be necessary to record these at high fields too.

In conclusion, we show here that the use of broadband ¹H decoupling, in particular using the 90_x–240_y–90_x sequence, is a viable and attractive option for recording in-phase ¹⁵N relaxation dispersion data. This option is particularly relevant when the protein spectrum contains resonances far from center. It offers artifact-free dispersion profiles without the need for recording data in multiple sets or the need for eliminating of data points, all without compromising data quality.

Materials and methods

NMR samples. NMR experiments were recorded on a sample of 2.5 mM uniformly ¹⁵N/¹³C-labelled Cu(II) azurin in 25 mM potassium phosphate buffer at pH 5.49 with 5% D₂O. Labelled azurin was produced and purified according to a previously published protocol with modifications for incorporating ¹³C-glucose and ¹⁵N-ammoniumchloride³⁷.

NMR experiments. Relaxation dispersion experiments, using the ST–CW–CPMG sequence, were recorded at 298 K on Bruker Advance III HD spectrometers operating at 850 and 950 MHz ¹H Larmor frequency and equipped with TCI cryoprobes. The constant-time CPMG relaxation delay (T_{relax}) was set to 40 ms with ν_{CPMG} set to 25, 50, 75, 100, 125, 175, 225 (2×), 275, 300, 350, 400 (2×), 500, 550, 600, 650, 700 (2×), 750, 800 (2×), 850, 900, 950 and 1000 Hz respectively, run

in an interleaved manner. Duplicates were used to estimate the error in $R_{2,eff}$. The errors were set to 0.2 s^{-1} at minimum. The pulse length of the ^{15}N refocusing pulses in the CPMG train was $90 \mu\text{s}$. For ^1H decoupling, either CW decoupling or a CPD-scheme (GARP, DIPSI, MLEV16, WALTZ16, $90_x-240_y-90_x$) was used. This was implemented by changing the “cw:f1” statement in the pulse program to read “cpds1:f1” (pulse program available upon request). In either case, the decoupling field strength was 14.7 kHz ($17 \mu\text{s}$ ^1H 90° pulse), applied at 8.2 ppm ^1H offset. A total of $3072/120$ points were acquired in the $^1\text{H}/^{15}\text{N}$ dimension with an acquisition time of $90/27.85 \text{ ms}$ and a relaxation delay of 2 s and 4 scans per FID. A reference spectrum, without the relaxation delay, was also recorded. NMR data were processed with NMR Pipe³⁸, using linear prediction in the ^{15}N dimension and Lorentz-to-Gauss window functions. Peak volumes were obtained by peak fitting using FuDa (Hansen, <http://www.biochem.ucl.ac.uk/hansen/fuda/>), and subsequently converted into effective relaxation rates via $R_{2,eff}(v_{\text{CPMG}}) = -1/T_{\text{relax}} \cdot \ln(I(v_{\text{CPMG}})/I_0)$, where I_0 is the peak intensity in a reference spectrum recorded without the relaxation delay T_{relax} . The $R_{2,eff}$ values measured using the ST-CW-CPMG sequence were corrected for R_1 -contribution according to the formula described by Jiang *et al.*³⁴ using an estimate of 0.95 s^{-1} R_1 - and 10.5 s^{-1} for R_2 -contribution for all residues. Dispersion curves obtained with either CW or CPD decoupling were compared by calculating the RMSD between the curves for all residues:

$$RMSD = \sqrt{\frac{1}{N} \sum_{i=1}^N \left(R_{2,eff}^{CPD,i} - R_{2,eff}^{CW,i} \right)^2}$$

where i is the index of a particular v_{CPMG} value and the summation runs over the N recorded points, equal to the number of points per dispersion curve (M) times the number of residues. The systematic difference between the CW or CPD-based dispersion curves was calculated from the average point-by-point difference per residue and is tabulated in Table S5.1. To compensate for these systematic differences, an “ R_2 -offset compensated” RMSD was calculated by replacing the CPD-based $R_{2,eff}$ values with the offset compensated values:

$$R_{2,eff}^{CPD,compensated,i} = R_{2,eff}^{CPD,i} - \frac{1}{M} \sum_{i=1}^M \left(R_{2,eff}^{CPD,i} - R_{2,eff}^{CW,i} \right)$$

Simulation of ^{15}N CW–CPMG dispersion profiles. To evaluate the magnitude of the slow-pulsing artifact in relaxation dispersion profiles, numerical simulations of a two-spin ^1H – ^{15}N system were carried out, assuming a non-deuterated protein. The evolution of magnetization in this spin system was calculated for the CPMG part of the CPMG–CW and CPMG–ST–CW sequence, including the flanking ^{15}N 90° pulses. Simulations in the absence of exchange and neglecting pulse imperfections were performed in operator space by solving the complete homogeneous master equation as described by Allard *et al.*³⁹ and Helgstrand *et al.*⁴⁰ using the open source computing language GNU Octave (<http://www.gnu.org/software/octave/>)⁴¹. All simulation used the parameters detailed below unless noted otherwise. The ^{15}N spin was assumed to be on resonance.

The magnetic field strength was set to 19.9 T, corresponding to ^1H Larmor frequency of 850 MHz. Relaxation rates were calculated using overall rotational correlation time τ_c of 9 ns, a value of 0.85 for the squared generalized order parameter, 100 ps for the correlation time for internal motions, and $-172/+10$ ppm for the $^{15}\text{N}/^1\text{H}$ chemical shift anisotropy. Relaxation due to neighboring protons was included as described in ref Allard *et al.*³⁹ by including a virtual proton at 1.85 Å, resulting in R_2 values of in-phase and anti-phase ^{15}N magnetizations of 13.6 and 26.7 s^{-1} respectively. Dispersion experiments were simulated with T_{relax} set to 40 ms, and ν_{CPMG} values ranging from 25 to 1000 Hz, the ^{15}N 180° refocusing pulse was set to 90 μs , ^1H CW decoupling field strength was set to 14.7 kHz (17 μs ^1H 90°).

Supplementary

Table S5.1 $R_{2,\text{eff}}$ offset between CPD and CW-derived dispersion curves^a.

<i>CPD scheme</i>	<i>average (s^{-1})</i>	<i>range (s^{-1})</i>	<i>90% limit (s^{-1})^b</i>
$90_x-240_y-90_x$	-0.27	-1.13 – 0.74	0.57
<i>MLEV</i>	-1.24	-6.77 – 1.06	2.92
<i>WALTZ</i>	-0.85	-4.44 – 1.15	1.80

^a data recorded with offset of decoupling field centered at 8.2 ppm. Negative offset values indicate that CPD-derived $R_{2,\text{eff}}$ values are lower than in the CW-based experiment.

^b absolute values.

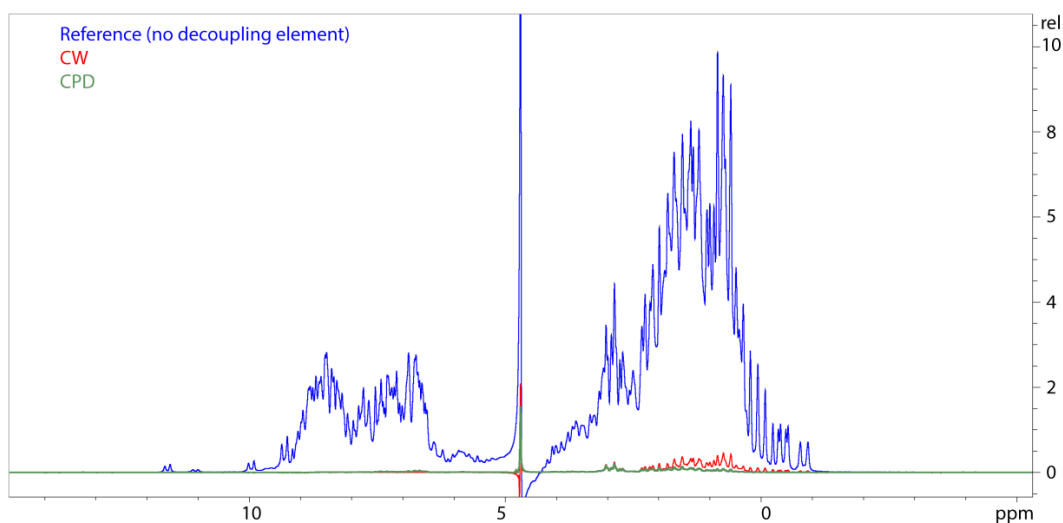


Figure S5.1 1D-¹H NMR spectra of azurin to study the effect on the reference experiment where the decoupling block is placed before the recycle delay. A recycle delay of 40 ms was used for obtaining data for CW and CPD elements while keeping the decoupling offset at 8.2 ppm and the decoupling power set at 3.5 W. The reference spectrum does not contain any decoupling block. Both CW and CPD decouplers suppress the water and aliphatic protons.

References

- (1) Frauenfelder, H., Sligar, S. G., and Wolynes, P. G. (1991) The energy landscapes and motions of proteins. *Science (80-.)*. 254, 1598–1603.
- (2) Wolynes, P. G., Karplus, M., Dobson, C. M., Zewail, A. H., Clarke, J., and Schön, J. C. (2005) Energy landscapes and solved protein-folding problems. *Philos. Trans. R. Soc. A Math. Phys. Eng. Sci.* 363, 453–467.
- (3) Henzler-Wildman, K., and Kern, D. (2007, December) Dynamic personalities of proteins. *Nature*. Nature Publishing Group.
- (4) HAMMES, G. G. (1964) Mechanism of enzyme catalysis. *Nature* 204, 342–343.
- (5) Eisenmesser, E. Z., Millet, O., Labeikovsky, W., Korzhnev, D. M., Wolf-Watz, M., Bosco, D. A., Skalicky, J. J., Kay, L. E., and Kern, D. (2005) Intrinsic dynamics of an enzyme underlies catalysis. *Nature* 438, 117–121.
- (6) Henzler-Wildman, K. A., Thai, V., Lei, M., Ott, M., Wolf-Watz, M., Fenn, T., Pozharski, E., Wilson, M. A., Petsko, G. A., Karplus, M., Hübner, C. G., and Kern, D. (2007) Intrinsic motions along an enzymatic reaction trajectory. *Nature* 450, 838.
- (7) Palmer, A. G. (2015) Enzyme dynamics from NMR spectroscopy. *Acc. Chem. Res.* 48, 457–465.
- (8) Kim, T. H., Mehrabi, P., Ren, Z., Sljoka, A., Ing, C., Bezginov, A., Ye, L., Pomès, R., Prosser, R. S., and Pai, E. F. (2017) The role of dimer asymmetry and protomer dynamics in enzyme catalysis. *Science (80-.)*. 355.
- (9) Sugase, K., Dyson, H. J., and Wright, P. E. (2007) Mechanism of coupled folding and binding of an intrinsically disordered protein. *Nature* 447, 1021.
- (10) Schneider, R., Maurin, D., Communie, G., Kragelj, J., Hansen, D. F., Ruigrok, R. W. H., Jensen, M. R., and Blackledge, M. (2015) Visualizing the molecular recognition trajectory of an intrinsically disordered protein using multinuclear relaxation dispersion NMR. *J. Am. Chem. Soc.* 137, 1220–1229.
- (11) Pratihari, S., Sabo, T. M., Ban, D., Fenwick, R. B., Becker, S., Salvatella, X., Griesinger, C.,

and Lee, D. (2016) Kinetics of the Antibody Recognition Site in the Third IgG-Binding Domain of Protein G. *Angew. Chemie - Int. Ed.* 55, 9567–9570.

(12) Xiao, T., Fan, J., Zhou, H., Lin, Q., and Yang, D. (2016) Local unfolding of fatty acid binding protein to allow ligand entry for binding. *Angew. Chemie Int. Ed.* 55, 6869–6872.

(13) Zhao, B., Guffy, S. L., Williams, B., and Zhang, Q. (2017) An excited state underlies gene regulation of a transcriptional riboswitch. *Nat. Chem. Biol.* 13, 968–974.

(14) Delaforge, E., Kragelj, J., Tengo, L., Palencia, A., Milles, S., Bouvignies, G., Salvi, N., Blackledge, M., and Jensen, M. R. (2018) Deciphering the dynamic interaction profile of an intrinsically disordered protein by NMR exchange spectroscopy. *J. Am. Chem. Soc.* 140, 1148–1158.

(15) Korzhnev, D. M., Religa, T. L., Banachewicz, W., Fersht, A. R., and Kay, L. E. (2010) A transient and low-populated protein-folding intermediate at atomic resolution. *Science (80-)*. 329, 1312 LP – 1316.

(16) Neudecker, P., Robustelli, P., Cavalli, A., Walsh, P., Lundström, P., Zarrine-Afsar, A., Sharpe, S., Vendruscolo, M., and Kay, L. E. (2012) Structure of an intermediate state in protein folding and aggregation. *Science (80-)*. 336, 362 LP – 366.

(17) Kimsey, I. J., Petzold, K., Sathyamoorthy, B., Stein, Z. W., and Al-Hashimi, H. M. (2015) Visualizing transient Watson-Crick-like mispairs in DNA and RNA duplexes. *Nature* 519, 315–320.

(18) Libich, D. S., Tugarinov, V., and Clore, G. M. (2015) Intrinsic unfoldase/foldase activity of the chaperonin GroEL directly demonstrated using multinuclear relaxation-based NMR. *Proc. Natl. Acad. Sci. U. S. A.* 112, 8817–8823.

(19) Franco, R., Gil-Caballero, S., Ayala, I., Favier, A., and Brutscher, B. (2017) Probing conformational exchange dynamics in a short-lived protein folding intermediate by real-time relaxation–dispersion NMR. *J. Am. Chem. Soc.* 139, 1065–1068.

(20) Culik, R. M., Sekhar, A., Nagesh, J., Deol, H., Rumfeldt, J. A. O., Meiering, E. M., and Kay, L. E. (2018) Effects of maturation on the conformational free-energy landscape of SOD1. *Proc. Natl. Acad. Sci. U. S. A.* 115, E2546–E2555.

- (21) Akke, M., and Palmer, A. G. (1996) Monitoring macromolecular motions on microsecond to millisecond time scales by $R_{1\rho}$ - R_1 constant relaxation time NMR spectroscopy. *J. Am. Chem. Soc.* *118*, 911–912.
- (22) Fawzi, N. L., Ying, J., Torchia, D. A., and Clore, G. M. (2010) Kinetics of amyloid β monomer-to-oligomer exchange by NMR relaxation. *J. Am. Chem. Soc.* *132*, 9948–9951.
- (23) Kovermann, M., Rogne, P., and Wolf-Watz, M. (2016) Protein dynamics and function from solution state NMR spectroscopy. *Q. Rev. Biophys.* *49*, e6.
- (24) Palmer, A. G., Kroenke, C. D., and Loria, J. P. (2001) Nuclear magnetic resonance methods for quantifying microsecond-to-millisecond motions in biological macromolecules, in *Methods in Enzymology*, pp 204–238. Academic Press Inc.
- (25) Vallurupalli, P., Bouvignies, G., and Kay, L. E. (2012) Studying “invisible” excited protein states in slow exchange with a major state conformation. *J. Am. Chem. Soc.* *134*, 8148–8161.
- (26) Vallurupalli, P., Sekhar, A., Yuwen, T., and Kay, L. E. (2017) Probing conformational dynamics in biomolecules via chemical exchange saturation transfer: a primer. *J. Biomol. NMR* *67*, 243–271.
- (27) Sauerwein, A. C., and Flemming Hansen, D. (2015) Relaxation dispersion NMR spectroscopy, in *Protein NMR: Modern Techniques and Biomedical Applications*, pp 75–132. Springer International Publishing.
- (28) Xue, Y., Kellogg, D., Kimsey, I. J., Sathyamoorthy, B., Stein, Z. W., McBairty, M., and Al-Hashimi, H. M. (2015) Characterizing RNA excited states using NMR relaxation dispersion, in *Methods in Enzymology*, pp 39–73. Academic Press Inc.
- (29) Lisi, G. P., and Loria, J. P. (2016, February) Using NMR spectroscopy to elucidate the role of molecular motions in enzyme function. *Prog. Nucl. Magn. Reson. Spectrosc.* Elsevier B.V.
- (30) Massi, F., and Peng, J. W. (2018) Characterizing protein dynamics with NMR $R_{1\rho}$ relaxation experiments, in *Methods in Molecular Biology*, pp 205–221. Humana Press Inc.
- (31) Gopalan, A. B., Hansen, D. F., and Vallurupalli, P. (2018) CPMG experiments for protein minor conformer structure determination, in *Methods in Molecular Biology*, pp 223–242.

Humana Press Inc.

- (32) Loria, J. P., Rance, M., and Palmer, A. G. (1999, March) A relaxation-compensated Carr-Purcell-Meiboom-Gill sequence for characterizing chemical exchange by NMR spectroscopy [13]. *J. Am. Chem. Soc.* American Chemical Society .
- (33) Hansen, D. F., Vallurupalli, P., and Kay, L. E. (2008) An improved ^{15}N relaxation dispersion experiment for the measurement of millisecond time-scale dynamics in proteins. *J. Phys. Chem. B* 112, 5898–5904.
- (34) Jiang, B., Yu, B., Zhang, X., Liu, M., and Yang, D. (2015) A ^{15}N CPMG relaxation dispersion experiment more resistant to resonance offset and pulse imperfection. *J. Magn. Reson.* 257, 1–7.
- (35) Yip, G. N. B., and Zuiderweg, E. R. P. (2004) A phase cycle scheme that significantly suppresses offset-dependent artifacts in the R2-CPMG ^{15}N relaxation experiment. *J. Magn. Reson.* 171, 25–36.
- (36) Chakrabarti, K. S., Ban, D., Pratihar, S., Reddy, J. G., Becker, S., Griesinger, C., and Lee, D. (2016) High-power ^1H composite pulse decoupling provides artifact free exchange-mediated saturation transfer (EST) experiments. *J. Magn. Reson.* 269, 65–69.
- (37) Karlsson, B. G., Pascher, T., Nordling, M., Arvidsson, R. H. A., and Lundberg, L. G. (1989) Expression of the blue copper protein azurin from *Pseudomonas aeruginosa* in *Escherichia coli*. *FEBS Lett.* 246, 211–217.
- (38) Delaglio, F., Grzesiek, S., Vuister, G. W., Zhu, G., Pfeifer, J., and Bax, A. (1995) NMRPipe: A multidimensional spectral processing system based on UNIX pipes. *J. Biomol. NMR* 6, 277–293.
- (39) Allard, P., Helgstrand, M., and Härd, T. (1998) The Complete Homogeneous Master Equation for a Heteronuclear Two-Spin System in the Basis of Cartesian Product Operators. *J. Magn. Reson.* 134, 7–16.
- (40) Helgstrand, M., Hard, T., and Allard, P. (2000) Simulations of NMR pulse sequences during equilibrium and non-equilibrium chemical exchange. *J. Biomol. NMR* 18, 49–63.

- (41) GNU Octave Manual Version 3 | Perceiving Systems - Max Planck Institute for Intelligent Systems.
- (42) Palmer, A. G., Skelton, N. J., Chazin, W. J., Wright, P. E., and Rance, M. (1992) Suppression of the effects of cross-correlation between dipolar and anisotropic chemical shift relaxation mechanisms in the measurement of spin-spin relaxation rates. *Mol. Phys.* 75, 699–711.
- (43) Hansen, D. F., Vallurupalli, P., Lundström, P., Neudecker, P., and Kay, L. E. (2008) Probing chemical shifts of invisible states of proteins with relaxation dispersion NMR spectroscopy: how well can we do? *J. Am. Chem. Soc.* 130, 2667–2675.
- (44) Adman, E. T. (1991, January) Copper protein structures. *Adv. Protein Chem.* Academic Press Inc.
- (45) Korzhnev, D. M. (2003) NMR detection of multiple transitions to low-populated states in azurin. *Protein Sci.* 12, 56–65.
- (46) Shaka, A. J., and Keeler, J. (1987, January) Broadband spin decoupling in isotropic-liquids. *Prog. Nucl. Magn. Reson. Spectrosc.* Pergamon.
- (47) Shaka, A. J., Barker, P. B., and Freeman, R. (1985) Computer-optimized decoupling scheme for wideband applications and low-level operation. *J. Magn. Reson.* 64, 547–552.
- (48) Shaka, A. J., Lee, C. J., and Pines, A. (1988) Iterative schemes for bilinear operators; application to spin decoupling. *J. Magn. Reson.* 77, 274–293.
- (49) Shaka, A. J., Keeler, J., Frenkiel, T., and Freeman, R. (1983) An improved sequence for broadband decoupling: WALTZ-16. *J. Magn. Reson.* 52, 335–338.
- (50) Levitt, M. H., and Freeman, R. (1981) Composite pulse decoupling. *J. Magn. Reson.* 43, 502–507.
- (51) Levitt, M. H., Freeman, R., and Frenkiel, T. (1982) Supercycles for broadband heteronuclear decoupling. *J. Magn. Reson.* 50, 157–160.
- (52) Levitt, M. H., Freeman, R., and Frenkiel, T. (1982) Broadband heteronuclear decoupling. *J. Magn. Reson.* 47, 328–330.
- (53) Levitt, M. H. (1982) Symmetrical composite pulse sequences for NMR population

inversion. II. Compensation of resonance offset. *J. Magn. Reson.* 50, 95–110.

(54) Hiller, S., Wider, G., Etezady-Esfarjani, T., Horst, R., and Wüthrich, K. (2005) Managing the solvent water polarization to obtain improved NMR spectra of large molecular structures. *J. Biomol. NMR* 32, 61–70.

(55) Loria, J. P., Rance, M., and Palmer, A. G. (1999) A TROSY CPMG sequence for characterizing chemical exchange in large proteins. *J. Biomol. NMR* 15, 151–155.

6

Chapter

General discussion

The aim of this thesis was to study the reason for activity differences between the homologous enzymes PLAAT3 and PLAAT4. We hypothesized that differences in dynamics could play a role on the basis of observations accumulating over the years on the role of C-terminal (CTD) and N-terminal domains of these proteins. The transmembrane CTD was found to be crucial for PLAAT3 PLA_{1/2} activity. Uyama *et al.*¹ showed that removal of this domain resulted in loss of phospholipase activity. In contrast, Golczak *et al.*² demonstrated that PLAAT4 truncated to its NTD has phospholipase activity, indicating that the transmembrane C-terminal domain is not critical. Golczak *et al.* also demonstrated that the rate of hydrolysis of short chain phosphatidylcholines of NTD of PLAAT4 is faster than the NTD of PLAAT3. Wei *et al.*³ reported that C-terminal domains (CTDs) of both PLAAT4 and PLAAT3 can induce HeLa cell death at a comparable level, while their NTDs play opposite roles in regulating the cell death activity, even though their structures are highly similar. The NTD of PLAAT4 was found to be enhancing the cell death effect of the CTD, whereas the NTD of PLAAT3 was found to be inhibitory. These authors also complemented the observations of a previous study by Scharadin *et al.*⁴ who found that residues 102-125, part of the loop renamed as L2(B6) in the thesis, of full-length PLAAT4 was necessary for pericentrosomal localization. Based on NMR studies, Wei *et al.*³ hypothesized that the motif (residues 102-125) in PLAAT3 might be covered by the CTD while it was exposed in PLAAT4. Therefore, we hypothesized that there must lie a connection between the activities and overall dynamics contributed by amino acid differences between PLAAT3 and PLAAT4 NTDs and especially loop L2(B6).

The melting temperature of PLAAT3 is 15°C higher than that of PLAAT4 and the rotational correlation time is 33% shorter, showing that in solution PLAAT3 is a more stable and compact protein than PLAAT4. A comparison of the salt bridge networks show that the former has a more extensive network of salt bridges, which could explain these observations. Both proteins feature a large loop (L1) that is known to be disordered,^{2,3,5,6} and is shown here to be mobile on the pico-nanosecond timescale. It has been proposed that L1 is a membrane anchoring loop in the full length protein.⁶ It was shown that replacement of L1 in PLAAT3 by the equivalent loop of LRAT leads to induction of Vitamin A conversion.⁶ This indicates that the highly disordered loop may play a role in modulating activity by interacting with the membrane. Interesting differences are found between PLAAT3 and PLAAT4 around the active site.

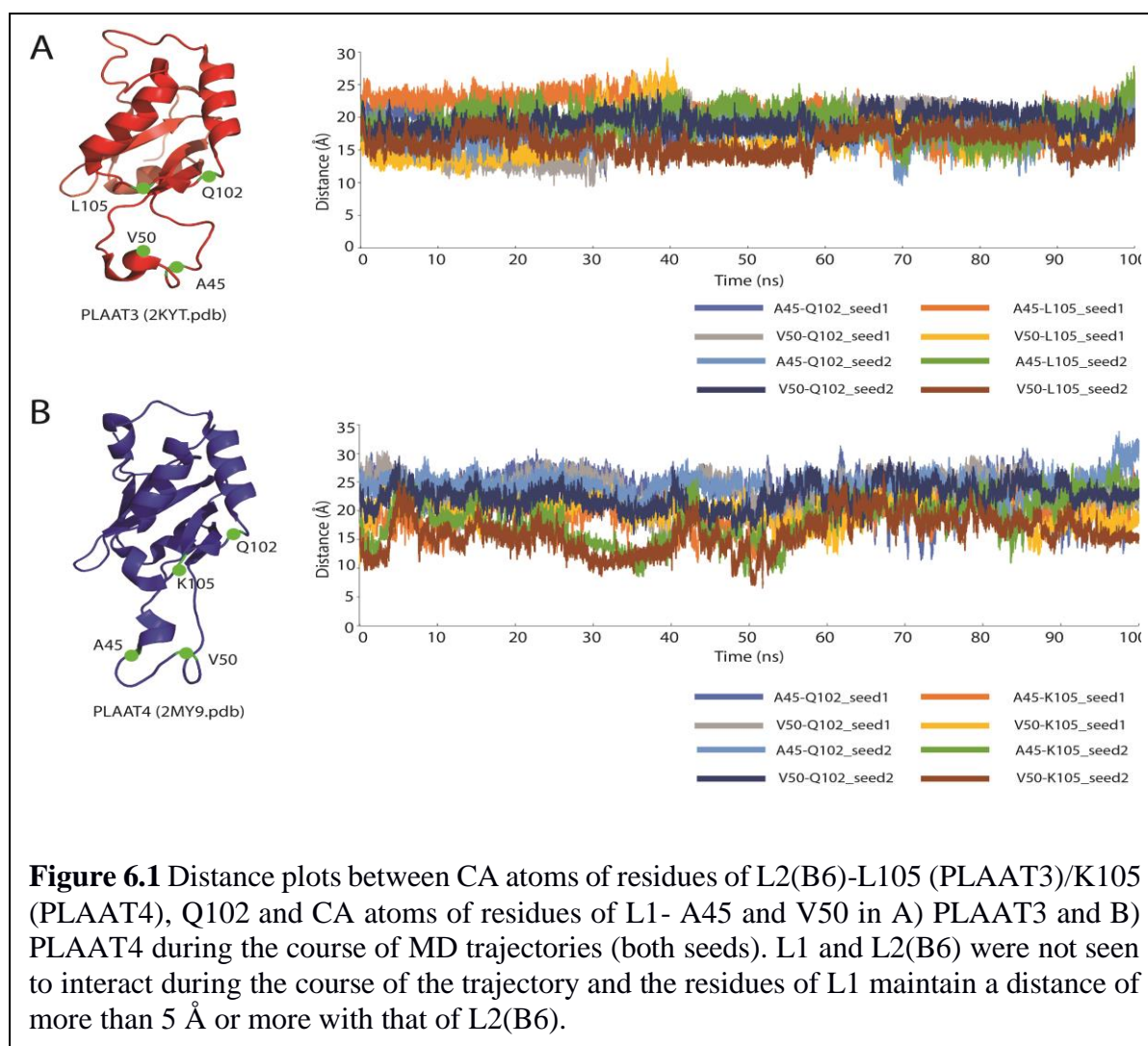
General Discussion

PLAAT4 shows low order parameters for R111 and N112, which immediately precede the catalytic nucleophile C113. Since there are no NMR resonance assignments for residues 106-110 and 113-114 in PLAAT4, it was assumed that the peaks of these residues are lacking because of line broadening due to motional chemical exchange. Millisecond timescale dynamics experiments identified a dynamic active site region involving residues 18, 19, 21, 23, 35 and 61. The resonance of G20 is missing, again indicative of exchange broadening. The peak of residue E22, which forms a salt bridge with R111, shows no broadening due to chemical exchange, which could imply that it either is not dynamic or its change in chemical shift ($\Delta\omega$) happens to be small. Thus, the active site region of PLAAT4 is dynamic, involving at least residues 18-23, 35, 61 and also 113-114. Such a dynamic patch is not observed in PLAAT3. We speculated that the difference in dynamics can explain the activity differences observed PLAAT3 and PLAAT4. The NTD of PLAAT3 may show little activity toward its substrate due to lack of active site dynamics, whereas the dynamics of PLAAT4 may enable its activity. To develop a model of what the dynamics in PLAAT4 may entail, molecular dynamics simulations were used. Although they can only sample fast dynamics, they still provided insight into the nature of motions and such calculations are known to correlate with NMR relaxation studies.⁷⁻¹⁰ The RMSD profiles obtained from the MD simulations indicated that PLAAT4 is inherently more dynamic than PLAAT3, supporting the NMR results. Using PCA, it was also demonstrated that the loop L2(B6) in PLAAT4 shows concerted motions that are absent in PLAAT3.

Thus, these observations raised the question whether the mobility of L2(B6) relates to the activity difference between PLAAT3 and PLAAT4. Increased flexibility could play a role in substrate accessibility or induced fit. Introduction of the PLAAT4 L2(B6) loop indeed increased the activity of PLAAT3 strongly, though the opposite change, introducing L2(B6) from PLAAT3 into PLAAT4, did not reduce activity. By studying the lifetimes of the salt-bridges during MD simulations of L2(B6)-swapped structures, it could be observed that the introduction of a non-native L2(B6) disrupts the inherent network of salt bridges, the disruption being more prominent in PLAAT3, reducing some of the structural rigidity which might enhance activity of PLAAT_L2(B6)₄, perhaps, by increasing substrate accessibility or greater active site flexibility.

Apart from L2(B6), studying the interaction between L2(B6) and the highly flexible loop L1 in modulating catalytic activity (especially for PLAAT3) is another facet to a greater

understanding of the workings of these enzymes, because the two loops are adjacent to each other in NTD structures. However, in light of the models proposed by Golczak *et al.*² and Pang *et al.*¹¹ for full-length enzymes, the two loops are expected to be far apart when interacting with the membrane. Wei *et al.*³ show that deletion of L1 in PLAAT3 enhances cell death inducing ability, not necessarily the phospholipase activity, since cell death inducing ability is conferred by the C-terminal domain. The authors mention that it is still not clear whether phospholipase activity plays any role in cell death. Therefore, the role of loop L1 in modulating phospholipase activity of PLAAT3 is unsure. We tried to address the question of interaction between loops L1 and L2(B6) in the NTD. Studying the interaction using NMR spectroscopy poses challenges since the NH-resonances of the residues constituting L1 are broadened beyond detection. The MD simulations show no evidence for contacts. The C_α distances between two pairs of residues in L2(B6) and L1 [Q102 and L105/K105 (PLAAT3/PLAAT4) in L2(B6) and A45 and V50 in L1] were calculated over the MD trajectory (Figure 6.1). The two loops, however flexible, do not interact significantly with each other.



General Discussion

Based on our findings, it can be concluded that PLAAT3 and PLAAT4 are dynamic proteins and the motions involve large parts of the structure. These motions clearly play an important role in modulating the activity, making it hard to explain activity differences with a simple model. For complete structural understanding of the activity difference of PLAAT family members, it will be important to compare the dynamics of the NTDs with those of the full-length proteins in a semi-native environment, such as a Nanodisc. Studying full-length proteins in Nanodiscs would also help decipher the role of the CTD and any possible interaction between the CTD and L1 loop, since L1 also interacts with the membrane and therefore should assume more defined conformation than the highly flexible loop that is observed for the NTD. It would be interesting to see if the interaction of the CTD and L1 with the membrane brings about any conformational change or change in dynamics in the NTD of PLAAT3, thereby rendering it more catalytically active than NTD itself. This could shed more light on the role of PLAAT3 phospholipase activity in obesity¹², lens degradation¹³ and in viral entry pathways.

14-16

References

- (1) Uyama, T., Kawai, K., Kono, N., Watanabe, M., Tsuboi, K., Inoue, T., Araki, N., Arai, H., and Ueda, N. (2015) Interaction of phospholipase A/acyltransferase-3 with Pex19p: a possible involvement in the down-regulation of peroxisomes. *J. Biol. Chem.* *290*, 17520–17534.
- (2) Golczak, M., Kiser, P. D., Sears, A. E., Lodowski, D. T., Blaner, W. S., and Palczewski, K. (2012) Structural basis for the acyltransferase activity of lecithin:retinol acyltransferase-like proteins. *J. Biol. Chem.* *287*, 23790–23807.
- (3) Wei, H., Wang, L., Ren, X., Yu, W., Lin, J., Jin, C., and Xia, B. (2015) Structural and functional characterization of tumor suppressors TIG3 and H-REV107. *FEBS Lett.* *589*, 1179–1186.
- (4) Scharadin, T. M., Adhikary, G., Shaw, K., Grun, D. J. B., Xu, W., and Eckert, R. L. (2014) Pericentrosomal localization of the TIG3 tumor suppressor requires an N-terminal hydrophilic region motif. *J. Invest. Dermatol.* *134*, 1220–1229.
- (5) Ren, X., Lin, J., Jin, C., and Xia, B. (2010) Solution structure of the N-terminal catalytic domain of human H-REV107--a novel circularly permuted NlpC/P60 domain. *FEBS Lett.* *584*, 4222–4226.
- (6) Golczak, M., Sears, A. E., Kiser, P. D., and Palczewski, K. (2015) LRAT-specific domain facilitates Vitamin A metabolism by domain swapping in HRASLS3. *Nat. Chem. Biol.* *11*, 26–32.
- (7) Palmer, A. (2013) Protein dynamics from NMR spectroscopy and MD simulation. *Biophys. J.* *104*, 45a.
- (8) Krepl, M., Cléry, A., Blatter, M., Allain, F. H. T., and Sponer, J. (2016) Synergy between NMR measurements and MD simulations of protein/RNA complexes: application to the RRM, the most common RNA recognition motifs. *Nucleic Acids Res.* *44*, 6452–6470.
- (9) Trbovic, N., Kim, B., Friesner, R. A., and Palmer 3rd, A. G. (2008) Structural analysis of protein dynamics by MD simulations and NMR spin-relaxation. *Proteins* *71*, 684–694.
- (10) Zhang, L., Bouguet-Bonnet, S., and Buck, M. (2012) Combining NMR and molecular dynamics studies for insights into the allostery of small GTPase-protein interactions. *Methods Mol. Biol.* *796*, 235–259.
- (11) Pang, X.-Y., Cao, J., Addington, L., Lovell, S., Battaile, K. P., Zhang, N., Rao, J. L. U. M., Dennis, E. A., and Moise, A. R. (2012) Structure/function relationships of adipose phospholipase A2 containing a Cys-His-His catalytic triad. *J. Biol. Chem.* *287*, 35260–35274.
- (12) Jaworski, K., Ahmadian, M., Duncan, R. E., Sarkadi-nagy, E., Varady, K. A.,

General Discussion

- Hellerstein, M. K., Lee, H.-Y., Samuel, V. T., Shulman, G. I., Kim, K., de Val, S., Kang, C., Sul, H. S., Val, S. De, Kang, C., and Sul, H. S. (2009) AdPLA ablation increases lipolysis and prevents obesity induced by high-fat feeding or leptin deficiency. *Nat. Med.* *15*, 159–168.
- (13) Morishita, H., Eguchi, T., Tsukamoto, S., Sakamaki, Y., Takahashi, S., Saito, C., Koyama-Honda, I., and Mizushima, N. (2021) Organelle degradation in the lens by PLAAT phospholipases. *Nature* *592*, 634–638.
- (14) Baggen, J., Liu, Y., Lyoo, H., van Vliet, A. L. W., Wahedi, M., de Bruin, J. W., Roberts, R. W., Overduin, P., Meijer, A., Rossmann, M. G., Thibaut, H. J., and van Kuppeveld, F. J. M. (2019) Bypassing pan-enterovirus host factor PLA2G16. *Nat. Commun.* *10*, 3171.
- (15) Elling, U., Wimmer, R. A., Leibbrandt, A., Burkard, T., Michlits, G., Leopoldi, A., Micheler, T., Abdeen, D., Zhuk, S., Aspalter, I. M., Handl, C., Liebergesell, J., Hubmann, M., Husa, A.-M., Kinzer, M., Schuller, N., Wetzler, E., van de Loo, N., Martinez, J. A. Z., Estoppey, D., Riedl, R., Yang, F., Fu, B., Dechat, T., Ivics, Z., Agu, C. A., Bell, O., Blaas, D., Gerhardt, H., Hoepfner, D., Stark, A., and Penninger, J. M. (2017) A reversible haploid mouse embryonic stem cell biobank resource for functional genomics. *Nature* *550*, 114–118.
- (16) Staring, J., von Castelmuur, E., Blomen, V. A., van den Hengel, L. G., Brockmann, M., Baggen, J., Thibaut, H. J., Nieuwenhuis, J., Janssen, H., van Kuppeveld, F. J. M., Perrakis, A., Carette, J. E., and Brummelkamp, T. R. (2017) PLA2G16 represents a switch between entry and clearance of Picornaviridae. *Nature* *541*, 412–416.

Summary

Phospholipase A/acyltransferases (PLAATs) play important roles in living organisms. From being tumor suppressors to regulating obesity to producing important bioactive lipids, new facets of these enzymes are being discovered and much of the inner workings of these enzymes are still unknown.

In **chapter 1**, the PLAAT family is introduced along with the knowledge obtained over the last two decades. PLAATs are a five-membered family of enzymes that share common secondary structure and a highly conserved sequence NCEHFV, which contains the catalytic triad member cysteine that acts as a nucleophile in catalysis. With the exception of PLAAT5, all PLAATs have an N-terminal catalytic domain and a C-terminal membrane anchoring domain. The PLAATs catalyze the first step of reaction, leading to the formation of N-acylethanolamines (NAEs), an important class of bioactive lipids that play a variety of roles, such as anti-inflammation, catabolism of fat, anti-apoptotic activity, ligands for endocannabinoid receptors etc. PLAAT3 and PLAAT4 are homologues but both display marked differences in their activity and specificity. For PLAAT3, the C-terminal domain is crucial for PLA_{1/2} activity, whereas the same domain is not critical for the same in PLAAT4. Furthermore, the N-terminal domain of PLAAT4 is a more active phospholipase, more rapidly hydrolyzing acyl-protein intermediates than PLAAT3. Physiologically, PLAAT3 regulates triglyceride metabolism in adipose tissue, whereas PLAAT4 plays a crucial role in tumor suppression, particularly in metastasis and invasion. Studying these two proteins on a molecular level was the topic of this thesis. The two methods- NMR spectroscopy and MD simulations that were deployed to elucidate the differences, are described in the chapter along with the thesis outline.

In **chapter 2**, the insights obtained from thermostability, NMR dynamics experiments and salt bridge analysis are outlined. PLAAT3 shows higher thermostability than PLAAT4, owing to its compact structure with well dispersed network of salt-bridges throughout the structure which in PLAAT4 are less and are confined to certain regions. Residue specific fast (ps-ns) and slow (ms) dynamics were studied using NMR spectroscopy. Apart from the highly disordered loop L1 in both the enzymes, PLAAT3 largely maintains a rigid structure and its active site does not show significant dynamics. This is however not true in case of PLAAT4, which is overall more flexible than PLAAT3 and its active site is much more mobile. This was

inferred by the low order parameters for residues that immediately precede the catalytic nucleophile C113. The absence of resonances for residues in the active site region indicated broadening due to chemical exchange. Millisecond timescale dynamics experiments also identified a dynamic active site region. Such a dynamic patch is not observed in PLAAT3. We speculated that the difference in dynamics can explain the activity differences observed PLAAT3 and PLAAT4. The NTD of PLAAT3 may show little activity toward its substrate due to lack of active site dynamics, whereas the dynamics of PLAAT4 may enable its activity.

To develop a model of what the dynamics of PLAAT4 would entail, molecular dynamics simulations were used, findings of which are presented in **chapter 3**. The global RMSD of PLAAT4 was observed to be higher than of PLAAT3, suggesting that the former undergoes conformational fluctuations during the simulations, confirmed by higher radius of gyration than for PLAAT3. Principal component analysis to study essential dynamics shows that PLAAT3 maintains a largely rigid conformation, especially an ordered secondary structure. In PLAAT4, more concerted motions were observed, especially in and around the active site. Apart from the flexible loop L1, loop L2(B6) and C113S_γ showed correlated motions. A significant rearrangement was observed in L2(B6) and since the α -helix A3, of which C113 is a part, is connected to this loop, its rearrangement rendered the active site quite mobile. The interaction between the cysteine of the catalytic triad and the histidine rings was also disrupted during each of the two runs.

The significance of the loop L2(B6) in modulating the activity was further studied in **chapter 4**. *In-vitro* and *in-silico* mutagenesis were carried out to swap the loop L2(B6) between PLAAT3 and PLAAT4. L2(B6)₄ mutation in PLAAT3 conferred higher phospholipase activity than in wild type PLAAT3 by introducing greater dynamics around the active site region, causing increased substrate accessibility. However, when L2(B6)₃ was introduced in PLAAT4, the activity increased as well. By MD simulations on the L2(B6) mutants, the role of these loops in overall dynamics were also studied, which did not yield clear differences in dynamics between the wild-type and mutant proteins. Salt bridge life-time analysis revealed that introduction of PLAAT4 L2(B6) in PLAAT3 caused disappearance of 50% existing salt bridges, enabling mobility. This mobility due to lack of salt bridges might be crucial for greater solvent accessibility. A similar effect was observed in PLAAT4_L2(B6)₃, which caused disappearance of 50% existing salt bridges in PLAAT4 suggesting that the swapping of L2(B6) changes the chemical environment and existing salt bridge networks in both PLAAT3 and PLAAT4. This observation, along with the data from phospholipase assay, strongly support

our hypothesis that the L2(B6) mutation in PLAAT3 restructured the salt bridges and introduced greater dynamics around the active site region, causing increased substrate accessibility.

Chapter 5 describes a project done with Dr. Hugo van Ingen aimed at removing slow pulsing artifacts in ^{15}N CPMG relaxation dispersion experiments introduced by using a single ^1H decoupling power for all CPMG pulsing rates. The slow-pulsing artifacts were analyzed in detail and it was demonstrated that the artifact can be suppressed through the use of composite pulse decoupling (CPD). The performances of various CPD schemes are reported and it was demonstrated that CPD decoupling based on the $90_x-240_y-90_x$ element results in high-quality dispersion curves free of artifacts, even for amides with high ^1H offset.

Chapter 6 describes general discussion on the outcomes and insights generated in this thesis.

Samenvatting

Fosfolipase A / acyltransferasen (PLAAT's) spelen een belangrijke rol in levende organismen. Het zijn tumoronderdrukkers, ze reguleren obesitas en produceren belangrijke bioactieve lipiden. Nieuwe facetten van deze enzymen worden nog steeds ontdekt en veel van de interne werking van deze enzymen is nog onbekend.

In **hoofdstuk 1** wordt de PLAAT-familie geïntroduceerd, samen met de kennis die de afgelopen twee decennia is opgedaan. PLAAT's zijn een vijfledige familie van enzymen die een gemeenschappelijke secundaire structuur en een sterk geconserveerde sequentie NCEHFV delen. De sequentie bevat het katalytische triade-lid cysteine, dat fungeert als het nucleofiel tijdens de katalyse. Met uitzondering van PLAAT5 hebben alle PLAAT's een N-terminaal katalytisch domein en een C-terminaal membraanverankerdomoien. De PLAAT's katalyseren de eerste reactiestap die leidt tot de vorming van N-acylethanolamines (NAE's), een belangrijke klasse van bioactieve lipiden die verschillende rollen spelen, zoals ontstekingsremming, katabolisme van vet, anti-apoptotische activiteit, het fungeren als liganden voor endocannabinoïde receptoren, enz. PLAAT3 en PLAAT4 zijn homologen, maar vertonen duidelijke verschillen in hun activiteit en specificiteit. Voor PLAAT3 is het C-terminale domein cruciaal voor PLA_{1/2}-activiteit, terwijl hetzelfde domein niet kritisch is voor deze functie in PLAAT4. Bovendien is het N-terminale domein van PLAAT4 een actiever fosfolipase dat sneller acyl-eiwit-tussenproducten hydrolyseert dan PLAAT3. Fysiologisch reguleert PLAAT3 het triglyceridenmetabolisme in vetweefsel, terwijl PLAAT4 een cruciale rol speelt bij de onderdrukking van tumoren, vooral bij metastase en invasie. Het bestuderen van deze twee eiwitten op moleculair niveau, vormde het doel van dit proefschrift. De twee methoden - NMR-spectroscopie en MD-simulaties, die werden gebruikt om de verschillen op te helderen, worden beschreven in dit hoofdstuk.

In **hoofdstuk 2** worden de inzichten verkregen uit thermostabiliteit, NMR-dynamica-experimenten en zoutbrughanalyse geschetst. PLAAT3 vertoont een hogere thermostabiliteit dan PLAAT4 dankzij de compacte structuur met een goed verspreid netwerk van zoutbruggen, die in PLAAT4 minder zijn en beperkt zijn tot bepaalde regio's. Residu-specifieke snelle (ps) en langzame (ms) tijdschaaldynamica werden bestudeerd met behulp van NMR-spectroscopie, waarbij duidelijk verschillen werden gevonden. Afgezien van de zeer wanordelijke lus L1 in beide enzymen, behoudt PLAAT3 grotendeels een rigide structuur en

vertoont de actieve site geen significante dynamiek. Dit is echter niet het geval bij PLAAT4, dat over het algemeen flexibeler is dan PLAAT3 en waarin de actieve site veel mobieler is. Dit werd afgeleid uit de lage ordeparameters voor residuen die onmiddellijk voorafgaan aan het katalytische nucleofiel C113. De afwezigheid van resonanties voor residuen rond de actieve site duidde op verbreding als gevolg van chemische uitwisseling. Milliseconde tijdschaal-dynamica-experimenten identificeerden ook een dynamisch actief site-gebied met actieve site-residuen. Zo'n dynamische patch wordt niet waargenomen in PLAAT3. We speculeerden dat het verschil in dynamiek de waargenomen activiteitsverschillen PLAAT3 en PLAAT4 kan verklaren. De NTD van PLAAT3 vertoont mogelijk weinig activiteit ten opzichte van zijn substraat vanwege een gebrek aan actieve site-dynamiek, terwijl de dynamiek van PLAAT4 zijn activiteit mogelijk maakt.

Om een model te ontwikkelen van wat de dynamica van PLAAT4 zou inhouden, werden moleculaire dynamica-simulaties gebruikt, waarvan de bevindingen worden gepresenteerd in **hoofdstuk 3**. Waargenomen werd dat de globale RMSD van PLAAT4 hoger was dan PLAAT3, wat suggereert dat de eerste conformationele fluctuaties ondergaat tijdens de simulaties, wat wordt ondersteund door een grotere traagheidsstraal dan die van PLAAT3. Analyse van hoofdcomponenten om essentiële dynamica te bestuderen, toont aan dat PLAAT3 grotendeels een starre conformatie behoudt, vooral een geordende secundaire structuur. In PLAAT4 werden meer gecoördineerde bewegingen waargenomen, vooral in en rond de actieve site. Afgezien van de flexibele lus L1 vertoonden lus L2(B6) en C113S_γ gecorreleerde bewegingen. Een significante herschikking werd waargenomen in L2(B6) en aangezien de α -helix A3, waarvan C113 een onderdeel is, verbonden is met deze lus, maakte de herschikking de actieve site behoorlijk mobiel. De interactie tussen het cysteïne van de katalytische triade en de histidineringsring werd ook tijdens elk van de twee runs verstoord.

De significantie van de lus L2(B6) bij het moduleren van de activiteit werd verder bestudeerd in **hoofdstuk 4**. *In-vitro* en *in-silico* mutagenese werden uitgevoerd om de lus L2(B6) te verwisselen tussen PLAAT3 en PLAAT4. L2(B6)₄-mutatie in PLAAT3 resulteerde in een hogere fosfolipase-activiteit dan in wild-type PLAAT3, door een grotere dynamiek rond de actieve site te introduceren, wat de toegankelijkheid van het substraat vergroot. Als L2(B6)₃ in PLAAT4 wordt geïntroduceerd, neemt echter ook daar de activiteit ook toe. Door MD-simulaties op de L2(B6)-mutanten werd de rol van deze lussen in de algehele dynamiek bestudeerd, wat geen duidelijke verschillen in dynamiek opleverde tussen de wild-type en mutanteiwitten. Levensduuranalyse van zoutbruggen toonde aan dat de introductie van

PLAAT4 L2(B6) in PLAAT3 ervoor zorgde dat 50% van de bestaande zoutbruggen verdwenen. De extra mobiliteit door het ontbreken van zoutbruggen kan cruciaal zijn voor een betere toegankelijkheid van kleine moleculen. Een vergelijkbaar effect werd waargenomen in PLAAT4_L2(B6)₃, waar 50% van de bestaande zoutbruggen in PLAAT4 verdwenen, wat suggereert dat het omwisselen van L2(B6) de chemische omgeving en bestaande zoutbrugnetwerken in zowel PLAAT3 als PLAAT4 verandert. Deze waarneming, samen met de gegevens van de fosfolipase-analyse, ondersteunt sterk onze hypothese dat de L2(B6)-mutatie in PLAAT3 de zoutbruggen herstructureerde en een grotere dynamiek introduceerde rond de actieve site, waardoor de toegankelijkheid voor het substraat werd vergroot.

Hoofdstuk 5 beschrijft een project uitgevoerd met dr. Hugo van Ingen en dat zich richtte op het verwijderen van artefacten bij lage pulsfrequenties in ¹⁵N CPMG-relaxatiedispersie-experimenten geïntroduceerd door gebruik van één enkele ¹H-ontkoppelingsmethode bij alle frequenties. Het langzaam pulserende artefact werd in detail geanalyseerd en er werd aangetoond dat het artefact kan worden onderdrukt door het gebruik van samengestelde pulskoppeling (CPD). De prestaties van verschillende CPD-schema's worden gerapporteerd en er werd aangetoond dat CPD-ontkoppeling op basis van het 90x–240y–90x element resulteert in hoogwaardige dispersiekrommen zonder artefacten, zelfs voor amiden met een hoge ¹H offset.

Hoofdstuk 6 beschrijft de algemene discussie over de uitkomsten en inzichten gegenereerd in dit proefschrift.

Curriculum Vitae

Soumya Deep Chatterjee was born in Siliguri, India on 18th of May 1990. In 2008, he got accepted in Calcutta University after finishing high school. In 2011, he obtained Bachelor of Science (Honours) degree in Microbiology. Thereafter, he continued studying for a master's degree from the same university in the same year.

His master's thesis was done under the supervision of senior scientist dr. Sujoy Mukherjee of the Indian Institute of Chemical Biology, where he first came across NMR spectroscopy as a technique to study protein dynamics. His thesis was on expressing and purifying a recombinant human immunoglobulin, performing backbone resonance assignment and predicting backbone torsion angles obtained from processing NMR data.

In 2013, he obtained a degree as Master of Science in Microbiology, winning a gold medal for securing the first position. In the same year, he joined Indian Institute of Chemical Biology as research project fellow under senior scientist Dr. Sujoy Mukherjee to continue working on protein dynamics using CPMG relaxation spectroscopy.

In 2014, he started his PhD project within Leiden Institute of Chemistry in then Protein Chemistry (now Macromolecular Biochemistry) group. The research was conducted under the supervision of Prof. Dr. Marcellus Ubbink and Prof. Dr. Mario van der Stelt. During his research, he focused on dissecting the differences in activity and specificity of homologs PLAAT3 and -4 using protein dynamics information obtained from NMR spectroscopy and MD simulation. Parts of his work were presented as posters at an EMBO conference (Munich, 2015), the Netherlands NMR Discussion Group (Wageningen, 2016), the Netherlands Chemistry conference (CHAINS, Veldhoven, 2016) and as oral presentation in Netherlands NMR Discussion Group (Nijmegen, 2018).

Publications

1. Chatterjee, S. D., Ubbink, M., and van Ingen, H. (2018) Removal of slow-pulsing artifacts in in-phase ¹⁵N relaxation dispersion experiments using broadband ¹H decoupling. *J. Biomol. NMR* 71, 69–77.
2. Chatterjee, S. D., Zhou, J., Dasgupta, R., Cramer-Blok, A., Timmer, M., van der Stelt, M., and Ubbink, M. (2021) Protein Dynamics Influence the Enzymatic Activity of Phospholipase A/Acyltransferases 3 and 4. *Biochemistry* 60, 1178–1190.